UNIVERSITY OF READING

Department of Meteorology

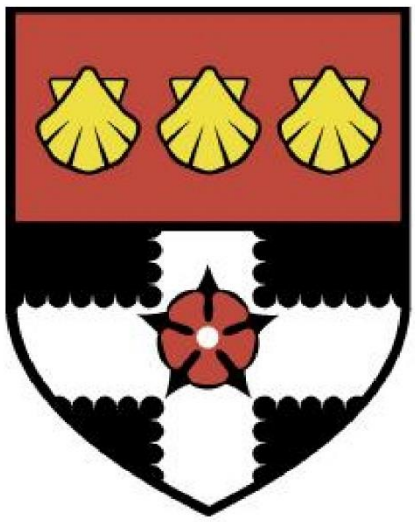

Use of a calibrated ceilometer network to improve high resolution weather forecasts

EMMA HOPKIN

A thesis submitted for the degree of Doctor of Philosophy

September 2018

Declaration: I confirm that this is my own work and the use of all material from other sources has been properly and fully acknowledged.

Emma Hopkin

Abstract

Ceilometers are simple, relatively inexpensive vertically pointing lidars usually operating at wavelengths of 905-910 nm or 1064 nm that can function reliably unattended for long periods and, as the name suggests, have mainly been used for detecting cloud base at airports where they are valuable for air safety issues. In addition to detecting the large backscattered return from cloud base, they can provide vertical profiles of backscatter from both clouds and aerosols every 5-30 seconds with a range resolution of 10-20 m.

This thesis presents a simple and robust method for calibrating ceilometers that has been tested in an operational environment. The method relies on using the integrated backscatter (B) from liquid clouds that totally extinguish the ceilometer signal; B is inversely proportional to the lidar ratio (S) of the backscatter to the extinction for cloud droplets. It is shown that for accurate calibration, care must be taken to exclude any profiles having targets with different values of S, such as drizzle drops and aerosol particles, profiles that do not totally extinguish the ceilometer signal, profiles with low cloud bases that saturate the receiver, and any profiles where the window transmission or the lidar pulse energy is low. A range dependent multiple scattering correction that depends on the ceilometer optics is applied to the attenuated backscatter profiles. A simple correction for water vapour attenuation for ceilometers operating at around 910 nm wavelength is applied to the signal using the vapour profiles from a forecast analysis. The consistency of profiles observed by a pair of co-located ceilometers in the UK Met Office network operating at around 910 nm and 1064 nm provides independent validation of the calibration technique.

Secondly, an ice cloud forward model is used to predict attenuated backscatter, using profiles of ice water content (IWC) from the Met Office's numerical weather prediction model, the UKV. A second moment approximation for particle area and mass is assumed, so that IWC becomes proportional to extinction. The lidar ratio for ice cloud is then used to calculate backscatter from the model derived extinction. The lidar ratio is calculated using ceilometer observations of thick attenuating ice cloud. Comparisons between the UKV derived attenuated backscatter and the attenuated backscatter observed by a ceilometer suggest that the UKV IWC is systematically too small in magnitude and too high in height.

Acknowledgements

I am very grateful for the contribution to this thesis made by my supervisors Anthony Illingworth and Chris Westbrook, for the support, patience and feedback given throughout the four years of this project and for always being there to share their wealth of knowledge and give me advice, no matter how frequent my questions. Thank you to Cristina Charlton-Perez, who, despite leaving the project half way through and no longer being an official supervisor, continued to give me endless support, both academically and emotionally right to the very end. I am also grateful to the late Sue Ballard, whose knowledge of the Met Office UM was inspirational and who continued to check on me and my progress, despite her illness. Many thanks to Lee Hawkness-Smith, for stepping on to the project and for so much support and advice which helped me in getting my thesis written up. I must also give thanks to all the members of TOPROF, and in particular, Simone Kotthaus and Maxime Hervo for sharing their wide knowledge and understanding of the intricacies and idiosyncrasies of ceilometers.

Special thanks to all the PhD students I have met during this time. In particular, Carly Wright, Hannah Bloomfield and Caroline Dunning who were always there to support me through the ups and downs with many many cups of coffee.

I am so grateful to my family, in particular my parents Ian and Rosey Hopkin, who have encouraged me and supported me continuously whilst I endlessly changed my mind about what I wanted to do with my life. Finally, I would like to thank Graeme Marlton, who believed in me and my work when I didn't, who supported me and encouraged me when I couldn't see the end and who supplied me with gin, chocolate and walks in the Chilterns when I needed to escape. I know that I would not have got this far without him.

Contents

Chapter 1:

Introduction and Motivations

1.1 Exploiting ceilometer networks

Cloud and aerosols play an important part in our everyday life, influencing our behaviour, our safety and our health. The monitoring and study of cloud and aerosol properties is therefore a vital topic in the forecasting and research of weather and climate. Traditionally, ceilometers were designed for the sole purpose of determining cloud base height. However, these single wavelength, low power lidars are capable of observing an entire vertical profile through the boundary layer, with backscatter data from aerosol, ash and cloud. Though ceilometer lidars are very basic when compared to more sophisticated high power lidar systems which may operate at multiple wavelengths, such as those with Raman or high spectral resolution capability, ceilometers do have several important advantages. Ceilometers are relatively cheap to purchase and operate, they are generally reliable, and can run continuously with little to no human intervention and maintenance. It is therefore easy for meteorological centres to develop a ceilometer network with a high spatial and temporal density. In fact, many national meteorological services, such as the UK Met Office, already have a network in place. High power lidars, on the other hand, while having substantially more sophisticated capabilities, are

also substantially more expensive and therefore much more sparsely distributed. Many of these high-power lidars are operated by research institutes and are therefore recording data only occasionally or during dedicated field campaigns (Wiegner et al., 2014).

Ceilometers measure backscattering profiles from near-ground level up to 8-15 km, depending on the manufacturer and design. In addition to the cloud base, observations derived from the backscatter of aerosols, haze, fog, virga, precipitation and clouds can be measured. Data on the boundary layer height and the visibility can also be determined.

1.2 The importance of observations for nowcasting, NWP and climate models

According to the most recent Intergovernmental Panel on Climate Change, cloud and aerosol amounts and their properties continue to be to the source of the largest uncertainty to estimates and interpretations of the Earth's changing energy budget and therefore the largest source of uncertainty in the representation of cloud processes in climate models (Stocker et al., 2013). Clouds play an important role in the Earth's climate system as they interact with both short wave (solar) radiation and long wave (terrestrial) radiation through absorption, emission and reflection. They therefore have both a warming and a cooling effect on the atmosphere through cloud-radiative feedback processes. Clouds also contain updrafts which carry energy, moisture, momentum, trace gases, and aerosol particles from the surface to heights of thousands of metres (Stocker et al., 2013). Cloud processes occur over a wide range of spatial scales, including scales much smaller than the typical model grid box. This necessitates the need for accurate cloud parameterisation schemes within general circulation models (GCMs). The ability to produce these accurate parameterizations is developed through an accurate knowledge of cloud properties and processes, which is itself developed through the use and study of observations.

In addition to the use of cloud parameterisation in climate prediction models, cloud processes are also important for short term forecasting in numerical weather prediction (NWP) models. The activity of humans is greatly influenced by the current and near term weather and the behaviour of the weather conditions generated by clouds, which can range from a general nuisance (e.g. light precipitation) to conditions which put human life at risk (e.g. thunderstorms, tornadoes, hurricanes). It is therefore clear that in order to accurately forecast such events, accurate forecasting of clouds is necessary.

The weather also plays a vital role in the aircraft industry, both domestic and military. The monitoring of cloud type and position and of visibility is a vital part of aircraft safety and can have a huge financial impact on airports and airlines, and reduce disruption to passengers.

The accuracy of GCMs and NWPs continues to improve and the role of observations in achieving these improvements is evident. For example, Huang et al. (2012) integrated observations of temperature, relative humidity and wind speed and gust into several NWP models, showing a significant improvement to the nowcasting of these variables. Recent studies such as Schuhen et al. (2018) are beginning to investigate the possibility of updating a forecast trajectory in post-processing using the most recent observations. The improvement of forecasting clouds in models is hampered, however, by inaccurate and intermittent observations (Illingworth et al., 2007). The development of network hubs that focus on the data processing, calibration and quality evaluation of networks of automatic instrumentation therefore has a vital role to play in the continued improvement of forecasting.

1.3 Cloud types and properties

Ceilometers are capable of observing several cloud layers. Based on the classification by Luke Howard (1803), clouds are grouped into the categories of cumulus, stratus and cirrus. The following section gives a brief summary of the cloud types and structures and follows Lohmann

et al. (2016) as reference, using the typical approach of grouping clouds into four types: low-level, mid-level, high-level and clouds with vertical extent.

1.3.1 Low-level clouds

Low-level clouds, located in the first 2 km of the troposphere, are shallow stratiform clouds with a vertical extent of up to 1 km. The main cloud types are stratus (St) and stratocumulus (Sc). Stratus cloud is a blanket-like layer cloud and has a similar appearance to high fog, such as that which occurs in Alpine valleys. However, whereas fog forms due to isobaric cooling and touches the ground, stratus cloud (as other cloud types) forms due to the adiabatic expansion and cooling in rising air masses.

Stratocumulus clouds are layered and have flattened cloud tops. While stratocumulus can have a patchy appearance, the individual cloud elements are connected to form a cloud layer and therefore differ to the cumuliform clouds (see section 1.3.4) which are clearly separate from each other.

Stratus and stratocumulus clouds tend to produce drizzle, where droplets have
radii between 25 μm and 0.25 mm. Graupel particles (heavily rimed snow particles) may also form at cooler temperatures.

1.3.2 Mid-level clouds

Cloud types with a cloud base at heights of 2 – 7 km comprise altocumulus (Ac), which have typical vertical extent of 200 – 700 m, and altostratus (As), which are typically 1 – 3 km thick. They typically form due to the slow upward lifting of air masses.

Altostratus clouds have a layered, uniform appearance, similar to low level stratus clouds, but have a smaller optical depth and so appear less grey than stratus cloud. Their presence can often be a precursor to an approaching warm front or occlusion.

Altocumulus clouds are convective clouds, formed due to local instabilities. They consist either of distinct cloud elements which are detached clouds or as rolls in layers and patches.

Virga (precipitation that evaporates or sublimates before it reaches the ground) may fall from altocumulus and altostratus clouds, visible in the form of fall streaks.

1.3.3 High-level clouds

High-level clouds consist of cirrus (Ci), cirrostratus (Cs) and Cirrocumulus (Cc) and are comprised completely of ice crystals. They are found at heights above 7 km in the troposphere. Cirrocumulus is a finely granulated cloud with many small, similar looking cloud elements intersected by areas of blue sky. Cirrostratus clouds have a waveless structure and have no identifiable individual cloud elements. Cirrus clouds consist of delicate filaments and are optically thin enough that they rarely produce shading. These high-level clouds have a much lower water content compared to low- and mid-level clouds.

1.3.4 Clouds with vertical extent

The fourth cloud type consists of clouds which are characterized by a low cloud base height and a large vertical extent and comprise cumulus (Cu), cumulonimbus (Cb) and nimbostratus (Ns). Nimbostratus is typically associated with long-lasting precipitation and is a formless, dark grey cloud. They form when air masses are lifted along a warm front in a low pressure system.

Convective clouds (cumulus and cumulonimbus) develop due to buoyancy in unstable air, where the air is sufficiently moist. Cumulus clouds have rounded tops and are generally well spaced over the cloud layer. Fair weather cumulus have a limited vertical development but may grow in height as the day progresses, developing into a cauliflower-like shape with a dark base. This is categorised as a towering cumulus (TCu) and is also known as cumulus congestus.

Further vertical development results in cumulonimbus storm clouds, which can have bases as low as 600 m and extend more than 12 km, reaching the tropopause. Further ascent is prevented by the stable inversion, resulting in the tops flattening and spreading out horizontally leading to the formation of an anvil. As with high-level clouds, the cold cloud top, consists of only ice crystals. In the middle region of the cumulonimbus cloud, both water droplets and ice crystals can be found. The warmer, lower parts of cumulonimbus consist of water droplets alone.

1.4 The importance of ice clouds

Of particular interest for this thesis is the importance of ice clouds and ice water content (IWC). Much of the recent development in the uses of attenuated backscatter as measured by ceilometers has focussed on the potential of this instrument to provide observations of aerosols. While the observations of ice clouds with ceilometers does provide some challenges, due to weaker signal-to-noise ratios (SNR) at the heights where ice clouds are found and due to attenuation of the ceilometer signal by lower clouds, ceilometer networks do have the potential to assist in the improvement of forecasting ice clouds, as shown in chapter 5.

IWC is a critical quantity in climate studies because it is used to determine other variables such as cloud absorption, optical depth, albedo and emissivity (Heymsfield et al., 2003) and, therefore, errors in model IWC are propagated through to other variables (Abel et al., 2014).

Ice clouds present a greater challenge than liquid water clouds in modelling the future climate because of the greater complexity of ice processes (Stocker, 2013). By furthering our understanding of how ice clouds behave in the present climate, we can improve our ability to model how ice cloud will behave in a future climate.

1.5 This thesis

Following this introduction, Chapter 2 summarises the lidar theory that is relevant to this thesis. The principals of lidar theory are presented, including an overview of scattering theory and of the lidar equation. The chapter also discusses the history of ceilometers, emphasising their development from being used purely for cloud base height measurements to an instrument capable of delivering full vertical profiles of attenuated backscatter and the research that exploits these measurements. An overview of the instrumentation used in this thesis is then presented. The final section of Chapter 2 discusses the basic concepts of comparing observations with model data.

In Chapter 3, the cloud calibration automated algorithm is explained. The corrections required to calibrate the ceilometer data are discussed, including a novel method of correcting for water vapour attenuation for ceilometers with a wavelength of 905-910 nm. Chapter 4 then discusses the results for the calibration of the Met Office ceilometer network, highlighting the stability of the calibration and showing that the ceilometers produced by different manufacturers with different wavelengths observe the same magnitude of attenuated backscatter when calibrated using the cloud calibration algorithm.

Chapter 5 presents an example of a novel use of a calibrated ceilometer: the assessment of the representation of ice clouds in the Met Office's UKV model. A forward model that produces simulated profiles of attenuated backscatter from the UKV ice water content is presented and the results are compared to profiles of attenuated backscatter observed by a ceilometer.

Concluding remarks and the possibility of future work in the development of the attenuated backscatter forward model are discussed in chapter 6.

Chapter 2:

Lidar and Ceilometer Fundamentals

2.1 Introduction

The use of observations is an essential part of refining and improving numerical weather prediction (NWP) models. While some observations used in data assimilation come from in-situ measurements, such as those made by radiosondes and aircraft, measurements from remote sensing instruments are essential for longer, more sustained temporal coverage. The remote sensing of cloud and aerosol properties can be split in to two types; passive and active. While passive instrumentation works by detecting emitted or scattered electromagnetic radiation from a natural source, active remote sensors emit electromagnetic radiation that is then scattered back to the sensor. As the speed of light is a known constant, the delay in the return of the emitted pulse of radiation (for a known angle) gives the position of the scatterer. Active remote sensing instrumentation has the potential to profile the atmosphere at high temporal and spatial resolutions.

In this chapter, the principles of lidar and ceilometer remote sensing are discussed. Section 2.2 presents some of the fundamentals of lidar technology, giving a brief history of lidar development and introducing the subject of scattering theory and the lidar equation. Section

2.3 then introduces ceilometers; a low power, automatic lidar with a single wavelength. The history of ceilometers as cloud base height recorders is described and their development into an atmospheric profiling research tool. Sections 2.4 and 2.5 describe the instruments used in this thesis, giving an overview of their technical properties. Finally, section 2.6 details the study of ice cloud properties and the use of observations to inform and improve model output. The potential for ceilometers to aid this work is discussed.

2.2 Principals of lidar remote sensing

The use of light detection and ranging (lidar) has developed as an essential component of observing and profiling the atmosphere for both research and forecasting the weather and the climate. In principal, the fundamentals of lidar are remarkably simple; the lidar emits light from a laser and records the time and intensity with which the light is returned to the instrument. Appendix B shows a schematic of a lidar receiver and transmitter.

2.2.1 A brief history

The earliest attempts of using light as a remote sensing instrument actually predates the invention of the laser, to when searchlights were used in the 1930s, to determine air density profiles of the atmosphere (Weitkamp, 2005). The use of observing scattered light at different frequencies was patented in 1949 (Neufeld, 1949), a precursor to the modern multi-wavelength lidar. The first functional laser was developed at Hughes Research Laboratories by Theodore Maiman in 1960, followed by the first atmospheric observations using a ruby laser in 1963 (Fiocco and Smullin, 1963). The developments of the basic lidar principals rapidly followed, culminating in the routine use of lidar by meteorologists to observe liquid and ice clouds, make various aerosol measurements, record visibility, determine water vapour content, to name but a few. Lidar development remains closely linked to advancements in laser technology, with

demands on power, wavelength and beam shape driving the innovations in the field of laser research (Weitkamp, 2005).

2.2.2 Scattering theory

In the context of lidar research, the two terms which are of most importance are undoubtedly 'backscatter' and 'extinction'. Backscatter is defined as the deflection of radiation through an angle of 180°, that is, in the backward direction towards the lidar receiver. Extinction is defined as the reduction in the intensity of radiation as it passes through a medium, due to absorption, reflection, or scattering out of the path of the beam. At lidar wavelengths, extinction is dominated by scattering. The interaction of radiation with a scatterer can be described by Rayleigh and Mie scattering.

2.2.2.1 Rayleigh scattering

Rayleigh scattering is defined as the elastic scattering from particles that are very small compared to the wavelength of the scattered radiation and is used to describe molecular scattering (Weitkamp, 2005). The intensity of Rayleigh scattering is inversely proportional to the fourth power of the wavelength and therefore dominates at shorter wavelengths (e.g. 355 nm) but is considered negligible at longer lidar wavelengths (e.g. 1064 nm).

2.2.2.2 Mie scattering

Developed by Mie (1908), Mie scattering theory describes the scattering of radiation of any wavelength and therefore technically includes Rayleigh scattering, as well as converging to geometric optics for large particles. In the context of lidar theory however, Mie scattering is more commonly used to describe the scattering intensity from particles that are of comparable or larger size than the wavelength of the radiation, such as aerosol particles, haze and cloud

droplets. For scattering particles of similar size to the radiation wavelength, the scattering intensity varies strongly with wavelength (Weitkamp, 2005). For large particles, where Mie scattering converges to the geometric optics regime, scattering is independent from wavelength.

2.2.2.3 Geometric optics

The geometric optics regime is where the size of particle is much greater than the wavelength and the scattering is wavelength-independent (provided the refractive index does not change) and the extinction cross section is simply equal to twice the projected area of the particle. At lidar wavelengths, particles in this regime include raindrops and ice particles.

2.2.3 The lidar equation

In its most simple form, the lidar equation can be written as (e.g. Weitkamp, 2005)

$$P(r) = K\,G(r)\beta(r)T(r) \qquad \textit{Eq. (2.1)}$$

where the power (P) received (with the same units as the corresponding raw signal) from a distance (r) is determined by the performance of the lidar system (K), the measurement geometry (G) which encompasses the range dependent overlap function (in meters), the backscatter coefficient (β) which sums all backscatter from all scatterers and has units of m^{-1} sr^{-1}, and the two way transmission term (T) which is unitless (Mattis and Wagner, 2014). Taking these terms into account, the lidar equation can also be expressed in its more common form, written as

$$P(r,\lambda) = E\frac{O(r)}{r^2}\big(\beta(r,\lambda) + \beta_{aer}(r,\lambda) + \beta_m(r,\lambda)\big)exp\big[-2\int_0^r\big(\alpha(r,\lambda) + \alpha_{aer}(r,\lambda) + \alpha_m(r,\lambda)\big)dr\big] \qquad \textit{Eq. (2.2)}$$

where $P(r,\lambda)$ is the signal power received and is dependent on distanced (r) and wavelength (λ) . E is the lidar constant which summarises its optical and detection characteristics and is

therefore frequently termed the calibration constant. The term describes the transmitted laser pulse energy and is a function of the average power of a single laser pulse, the length of a volume illuminated by the laser pulse at a fixed time, the area of the primary receiver optics and the overall system efficiency (Weitkamp, 2005).

O(r) is the receiver and field-of-view overlap function. The overlap describes the fraction of the laser beam cross-section that is contained within the receiver field of view and is a function of range (e.g. Vande Hey et al., 2011). The total backscatter coefficient is given by the term$\big(\beta(r,\lambda)+\beta_{aer}(r,\lambda)+\beta_m(r,\lambda)\big)$, with contributions from cloud, aerosol and molecular backscatter, respectively. The exponential term describes the transmission and is a function of the extinction coefficient, given by $\big(\alpha(r,\lambda)+\alpha_{aer}(r,\lambda)+\alpha_m(r,\lambda)\big)$, with contributions from cloud, aerosol and molecular backscatter, respectively. The influence of β_m and α_m is wavelength dependent; for wavelengths of 905-1064 nm their significance can be considered negligible.

As Weitkamp (2005) describes, equation 2.2 gives the lidar signal. The detectable signal will also consist of an instrument signal (or noise) and of a background signal, typically dominated by scattered sunlight (although direct sunlight may contribute at low latitudes), but also with contributions from moon and starlight and from artificial sources of light.

2.2.4 Multiple scattering

Equation 2.2 describes photons scattered by only one scatterer before being detected; this is called single scattering. As defined by Hogan (2008), *'any scattered photons leave the field of view of the receiver and are not detected (except those in the exact backscatter direction)*'.

However, when particles are big compared to the wavelength, diffraction theory tells us that half of the extinguished radiation is diffracted into a narrow lobe in the forward scattering direction (that is, upward in the case of ground based lidar) (Hogan, 2006). The width of this

lobe in radians is approximately $\frac{\lambda}{\pi a}$, where λ is the wavelength and a is the equal-area radius of the particle. Because cloud particles are large compared to the wavelength in the case of lidar, the width of the forward lobe is narrow and is comparable to the field of view (FOV) of the lidar. So photons can undergo forward-scattering events, followed by a backscatter event and still be detected. This is known as small-angle multiple scattering (Hogan, 2008). Thus, half of the energy which would have been lost by extinction if only single scattering was present actually remains in the beam. Multiple scattering can be modelled numerically (e.g. Kattawar and Plass, 1971; Eloranta, 1998; Hogan, 2006) or approximated (Platt, 1973).

A multiple scattering factor, η (Platt, 1973), is therefore included in the transmission term of the lidar equation to express the apparent increase in backscatter and reduction in attenuation (O'Connor et al., 2004). Accounting for calibration and range correction and including the multiple scattering factor, equation 2.2 can, therefore, be written as

$$\beta_{obs}(r,\lambda) = \beta(r,\lambda)\exp\left[-2\eta\int_0^r \alpha(r,\lambda)dr\right] \qquad \textit{Eq. (2.3)}$$

where $\beta_{obs}(r,\lambda)$ is the observed attenuated backscatter, $\beta(r,\lambda)$is the backscatter coefficient and $\alpha(r,\lambda)$is the atmospheric extinction coefficient and η is the multiple scattering factor. The value of η varies between 0.5 and 1. For a value of 1, the photons entering the receiver have only been scattered once. For a value of 0.5, the maximum amount of multiple scattering is assumed to take place, meaning that all the scattered photons remain within the field of view of the lidar receiver.

2.2.5 The lidar ratio

The signal from lidars is difficult to invert because it is dependent on two parameters, as shown in equation 2.3. Extinction and backscatter often need to be derived from one measurement; the intensity of the light detected (Vande Hey, 2013). To retrieve the extinction coefficient

from the observed backscatter, the lidar ratio is required. The lidar ratio is also known as the extinction-to-backscatter coefficient and is defined as

$$S = \frac{\alpha_p(r,\lambda)}{\beta_p(r,\lambda)} \qquad \textit{Eq. (2.4)}$$

where S is the lidar ratio, and α_p and β_p are the particle extinction and backscatter, respectively. The particle lidar ratio at a given range is dependent on the size distribution, shape and chemical composition of the particles (Weitkamp, 2005). The lidar ratio can therefore vary considerably with the target, with typical values between 10 and 100 sr. Considerable effort has been given to reducing the error in determining the lidar ratio in order to relate observations of backscatter to the unknown extinction in order to determine further microphysical properties of the atmosphere (e.g. Ansmann et al., 1992, Müller, 2007).

Substituting in the lidar ratio, equation 2.3 can be expressed as

$$\beta_{obs}(r,\lambda) = \frac{\alpha(r,\lambda)}{S} \exp\left[-2\eta \int_0^r \alpha(r,\lambda)dr\right] \qquad \textit{Eq. (2.5)}$$

where $\beta_{obs}(r,\lambda)$ is the lidar observed attenuated backscatter. Further detail on how the lidar ratio relates to the lidar equation is shown in Appendix A.

2.3 An overview of ceilometers

Ceilometers are single wavelength, low-power lidars. Sometimes termed 'the poor man's lidar', ceilometers are basic in comparison to higher power lidars, which may operate at multiple wavelengths and have Raman or high spectral resolution capability. While ceilometers were designed specifically for measuring just cloud base height, high power lidar were designed for much more sophisticated observations. Ground based lidar have been used to observe atmospheric densities up to heights of 100 km, for almost as long as lasers have been manufactured (e.g. Mc Cormick et al., 1967; Kent and Keenliside, 1975). However, as mentioned in Chapter 1, ceilometers do have several advantages. High power lidars are

substantially more expensive and therefore more sparsely distributed. They are most frequently operated by research institutes and, due to large running costs, are therefore recording data only occasionally or during dedicated field campaigns (Wiegner et al., 2014). Ceilometers, on the other hand, are relatively cheap, reliable and can run continually without much need for human intervention. Furthermore, many national meteorological services, such as the UK Met Office, already have a network of ceilometers in place.

2.3.1 Development of ceilometers

The very first form of ceilometer used projectors to generate beams of light, directed at the cloud base. The height at which the beam of light formed a spot on the cloud was then calculated using trigonometry (EMS, 2017). This method was first demonstrated and described by Poul la Cour (1871) and led to the development of rotating beam ceilometers with an incandescent lamp that used optical triangulation to measure the height to cloud base (Eberhard, 1986). The first patent for a laser ceilometer was eventually filed in 1974 (Vander Hey, 2013; Segre and Truscott, 1976).

2.3.2 Using ceilometers to study clouds

Ceilometers were designed specifically to measure cloud base height (CBH) and visibility. The accurate determination of CBH is vital to the aviation industry, to providing information for real-time operational forecasting and for use in validation and data assimilation of CBH in numerical weather prediction (NWP) models. CBH is also a significant parameter in the characterisation of clouds (Hirsch et al., 2011) and ceilometers are therefore frequently used to investigate cloud base behaviour and climatologies (e.g. Costa-Surós et al., 2013; Albrecht et al., 1988).

While CBH has previously been defined as the height at which the ceilometer signal reaches its maximum value (Eberhard, 1986), this definition often disagrees with pilot reports which are based on visibility. Ceilometer manufacturers have therefore developed their own proprietary algorithms; as a commercial product, the exact definition used is not disclosed. This can result in disparities between different models. Martucci et al. (2010) demonstrated the differences between a Jenoptik CHM15k and a Vaisala CL31 ceilometer (see section 2.4 for more detail on these ceilometer models) collocated at Mace Head Atmospheric Research Station in Ireland. The authors demonstrated that the Vaisala ceilometer produced systematically higher cloud base measurements compared to the Jenoptik ceilometer, with a worst-case scenario from the 12 case studies examined resulting in an offset of 570 m. This can be an issue when National Weather Services have ceilometer networks with more than one ceilometer model.

In addition to the commercial algorithms for CBH, a number of researchers have developed their own versions of CBH detection. As a lidar system, employing the same method of observation as high power lidar, ceilometers observe a full vertical quantitative profile of attenuated backscatter. Martucci et al. (2010) developed the temporal height tracking (THT) algorithm, which uses the maximum value of attenuated backscatter in each vertical profile, coupled with the vertical gradient of the attenuated backscatter profile. The THT algorithm reduced the disparity that the authors had found between the CBH given by the collocated Vaisala CL31 and Jenoptik CHM15k ceilometers. When applied, the THT algorithm reduced the 12 case study average offset from 160 m to – 3 m.

Other algorithms aim to optimise CBH detection for a particular cloud type. For example, Tricht et al. (2014) noted that the commercial algorithm favoured optically thick, liquid water clouds but struggled with the detection of thin ice clouds. The authors developed a polar threshold (PT) algorithm based on Platt et al. (1994), using a threshold technique. However,

where Platt et al. (1994) used a multiple of the standard deviation of the background fluctuations, Tricht et al. (2014) found that the absolute surface attenuated backscatter was necessary for a threshold method because the background signal of clear polar air is extremely low and therefore would have triggered spurious CBH detection near the surface.

2.3.3 Development of ceilometer aerosol profiling

In addition to the development of CBH detection algorithms, the use of the full vertical profile of attenuated backscatter has led to the development of several areas of research using ceilometers. Note that in order to make use of the attenuated backscatter data, the ceilometers must be calibrated. This is discussed in Chapter 3. One of the primary areas is the study of aerosols. The study of aerosol radiative forcing, aerosol transport, aerosol-cloud interactions and air pollution requires continuous vertical observations in near real time. While more advanced lidar are required for the detailed study of aerosol type and concentration, ceilometers can be used to provide a larger spatial coverage at a lower cost. The INTERcomparison of Aerosol and Cloud Tracking (INTERACT) campaign which was part of the Aerosol Clouds Trace gases Research InfraStructure (ACTRIS, http://www. actris.org), explored the capabilities of ceilometers for aerosol profiling (Madonna et al., 2015). The aim of the campaign was to assess the stability, sensitivity, and uncertainties of ceilometer aerosol attenuated backscatter profiles by comparing with an advances multi-wavelength Raman lidar. Madonna et al. (2015) found that the Jenoptik CHM15k showed a better correlation with the Raman lidar attenuated backscatter coefficient, but the Campbell-Scientific CS135s and the Vaisala CT25k ceilometers generally underestimated the aerosol attenuated backscatter. The author concluded that the ceilometers had potential for aerosol profiling but currently lacked stability due to sensitivity to temperature changes and further technological improvements are required. Wiegner et al. (2014) drew a similar conclusion, as part of the European Aerosol

Research Lidar Network (EARLINET) framework. In assessing the potential of ceilometers for the quantitative retrieval of aerosol properties, Wiegner et al. (2014) found that the uncertainties in the incomplete overlap of the ceilometers, the unknown lidar ratio for aerosols, and the issue of water vapour absorption meant that the exploitation of ceilometers was very much in its infancy and further studies were required.

2.3.4 TOPROF

In order to develop the potential of vertical profiling using a ceilometer network, the European Union funded the Cooperation in Science and Technology (COST) Action ES1303, Towards Operational ground based PROFiling with ceilometers, doppler lidars and microwave radiometers for improving weather forecasts (TOPROF). The main aims of TOPROF were to develop the data formats, calibration techniques and retrieval algorithms for a European network of instruments. The work under TOPROF and continued by E-PROFILE (part of the EUropean METeorological services NETwork (EUMETNET) Composite Observing System, EUCOS) has led to the development of a network of several hundred ceilometers which provide attenuated backscatter profiles of aerosol and cloud properties with 30 m vertical resolution once a minute. As part of this action, the CeiLinEx2015 campaign was devised to evaluate attenuated backscatter and cloud base height products and to quantify and reduce inhomogeneities between ceilometers of different generations and manufacturers (Mattis et al., 2016).

A study by Kotthaus et al. (2016) focussed on the CL31 ceilometers manufactured by Vaisala and identified distinct differences in profiles of attenuated backscatter from collocated ceilometers (e.g. Emeis et al., 2009). Due to the collaboration of ceilometer manufacturers and research scientists in TOPROF, Vaisala released new firmware aimed at meeting the requirements of researchers, compared to earlier versions which were focussed on the needs of

pilots and forecasters. The new firmware (versions 1.72 and 2.03) required certain versions of hardware. Kotthaus et al. (2016) compared older firmware (versions 1.70, 1.71 and 2.02) to the new firmware to develop correction procedures for the older firmware to account for data artefacts and allow for consistent processing of historic data.

2.3.5 Developments in ceilometer research

A novel use of ceilometer attenuated backscatter profiles was the development of a fog formation alert system (Haeffelin et al., 2016).The development of fog is of particular interest at airports where air traffic can be significantly disrupted by poor visibility at ground level which makes it unsafe to take off, land and taxi on the runway. Based on the temporal evolution of attenuated backscatter observations, an algorithm has been developed to provide alerts of the formation of radiation fog, on the scale of minutes to hours before the fog event. The Predictive Alert of Radiation FOG (PARAFOG) algorithm tracks aerosol backscatter hygroscopic growth and for the 45 case studies tested, was capable of raising an alert at least 30 minutes before every event. PARAFOG is currently deployed using the Vaisala CL31 at the Charles de Gaulle airport, Paris, to support the forecasting of poor visibility on the airport runways (Haeffelin et al., 2016).

Inferring mixing height is another example of potential uses for ceilometer profiles of attenuated backscatter. Several algorithms have been developed which employ ceilometer observations to detect mixing height (e.g. Münkel et al., 2007; Eresmaa et al., 2012; Sokół et al., 2014; Tang et al., 2016) and use a gradient method, exploiting the distinctive decrease in aerosol concentration between the boundary layer and the free atmosphere above (Kotthaus et al., 2016). For example, Tang et al. (2016) found that under conditions of neutral stratification, the ceilometer underestimates the mixing height; however, in general, the ceilometer retrieved

mixing heights were fairly consistent with the radiosonde mixing heights, resulting in a correlation coefficient greater than 0.9.

2.4 The Met Office ceilometer network

The primary source of ceilometer data for this project comes from the Met Office ceilometer network. Within the Met Office, the ceilometers are also known as laser cloud base recorders or LCBRs. The network contains 138 LCBRs which are continually recording cloud base height. The majority of these ceilometers were manufactured by Vaisala. 11 of the ceilometers, however, were manufactured by Jenoptik and purchased by the Met Office following the 2010 eruption of Eyjafjallajökull, Iceland to monitor volcanic ash. Note that Jenoptik no longer produce ceilometers; the manufacturing of new ceilometers and any maintenance and servicing of the Jenoptik ceilometers has been taken over by Lufft. From here on, we refer to these ceilometers as Lufft ceilometers, including those manufactured before production passed from Jenoptik to Lufft.

Figure 2.1 shows the locations of the 40 ceilometers in the UK that are presently reporting the full vertical profiles of the atmospheric attenuated backscatter. The purple crosses show the location of the 29 sites with a Vaisala CL31 ceilometer and the red crosses show the 2 sittes with a Jenoptik CHM15k Nimbus ceilometer. The remaining 9 sites have collocated Vaisala and Jenoptik ceilometers. These are the instruments that have been used to test the ceilometer calibration technique described in Chapters 3 and 4.

2.4.1 Vaisala Cl31

The majority of the Met Office ceilometers are the CL31 model, although there are still some of the older Vaisala CT25k ceilometers in use. These older ceilometers are in the process of

being decommissioned and replaced so are not discussed in this thesis, however the ceilometer calibration algorithm described in Chapter 3 is still applicable to the CT25k ceilometers.

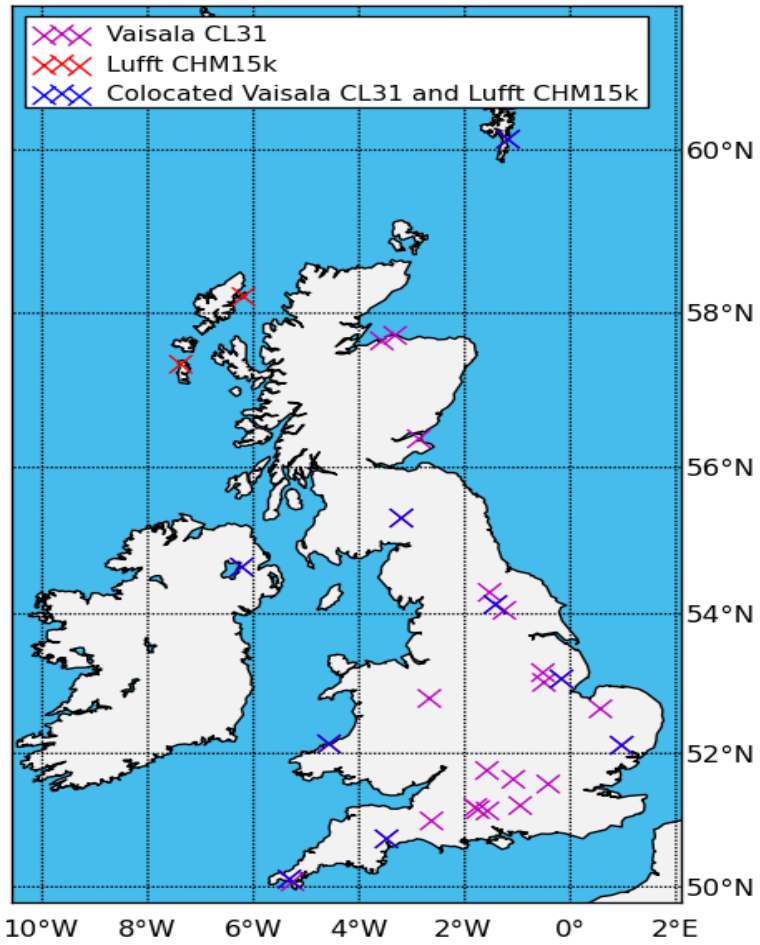

Figure 2.1: Location of Met Office ceilometers which record the full profile of attenuated backscatter. Sites with a Vaisala CL31 ceilometer are indicated by a purple cross, sites with a Lufft CHM15k nimbus ceilometer are indicated by a red cross and sites with both a Vaisala CL31 and a Lufft CHM15k nimbus ceilometer are indicated by a blue cross.

The key technical properties of the Vaisala CL31 ceilometers and the Lufft CHM15k nimbus ceilometers used by the Met Office are summarised in Table 2.1. In brief, the Vaisala CL31 ceilometers use an InGaAs diode laser which emits pulses with an energy of 1.2 μJ at a pulse

repetition frequency (prf) of 10 kHz with a central wavelength of 910 ± 10nm, though the typical spectral width is more often 4 nm (Kotthaus et al. 2016, Markowicz et al. 2007). At these wavelengths, attenuation by water vapour is significant.

Specification	Vaisala CL31	Lufft CHM15k
Laser	InGaAs Diode	Nd:YAG
Centre Wavelength	910 nm	1064 nm
Wavelength Variability	± 10 nm	insignificant
Optical Design	coaxial	Biaxial
Pulse Energy	1.2 μW	8 μW
Pulse Repetition Rate (PRF)	10 kHz	5-7 kHz
Temporal Resolution	30 s	30 s
Vertical Resolution	20 m *	15 m
Complete Overlap	70 m	1000 m
Maximum Detection Range	7.6 km	15 km

*Table 2.1: Summary of some technical characteristics and parameters of the Vaisala CL31 and Lufft CHM15k, as operated in the Met Office network. * Exeter CL31 has a vertical resolution of 10 m.*

Due to the low power of ceilometers, they have a much higher pulse repetition rate compared to high-power lidars, to compensate for this lower power and to increase the signal to noise ratio. The CL31s have a single lens design, with the centre of the lens collimating the laser beam and the outer part of the lens used for focussing the backscattered light onto the receiver, which uses an avalanche photo diode (APD) detector to process the signal (Münkel et al., 2007). Complete overlap of the transmitted beam at the receiver sample is achieved at a height of approximately 70 m (Martuccci et al., 2010) and the maximum range is 7.6 km.

There are currently several different versions of the older Vaisala firmware in use by the Met Office ceilometer network. The various versions process the signal in different ways, applying "cosmetic" shifts to the data to avoid unphysical negative backscatter values. The original users for ceilometer data were airline pilots and these cosmetic shifts were applied so that it was easier for non-experts to interpret the displays. Full details of the shifts and methods for correcting can be found in Kotthaus et al. (2016). These effects should certainly be corrected

for in the study of smaller particles such as aerosols and ash; however, for the stronger signal from cloud particles the effects of these shifts on the calibration method discussed in Chapters 3 and 4 and on the ice cloud forward model in Chapter 5, are negligible.

2.4.2 Lufft CHM15k nimbus

The Lufft ceilometers use a Nd:YAG laser and operate at a slightly longer wavelength of 1064 nm where the attenuation by water vapour is negligible. The avalanche photodiode detector (APD) detector employs a photon counting method. Due to the biaxial design of the Lufft ceilometers, full overlap is not reached until 1 km rather than 70 m for the CL31. The pulse repetition frequency is in the range 5 -7 kHz and the pulse energy is 8 μJ, which is six times higher than the Vaisala CL31 ceilometers. This higher pulse energy, combined with the different overlap configuration, results in a much higher sensitivity of the CHM15k ceilometer, for detection of elevated aerosols such as volcanic ash plumes.

2.5 Chilbolton instrumentation

While the main source of observation data for this thesis was from the Met Office network, the ice cloud forward model was developed using Vaisala the CL51 ceilometer situated at the Chilbolton Observatory, Hampshire. The main reason for this was to enable a forward model validation experiment using the radar that is collocated with the Vaisala CL51 ceilometer at Chilbolton.

2.5.1 Vaisala CL51

The Vaisala CL51 ceilometer is a newer model of ceilometer, similar to the Vaisala CL31 ceilometer but with attenuated backscatter profiling up to a range of 15 km. The Vaisala CL51

has an InGaAs diode laser which emits pulses with an energy of 3.0 μW at a pulse repetition frequency (prf) of 6.5 kHz with a central wavelength of 910 ± 10nm at 25 °C. Therefore, the ceilometer beam is subject to attenuation by water vapour, which must be corrected for. As with the CL51, the CL51 ceilometer employs a single lens design which Vaisala reports as providing nearly full overlap within 30 m (Münkel and Roininen, 2010).

2.5.2 UFAM 35 GHz 'Copernicus' cloud radar

The UFAM (Universities Facilities for Atmospheric Measurement) 35 GHz Copernicus radar operates continually and provides 30 s measurements of reflectivity, depolarisation ratio, and Doppler measurements. The radar reflectivity parameter is the intensity of the echo returned by backscatter from atmospheric particles. At 35 GHz (9 mm wavelength), the reflectivity from cloud particles is predominantly from Rayleigh scattering**.** At this wavelength, attenuation by rain droplets is large with an attenuation coefficient of approximately 0.2 dB km^{-1}. It has a range resolution of 75 m and a maximum unambiguous range of 30 km. The radar is sensitive down to -35 dBZ; that is, able to measure median volume diameters down to 100 μm (Hogan et al., 2000). The peak transmitted power is 1.5kW and the radar has an average of 5000 pulses/ray.

2.6 Matching models and observations

2.6.1 Basic concepts of data assimilation

Predicting the weather numerically is an initial conditions problem, where the atmospheric system is also chaotic in its nature (Lorenz, 1963). Given an initial estimate of the current conditions of the atmosphere, a forecast model predicts the evolution of the atmosphere. Therefore, the more accurate the initial estimate of the state of the atmosphere, the better the

accuracy of the forecast will be. To improve the accuracy of the initial conditions, the forecast is combined with observations through a process of data assimilation. Data assimilation is an analysis technique by which observations of the atmosphere are incorporated into the model state (Bouttier and Courtier, 1999). A forward model, also known as the forward operator or the observation operator, transfers the model state variables to the model equivalent of the atmospheric observations (Lorenc, 1986). Forward models are also used to evaluate and validate the ability of NWP models to represent observations and to judge the feasibility of assimilating the observation to improve the model forecast. Alternatively, the observations may be transformed to the model state. With the same variable derived from both the model and the observation, statistical comparisons can be made to detect errors and biases in the model. The use of departures between the model and the observations is therefore a key step in the data analysis before the assimilation procedure.

2.6.2 Comparing ice cloud properties of models and observations

As discussed in Chapter 1, ice cloud plays a major role in the radiation budget of the Earth. Satellite instrumentation has proved vital in providing global observations of radiatively relevant ice cloud properties, such as cloud top height and effective particle radius; however, ice clouds are still a major source of uncertainty in climate modelling (Wang et al., 2017; Waliser et al., 2009). The comparison of models with observations of ice cloud properties is therefore an important part of improving these parameters in NWP and climate modelling.

For the simulation of model variables derived from observations, the model variables used for ice cloud are cloud fraction and ice water content. Measurements from satellite remote sensing, ground based remote sensing and in-situ measurements, such as from aircraft, are used to derive cloud fraction and ice water content (IWC).

Cloud radars are frequently used in the study of ice cloud properties and microphysics as, unlike lidar, they have the ability to penetrate optically thick clouds (Maahn et al., 2015; Brown et al. 1995; Benedetti et al. 2003; Matrosov et al. 2002). However, radar cannot identify the base of low level water clouds and may struggle to detect optically thin cirrus cloud (Delanoe et al., 2011). Therefore, the evaluation of ice cloud representation has frequently made use of a synergy of lidar, radar and microwave radiometer. For example, the Cloudnet project was set up to continuously evaluate the representation of clouds in climate and weather forecast models using vertical profiles of cloud and aerosol properties at high temporal and spatial resolution. Illingworth et al. (2007) used radar observation data from Cloudnet sites to evaluate IWC in 7 operational forecast models. Of the models tested, they found that the Met Office global model and mesoscale model and the ECMWF model have the closest mean profile of IWC compared to the IWC derived from the observations.

Delanoe et al. (2011) focussed on cloud fraction in the ECMWF model and the Met Office model and used observations from the CloudSat radar and CALIPSO lidar. They found that although the models captured the main geographical distributions, both models overestimated ice cloud occurrence in the Tropics and Antarctica for higher temperature ranges and underestimated the occurrence of ice cloud at very low temperatures.

When converting lidar and radar observations to model variables, care must be taken to account for the loss of signal power due to attenuation as the beam passes through clouds (Wilkinson et al., 2008). To make a fair comparison and reduce the number of assumptions made, the approach of simulating the raw observation from the model output (using a forward model) may be more favourable (Chiriaco et al., 2006). Using this method, the attenuation through thick cloud will be accounted for. Chiriaco et al. (2006) used this method to simulate midlatitude ice clouds using the fifth-generation Pennsylvania State University–NCAR Mesoscale Model (MM5). They tested four methods and found that in each case the ice cloud

was too persistent compared to observations from the SIRTA observatory lidar and radar. Wilkinson et al. (2008) used a similar method, simulating attenuated backscatter from the ECMWF model with a lidar forward model and comparing to the Ice, Cloud and Land Elevation Satellite (ICESat). They also found that the ECMWF overestimates the amount of ice cloud present in the Tropics.

2.6.3 Attenuated backscatter forward models using ceilometers

The assimilation of CBH from ceilometer networks into NWP models has already proven beneficial in improving forecast skill (e.g. Dow and Macpherson, 2013). There are many examples of ceilometers being used in synergy with radar to determine the CBH for model comparison (e.g. Mace et al., 1998; Beesley et al., 2000). With the continuing development of our understanding of ceilometer calibration, stability and uncertainties, the potential for model evaluation and data assimilation using the full profiles of attenuated backscatter from ceilometer networks, in a similar manner to high power lidar and radar, is beginning to be explored.

The Met Office have designed a forward model to explore whether the assimilation of observed attenuated backscatter from their ceilometer network would be feasible and judge its potential to improve the UM high resolution forecasts (Charlton-Perez et al., 2013). The attenuated backscatter forward model uses the Edward-Slingo radiative transfer model (Edwards and Slingo, 1996) to simulate extinction by calculating the optical scattering properties for a given particle size distribution. The attenuated backscatter from aerosol, liquid water clouds and rain are forward modelled. Currently, the ice cloud attenuated backscatter is not forward modelled. Initial testing of the forward model designed by Charlton-Perez et al. (2013) suggests that realistic profiles of attenuated backscatter can be produced which are comparable to the observed attenuated backscatter profiles. However, this forward model assumes a fixed

scattering efficiency and is independent of wavelength, assumptions which are not typically suitable for aerosols (Warren et al., 2018). Therefore, a new forward model for attenuated backscatter from aerosols has been designed by Warren et al. (2018) to include aerosol speciation and wavelength dependency. This aerosol forward operator (aerFO) has the potential to be used to evaluate the performance of urban surface parameterisation schemes in the UKV and the ability of these schemes to drive growth of the mixing layer.

2.7 Conclusions

In this chapter, the fundamental principles of lidar and ceilometers were discussed. Almost since the development of the first laser in 1960, lidar has played a crucial role in observing the Earth's atmosphere. The scattering theory relevant to the use of lidar was introduced and the variables of the lidar equation discussed. An overview of ceilometers was then presented. Ceilometers were designed as cloud base recorders, however, they employ the same principle as lidar. Therefore, providing we can understand the uncertainties, the calibration and the stability of ceilometer vertical profiles of attenuated backscatter, ceilometers have the potential to provide automated networks of atmospheric profiling at a much cheaper cost than traditional lidar. The Met Office has a network of 40 ceilometers consisting of Vaisala CL31 ceilometers and Lufft CHM15k ceilometers that record the full profile of attenuated backscatter. One use of this network could be to improve the representation of ice cloud in NWP models. The need for this was discussed and the concept of an attenuated backscatter forward model introduced. The need for ceilometer calibration is a crucial step in the development of ceilometer profiling and is discussed in Chapter 3.

Chapter 3:

An Automated Technique for the Calibration of a Network of Operational Ceilometers

3.1 Introduction

Ceilometers are simple, relatively inexpensive vertically pointing lidars usually operating at wavelengths of 905-910 nm or 1064 nm that can function reliably unattended for long periods and, as the name suggests, have mainly been used for detecting cloud base at airports where they are valuable for air safety issues. Recent studies have shown that, in addition to detecting the large backscattered return from cloud base, they can provide vertical profiles of backscatter from both clouds and aerosols every 5-30 seconds with a range resolution of 10-20 m. Examples of the use of ceilometer profiles in a research environment are for validation of the representation of clouds in operational numerical weather prediction (NWP) models (Illingworth et al., 2015), for aerosol profiling (Markowicz et al., 2008; Madonna et al., 2015), fog observations (Dupont et al., 2012) and the retrieval of mixing height levels (Münkel et al., 2007).

Many operational weather forecasting models now represent both clouds and aerosols by prognostic variables. Remote sensing observations are needed, firstly to test whether the

models are providing unbiased estimates of the aerosol and cloud properties, and if so, for data assimilation into such models to improve forecasts of hazardous weather such as pollution episodes and severe convective storms producing flash floods. The European Ground-Based Observations of Essential Variables for Climate and Operational Meteorology (EG-CLIMET), which was a recent Cooperation in Science and Technology (COST) action financed by the European Union, noted that there are hundreds of ceilometers deployed over Europe, which are currently under-exploited, and they recommended that they be networked to provide users easy access to calibrated backscatter data (Illingworth et al., 2015). Currently, the real-time networking is being implemented by the E-Profile programme of European Meteorological Services Network (EUMETNET) with the data formats, calibration techniques and retrieval algorithms being developed by COST action 1303: Towards operational ground based profiling with ceilometers, doppler lidars and microwave radiometers for improving weather forecasts (TOPROF).

If ceilometer data are to be used in an operational context, and potentially for data assimilation, accurate calibration is essential. The World Meteorological Organisation requirements (OSCAR 2016) suggests the goal for ice water content (IWC) is for observations to an accuracy of 10 % and aerosol optical extinction to an absolute accuracy of 0.01 km^{-1}, but no fractional accuracy is quoted. Ice particle density is usually assumed to be inversely proportional to particle size, so IWC is proportional to extinction. For a given lidar ratio, the requirement is therefore for a ceilometer calibration accuracy of 10 %.

The use of theoretical calibrations for lidars and radars based on an accurate budget of the losses and gains in the transmission and reception optics and in the electronics together with atmospheric attenuation can cause large errors (Protat et al., 2011). Accordingly, it is preferable to find some natural target that has a known backscatter value. There are two such candidates for ceilometers: firstly, the backscatter from the molecules in the atmosphere and secondly, the

integrated backscatter profile from water clouds that totally extinguish the lidar beam. The second method, using the attenuated backscatter signal from liquid water clouds, relies on the fact that the backscatter to extinction ratio (S) is a known value of 18.8 sr for wavelengths of relevance to ceilometers. The advantage of this method is that the backscatter values from liquid water clouds are very high (typically peaking at 0.3 km^{-1} sr^{-1}); hence, the signal to noise ratio of water cloud returns is very large. The first method, commonly known as Rayleigh calibration, is commonly used for lidars which operate in the UV or visible wavelength range; since molecular Rayleigh scattering is inversely proportional to the forth power of the wavelength, the clear-air signal is much greater in the visible and UV wavelength compared to the infrared wavelengths used by ceilometers. Therefore, for ceilometers, the molecular signal close to the ground is over one hundred times lower than the cloud returns and of the order 10^{-3} km^{-1} sr^{-1}. The signal falls off exponentially with height; therefore, for an accurate estimate of the molecular return it is necessary to average the ceilometer returns over several hours on selected cloudless nights when there is negligible backscatter from thin cirrus clouds or aerosols (e.g. Tsaknakis et al., 2011; Wiegner et al., 2014).

3.2 The lidar ratio

Autocalibration of ceilometers using liquid water cloud was proposed by O'Connor et al. (2004) as a simple method that requires no additional instruments to compute a calibration coefficient. The technique relies on the use of the lidar ratio (ratio of extinction to backscatter, denoted S) that is a constant for the droplets in liquid water cloud. Several studies have individually calculated S from the lidar equation using Mie theory: Pinnick et al. (1983) found that, for a wavelength of 1064 nm, S = 18.2 sr; Wu et al. (2011) calculated an S of 18.5 ± 0.47 sr for a wavelength of 1064 nm. O'Connor et al. (2004) calculated an S of 18.8±0.8 sr for a wavelength of 905 nm and showed that this was essentially constant for the observed cloud droplet size

distribution for a mean droplet size ranging from 10 to 100 μm. However, S values were lower for drizzle having larger droplets. Since S is very similar at 905 nm and 1064 nm, we follow O'Connor et al. (2004) and use S = 18.8 sr for both wavelengths.

3.3 The cloud calibration method

The method compares this theoretical S to a calculated 'apparent S'. When the ceilometer signal is completely extinguished by the cloud, the total path integrated attenuated backscatter B is equal to the reciprocal of twice the lidar ratio:

$$B = \int_0^\infty \beta_{observed}\, dz = \int \beta_{True}(z)\, exp[-2\tau(z)]\, dz$$

$$= \frac{1}{\eta S}\int exp(-2\tau)\, d\tau = \frac{1}{2\eta S} \qquad \textit{(Eq. 3.1)}$$

where B is the total integrated attenuated backscatter, τ is the optical thickness, S is the theoretical lidar ratio, and η is a multiple scattering correction which is dependent on laser wavelength, beam divergence, telescope field of view, and altitude (z). The multiple scattering corrections are height dependent and calculated for each gate using the method and code described by Hogan (2015). η is usually between 0.7 and 0.85 for wavelengths between 905-1064 nm in liquid water clouds. The calibration technique involves multiplying the observed backscatter signal $\beta_{observed}$ by a calibration coefficient, C, so that B η = 0.025 m^{-1} sr^{-1}, the value for water drops when S =18.8 sr. Note that C is a scaling factor, and is the reciprocal of the widely used Calibration Constant C_L which is often used for photon counting receivers, and is the factor by which the count should be divided by to obtain a calibrated value (e.g. Wiegner et al., 2014).

The calibration technique will fail if there are targets contributing to B that have an S that is not equal to 18.8 sr. At ceilometer wavelengths, aerosols generally have S values above those for cloud droplets; marine aerosols have an S close to 20 sr, but most aerosols' S values are

much higher and in the range 40 to 100 for dust, smoke and ash (e.g. Omar et al., 2009). If aerosols are included then, for a theoretical given extinction, they would have a higher backscatter than cloud droplets; the value of B would be too high and, therefore, C would be too low. Conversely, drizzle has S values below those for cloud droplets, and so for a theoretical given extinction, drizzle would contribute less to B than clouds, and lead to a B that is too low, so the value of C would be too high. The inclusion of profiles that are not totally extinguishing the ceilometer return will have the same effect.

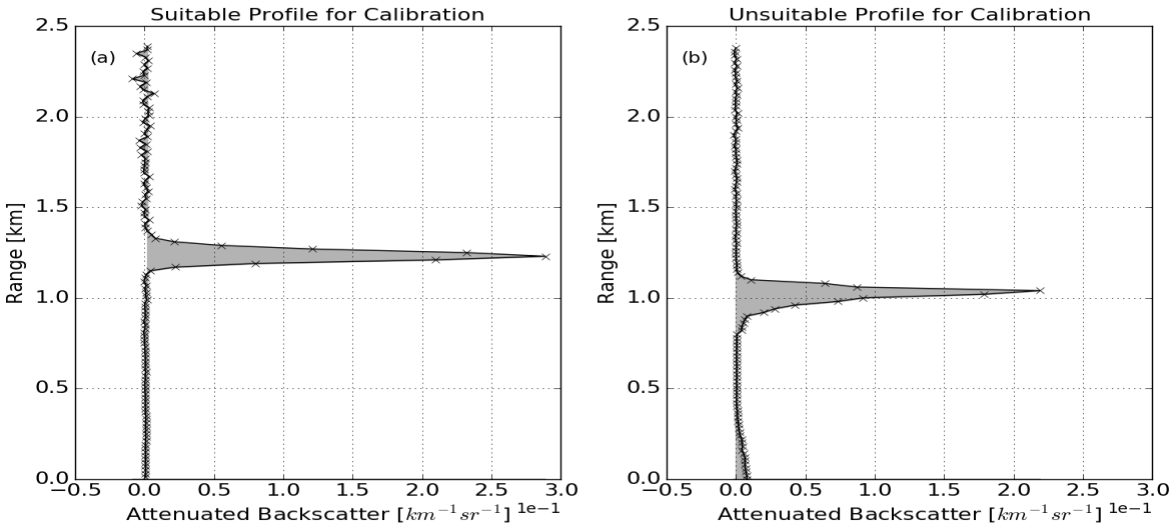

Figure 3.1: Profiles of attenuated backscatter through stratocumulus cloud. Panel (a) shows an example of a suitable profile for calibration. The integral of the profile (grey shaded area) is equal to $\frac{1}{2\eta S}$ *and, when calibrated, should give an S of 18.8 ± 0.8 sr. Panel (b) shows an example of a profile unsuitable for calibration due to the high levels of aerosol in the first 200 m. This is indicated by the grey shading up to 200 m. It is also unsuitable due to the drizzle below the stratocumulus cloud, indicated by the slight increase in attenuated backscatter underneath the peak.*

Figure 3.1a shows an example of an uncalibrated, attenuating backscatter profile typical of those from stratocumulus clouds that is ideal for use in the liquid cloud calibration algorithm. Cloud is observed as the sharp peak in attenuated backscatter just above cloud base within a

few range gates with a maximum value of 0.28 km^{-1} sr^{-1} and it clearly dominates the observed ceilometer return. The shaded area indicates the area of integration used in computing the total attenuated backscatter of the profile. The profile in figure 3.1b is for a stratocumulus cloud that completely attenuates the ceilometer return. However, in this case it is unsuitable for calibration because there is a return from aerosol is the lowest 200 m of the profile, due to the presence of drizzle indicted by a gradual increase in attenuated backscatter below the peak at cloud base.

3.4 Correcting the ceilometer data

Before the calibration can be performed, there are several issues with the data that need to be accounted for and corrected. Several of these issues are due to the fact that ceilometers were not designed to record accurately the profile of attenuated backscatter. Their design purpose was originally just to report the cloud base height and the numerical value of attenuated backscatter was not required. In studying the data observed by ceilometers, several issues have come to light which depend on the type of ceilometer.

3.4.1 Window transmission

The window transmittance is one of the optical systems specifications reported by the instrument. It is given as a percentage and indicates the visibility through the instrument window. The lower the percentage, the more obscured the instrument window is and therefore the weaker the ceilometer beam will be. For the Vaisala CL31, the manual gives 97% as the typical value of a clean ceilometer window (Vaisala, 2006). A window contamination warning is issued if the transparency is estimated to be 70% or lower.

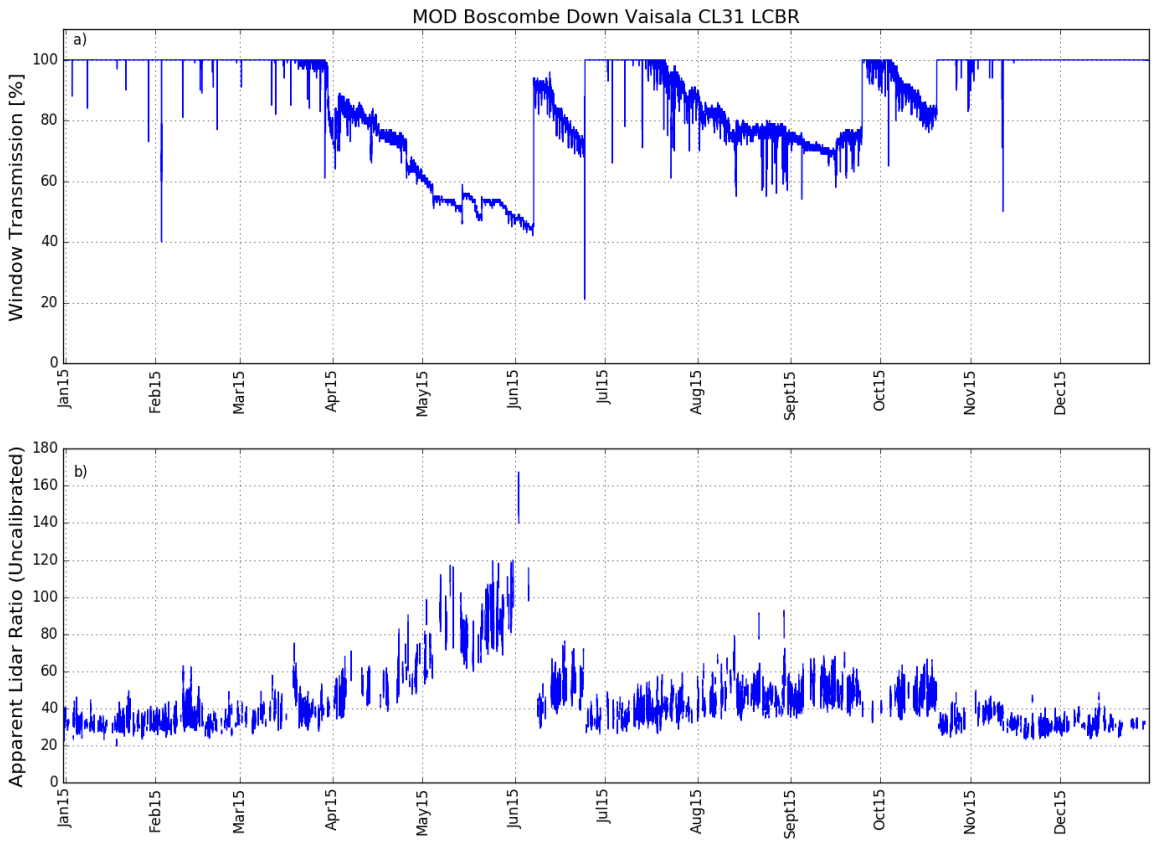

Figure 3.2: Impact of reduced window transmission on calculation of the apparent lidar ratio, shown for the Vaisala CL31 ceilometer located at Boscombe Down (51.16 °N, 1.75 °W). Panel a) shows the window transmission percentage as recorded by the ceilometer for each 30 second profile observed during the year 2015. Panel b) shows the calculated apparent lidar ratio for each 30 second profile where liquid water cloud that would be suitable for performing the cloud calibration is present during the year 2015.

Figure 3.2 gives an example of the effect of a reduced window transmission on the value of the calculated apparent S. Whenever the window transmission drops in percentage, the apparent S increases. This is because the attenuated backscatter recorded is lower than it should be, due to a weaker beam transmitted through the contaminated window to the detector. Although the relationship between window transmission and apparent S appears to be indirectly proportional, the window transmission is an estimated value, given to the nearest percentage.

Therefore, so the use of this relationship to correct a reduced window transmission could introduce a significant error to the calibration. It is more advisable to monitor the window transmission and flag any drops in the value. If the ceilometer is in an easily accessible location, the ceilometer should be cleaned.

Figure 3.2 also shows several instances where the window transmission drops by 30-50% before returning to 100%. These instances last less than 5 minutes and are caused by drizzle drops on the window. The instrument blower will clean the window in these conditions and as the calibration would not be performed during a period of drizzle, this episode of drizzle will not affect the calibration value.

3.4.2 Pulse energy

Similar to the window transmission, the laser pulse energy is an optical systems' property monitored by the instrument. The pulse energy is given as the percentage of a nominal factory setting. For the Vaisala CL31 ceilometers, the embedded software will maintain this value to between 95% and 105%. However, a faulty or expiring laser diode will result in a lower laser power that will, in turn, result in a lower recorded attenuated backscatter and, therefore, a higher apparent S. The effect of lower laser power is demonstrated in figure 3.3.

Figure 3.3a shows that the pulse energy for the Boscombe Down Vaisala CL31 ceilometer was reduced to less than 80% in September 2014 and continued to drop until the transmitter was replaced on October 9th 2014. Figure 3.3b shows the calculated apparent S for the corresponding profiles. During the period of reduced pulse energy, the apparent S is more than twice the apparent S of the profiles recorded after the transmitter was replaced.

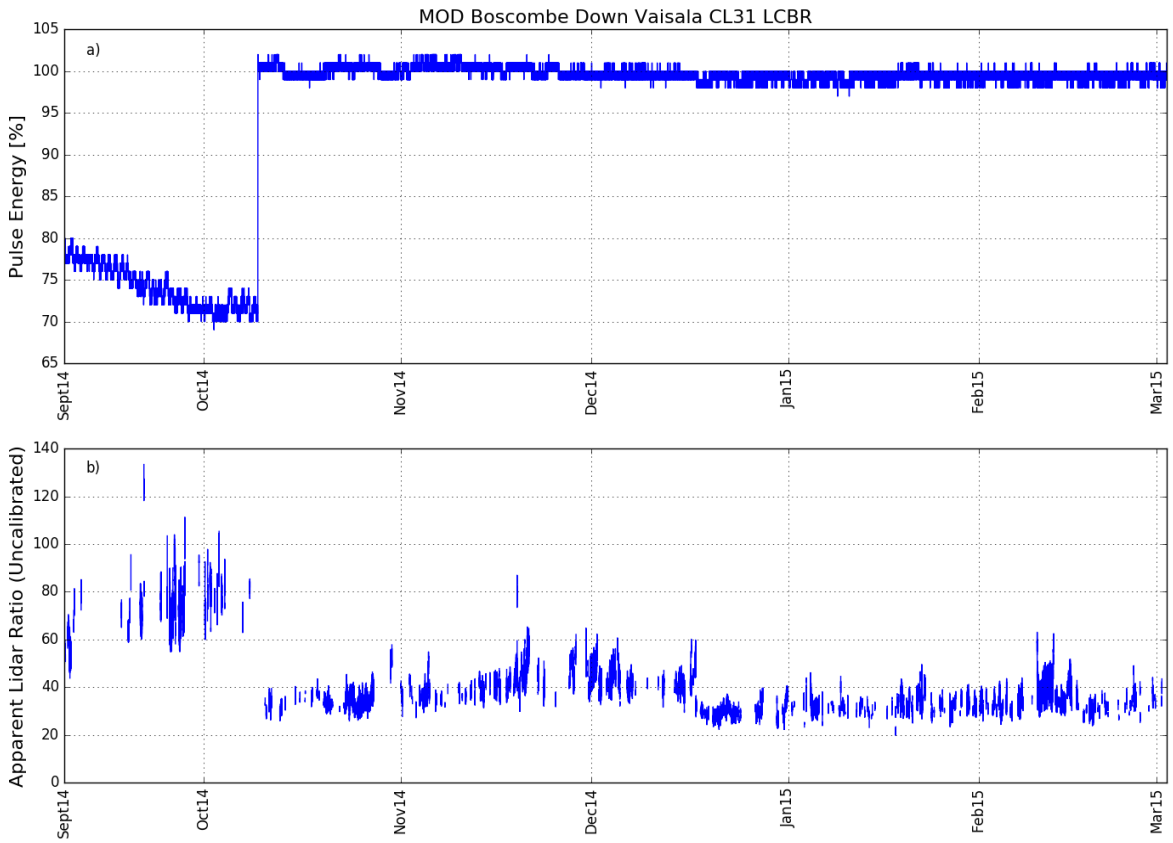

Figure 3.3: Impact of reduced pulse energy on calculation of the apparent lidar ratio, shown for the Vaisala CL31 ceilometer located at Boscombe Down (51.16 °N, 1.75 °W). Panel a) shows the pulse energy percentage as recorded by the ceilometer for each 30 second profile observed during the period September 2014 – March 2015. Panel b) shows the calculated apparent lidar ratio for each 30 second profile where liquid water cloud that would be suitable for performing the cloud calibration is present during the period September 2014 – March 2015.

As with the window transmission, this percentage pulse energy is an estimate, not an accurate observation. Therefore, attempting to correct for a reduced pulse energy should be treated with caution. Any calibration performed whilst the ceilometer has a failing transmitter should be used with caution. A ceilometer with an expiring transmitter will continue to record cloud base height measurements; however, some higher clouds may be missed.

3.4.3 Overlap region

One of the terms in the lidar equation (see chapter 2, section 2.2.3), $G(r)$, describes the geometric factor and is given by,

$$G(r) = \frac{O(r)}{r^2} \qquad \textit{(Eq. 3.2)}$$

where r is the range and $O(r)$ is the overlap function. The overlap describes the fraction of the laser beam cross-section that is contained within the receiver field of view and is a function of range (Vande Hey et al., 2011). The overlap is complete (or equal to 1) once there is absolute overlap between the laser beam and the receiver field of view. The height of complete overlap is dependent on the ceilometer design. The two main designs utilised by ceilometer manufacturers are coaxial optics or biaxial optics. Coaxial optics (e.g. Vaisala), where the laser and detector use the same aperture, result in a much smaller altitude of complete overlap. A biaxial design (eg Lufft, Belfort), where the receiver and detector optics are separated and usually do not use the same aperture, have the advantage of good optical isolation (Vande Hey, 2013). Campbell Scientific ceilometers combine these two designs to create a novel biaxial optic that utilises separate regions of the same aperture.

Determination of the overlap function requires knowledge of the laser source power distribution and propagation, the angular and positional response of the detector and the performance of the optics (Vande Hey et al., 2011). An imperfect overlap function results in the distortion of the measured backscatter due to the geometric and instrumental artefacts in the overlap region. Hervo et al., (2016) are of the opinion that the most viable method for determining the overlap function for a large network is through observing a homogeneous atmosphere so that the aerosol backscatter and extinction coefficients are constant. As a result, this method is usually only suitable for instruments that reach complete overlap within a few hundred metres.

The Vaisala CL31 ceilometers in the Met Office network have the option to apply a manufacturer-deduced overlap function which has been derived from laboratory measurements and field observations under homogeneous atmospheric conditions. This overlap function has been verified for each individual instrument and has an error of less than 10% (Kotthaus et al., 2016). The Lufft ceilometers also have an automatically applied overlap function that is specific to each ceilometer. However, recent investigations by Hervo, et al. (2016), suggests that there is a temperature dependency for this correction which results in the true correction varying by as much as 50% (for the test ceilometer at Payerne, 46.82 °N, 6.94 °E) compared to the values provided by the manufacturer. Such a large variation would not be expected for the ceilometers in the United Kingdom, due to a smaller annual cycle in temperatures than Switzerland. Nevertheless, this temperature dependency should be considered when using the data in the lowest 1500 m and should either be corrected for or accounted for in the data error.

3.4.4 Water vapour (905-910 nm ceilometers)

In the use of data from Vaisala CL31 ceilometers (and others of similar wavelength – e.g. Vaisala CL51, CT25k, CT75k, Campbell Scientific CS135), the effect of atmospheric water vapour below the cloud on the laser signal must be considered, because the wavelength of these ceilometers (910 nm) is in a weak water vapour absorption band. Note that because the Lufft ceilometers operate at 1064 nm, where there is a water vapour absorption window, the Lufft ceilometers do not require a correction for water vapour.

There have been several studies which have highlighted the attenuation of the ceilometer beam by water vapour as a potential issue, but most have tried simply to avoid the problem so that no correction is required. One method is to limit the effects of water vapour by restricting the number of range gates used; Sundström et al. (2009) limited the altitude to just a few range gates above the ceilometer so that the water vapour attenuation could be deemed a negligible

influence. Others restricted their studies so that quantitative values of backscatter were unneccessary, such as in making comparisons of cloud base height (Martucci et al., 2010) . However, for a correct calibration to be applied to the signal and for true quantitative values of attenuated atmospheric backscatter to be obtained, the issue of water vapour must be addressed. Wiegner and Gasteiger (2015) describe a method of correcting for water vapour attenuation for ceilometers at wavelengths around 910 nm by performing detailed line by line radiation transfer calculations. They investigate the impact of the instrument emission spectrum (e.g. for a CL51, Vaisala states that the wavelength is 910 with an uncertainty of ± 10 nm at 25°C and with a drift of 0.27 nm K-1). Figure 3.4a shows a figure from their paper, depicting an example of a broad (full width at half maximum of 4 nm) and a narrow (full width at half maximum of 2 nm) Gaussian emission curve and the corresponding water vapour transmission in the spectral range 904 to 916 nm.

Vaisala report that the typical emission full width at half maximum (FWHM) is 3.4 nm (Kotthaus et al., 2016). Clearly, the spectral structure of absorption is much narrower than the breadth of the spectrum emitted by the ceilometer, so that in any case a large number of the strong and weak lines are averaged. Despite this, Figure 3.4b implies that there is a sensitivity to the FWHM. However, the largest variability is for a tropical atmosphere and an instrument wavelength of 902-907 nm. As the primary focus here is a network in mid-latitudes with a ceilometer wavelength of 910 nm, the sensitivity to the exact size of the FWHM is deemed small enough to ignore for the purposes of calibration using liquid water cloud. Furthermore, the variability due to FWHM is partly dependent on temperature-induced changes to the laser diode and therefore the wavelength (Wiegner and Gasteiger, 2015).

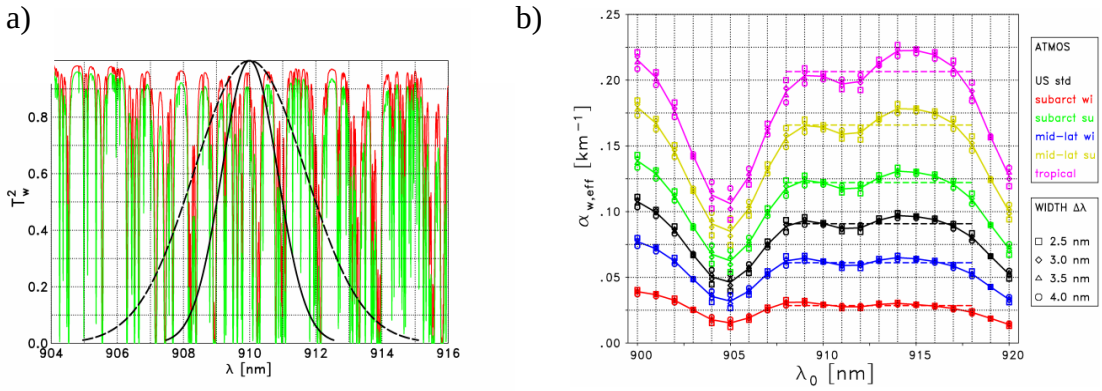

Figure 3.4: Panel (a) shows two way water vapour transmission T^2_w between the surface and 1 km (red) and 10 km (green) in the spectral range 904 and 916 nm, for mid-latitude summer conditions. Two Gaussian emission curves with FWHM = 2 nm (black, solid line) and FWHM = 4 nm (black, dashed) are shown for a wavelength of 910 nm. Panel (b) shows effective water vapour absorption coefficient $\alpha_{w,eff}$,which is inversely proportional to the two-way transmission, in the lowermost layer (0–1 km) for six standard atmospheres and different wavelengths as indicated in the legend. The dashed lines give the averages over the spectral range from 908 to 918 nm. Source: Wiegner and Gasteiger, (2015)

As the housing of the ceilometer lasers and detectors are temperature-controlled environments, the effect of laser wavelength drift due to temperature can be considered insignificant. In addition, the method described by Wiegner and Gasteiger (2015) requires the use of a radiative transfer model or access to their "WAPL" database of absorption coefficients. Because the liquid cloud calibration method presented here is intended for operational, real-time use, a simple, robust and computationally cheap method was required.

A simplified technique for correcting for the effects of water vapour attenuation has therefore been devised based on the results from Markowicz et al. (2008).

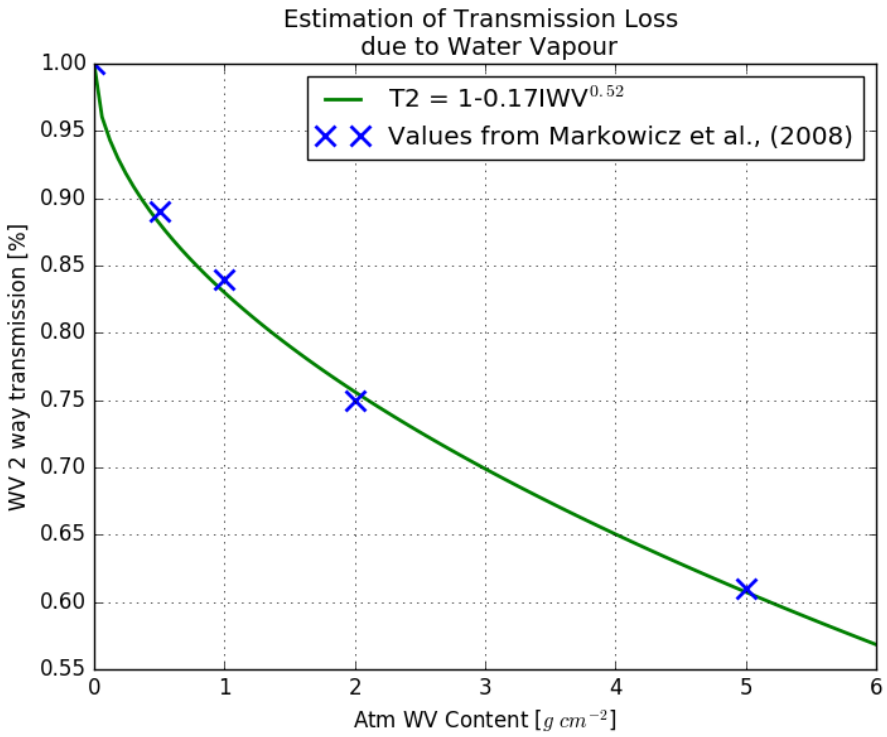

Figure 3.5: Estimated transmission loss as a function of the atmospheric water vapour content. The blue crosses are the values calculated by Markowicz et al. (2008) for a ceilometer with a wavelength of 910nm.

A simple monotonic function has been fitted (using a least squares fit) to data from Markowicz et al. (2008) to parameterise the two way attenuation by water vapour as a function of integrated water vapour (IWV) at a wavelength of 910 nm. This fitted curve is depicted in figure 3.5:

$$T_{wv} = 1 - 0.17IWV(z)^{0.52} \qquad \textit{(Eq. 3.3)}$$

where T_{wv} is the height dependent two way transmission as a percentage of the transmission without water vapour attenuation and IWV(z) is the atmospheric water vapour content from the surface to height z in g cm^{-2}. The attenuated backscatter is then corrected using:

$$B = \int \beta_{att} \times C_{wv}\ dr \qquad \textit{(Eq. 3.4)}$$

where $C_{wv} = \frac{1}{T_{wv}}$, the height dependent water vapour attenuation correction obtained from equation 3.3, and dr is the range gate resolution.

The transmission calculation for each range gate requires a value of the water vapour content which is obtained by integrating the water vapour density from the ground to each specific range gate. Then a transmission profile can be constructed. Here, a comparison of the method described with the detailed line-by-line Wiegner and Gasteiger method is made using water vapour density profiles obtained from the ECMWF model and is shown in figure 3.6. The ECMWF water vapour density profiles and the transmission profiles calculated using the Wiegner and Gasteiger method were provided by Maxime Hervo (Meteoswiss, Personal Communication, 2016).

Figure 3.6 is a typical, representative example that demonstrates the similarity in the results of the two methods between the ground and 3 km. The transmissivity through water vapour is shown as a function of height, with each of the four panels showing a different time during the example day. The WAPL method is depicted in blue and the new, simple method is depicted in red. The transmissivity profiles differ by a maximum of 2%. As the variability in the calibration from day to day differs by more than 2%, the differences in transmissivity as calculated by the two methods can be deemed negligible. Thus, this new simplified method for correcting water vapour attenuation in order to calibrate the ceilometers is deemed to be sufficient.

It should also be noted that previously the cloud calibration method was thought to be correct to within 5% (O'Connor, 2004); however, by neglecting water vapour, their calibration results would be biased by approximately 20%, depending on the time of year. The typical water vapour path in winter is 1cm leading to a transmission of about 0.85. Hence if no water vapour correction was made, one would expect an apparent annual cycle of the calibration coefficient which varied by about 12%.

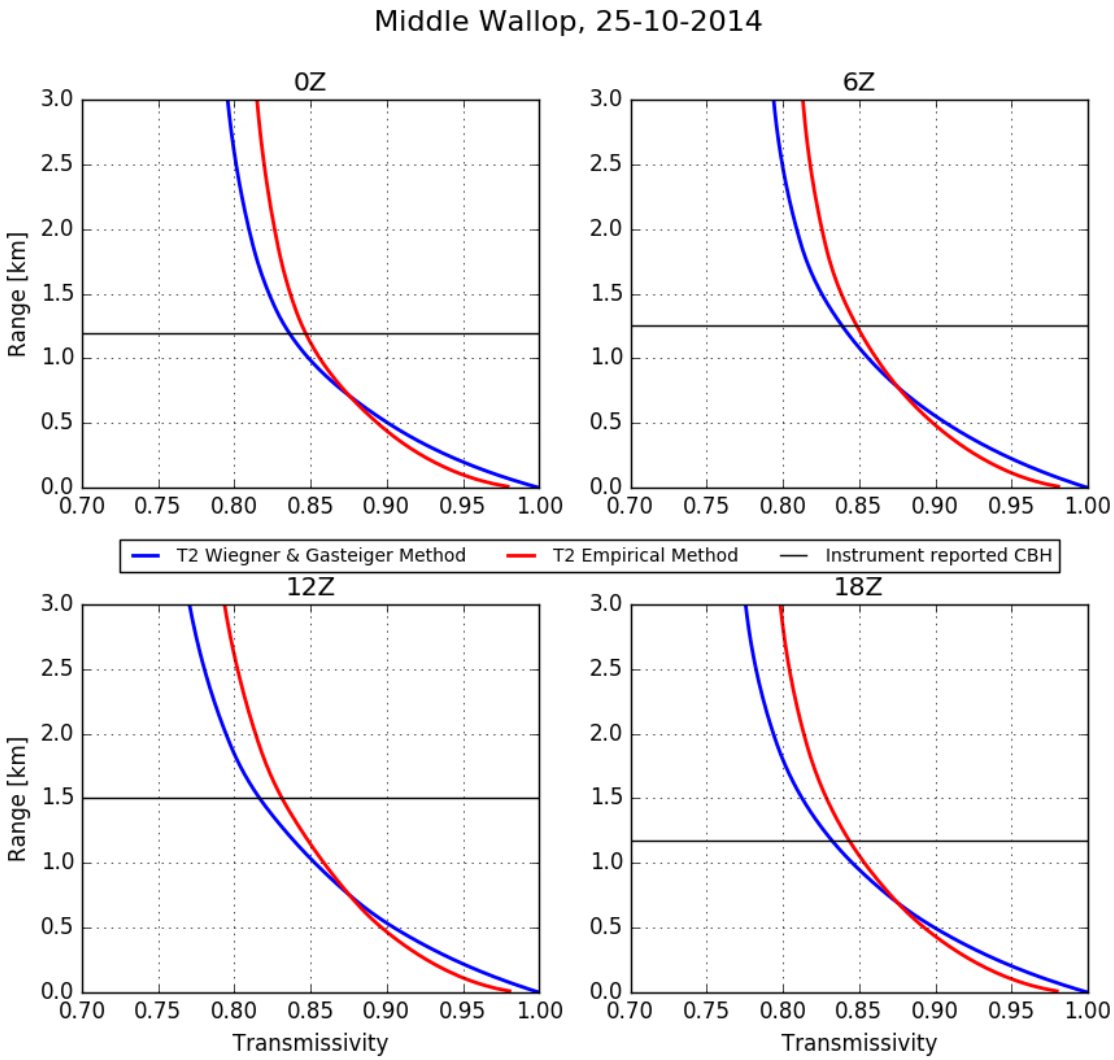

Figure 3.6: Comparison of water vapour transmission correction methods using ECMWF water vapour density profiles for 25th October 2014 at Middle Wallop, England. Each panel represents a time of day (clockwise from top left 0Z, 6Z, 12 Z and18Z). The transmissivity is shown as a profile with values on the x-axis for each range gate (y-axis). The profile calculated using WAPL (Wiegner and Gasteiger, 2015) is shown in blue. The transmissivity profile calculated using the empirical function is drawn in red. The horizontal black lines show the instrument-reported cloud base height at that time.

The water vapour could be estimated using a microwave radiometer. Alternatively, it can be obtained from a numerical weather prediction (NWP) model. In this thesis, the latter approach

is used. Cossu et al. (2015) have compared NWP output with the water vapour path derived from microwave radiometers and find that the mean bias of the NWP water vapour path is only 0.7mm. For the automatic operational calibration of the Met Office ceilometers, water vapour density would be calculated from pressure, temperature and specific humidity profiles output from the Met Office UKV model.

3.4.5 A height constraint for Met Office Vaisala CL31 Ceilometers

For the Vaisala ceilometers in the Met Office network, a cosmetic feature in the firmware suppresses the range correction to the received power for heights above 2.4 km, except when there are clouds present. This is done to avoid the background noise signal leading to apparent clouds at high altitudes that confuse the non-expert. In addition, Kotthaus et al. (2016) found that the attenuated backscatter in the lowest 200 m may be subject to artefacts so, in this calibration study of the Met Office's Vaisala ceilometers the returns above 2.4 km and below 200 m are not used.

Figure 3.7 shows a histogram of the integrated attenuated backscatter, B, from liquid cloud as a function of the height of the maximum attenuated backscatter (used as an indicator of the height of the cloud), for profiles from an uncalibrated Met Office Vaisala CL31 situated at Middle Wallop (51.15° N, 1.57° W). Multiple scattering and water vapour attenuation below the cloud have been taken into account. Over 100,000 profiles from the period September 2014 to December 2015 were used in this histogram. The numbers superimposed on the right side of the plot show the mean and standard deviation at 100m intervals of the range. For 16 of the 21 heights shown, the mean value is 0.021 sr^{-1}. The other 5 gates differ by a maximum of only 0.002 sr^{-1}. This provides confirmation both of the validity of the range dependent multiple scattering correction and of the assumption of constant S for different water clouds.

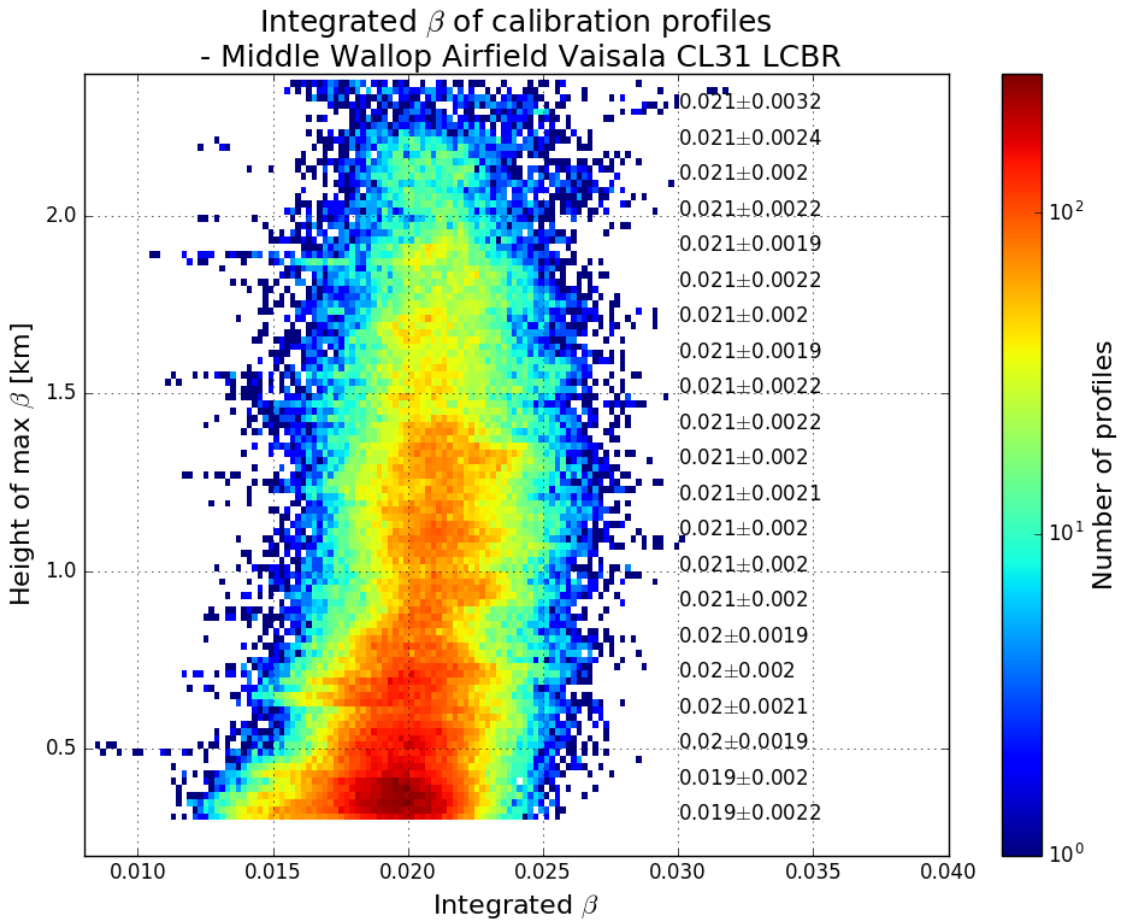

Figure 3.7: 2D histogram of integrated attenuated backscatter with range, with height dependent multiple scattering correction applied. Warmer colours (towards red) indicate a higher density of profiles. The values shown along the right-hand side give the mean +/- the standard deviation of the integrated attenuated backscatter (units sr^{-1}) at 100m intervals.

Below 500 m there is, however, a slight change. The distribution of the integrated attenuated backscatter is still concentrated in a similar region as at other heights, but it also has a slight tail to the left (i.e. lower values of integrated beta). For profiles in this tail region below 500 m, the attenuated backscatter is smaller, which will result in a larger apparent lidar ratio. The mean value of the integrated attenuated backscatter at heights below 500 m decreases by 9.5% while the standard deviation increases by 17%. We suspect that this is a result of the instrument detector saturating. When the cloud base is very low, the cloud signal may be so strong at its

peak (i.e. the peak attenuated backscatter) that the true magnitude of the backscattered signal is not fully detected and, therefore, the integrated attenuated backscatter appears smaller when compared to other heights. Occasionally, this may be due to microphysical processes within the cloud. Nicholls (1984; Powlowska et al., 2000) showed that there is a reduction in droplet number concentration below 450-500 m. Low droplet number concentration may, in some cases, be significant enough to affect the backscatter at this heights below 500 m.

3.4.6 Saturation (1064 nm ceilometers)

Before the cloud calibration can be applied to the Lufft ceilometers, the issue of saturation must be addressed. Due to the greater pulse energy (compared to Vaisala ceilometers), the Lufft ceilometer receivers are much more prone to saturation. When saturation occurs, the backscatter reported for this profile is false – it is too low. Hence, these profiles that saturate need to be detected and rejected from use in the calibration algorithm. The exact magnitude of power at which the Lufft power saturates is an unknown value. However, it is possible to detect the majority of saturated profiles because the saturation of the receiver usually causes the instrument background noise to drop, making the signal appear negative just above the cloud layer (Personal Communication, H. Wille, Lufft, 2017). This is evident in the attenuated backscatter profiles, where there is a region of negative attenuated backscatter above the cloud and a larger fluctuation in the noise compared to an unsaturated profile. This effect of saturation on the backscatter profile is shown in figure 3.8.

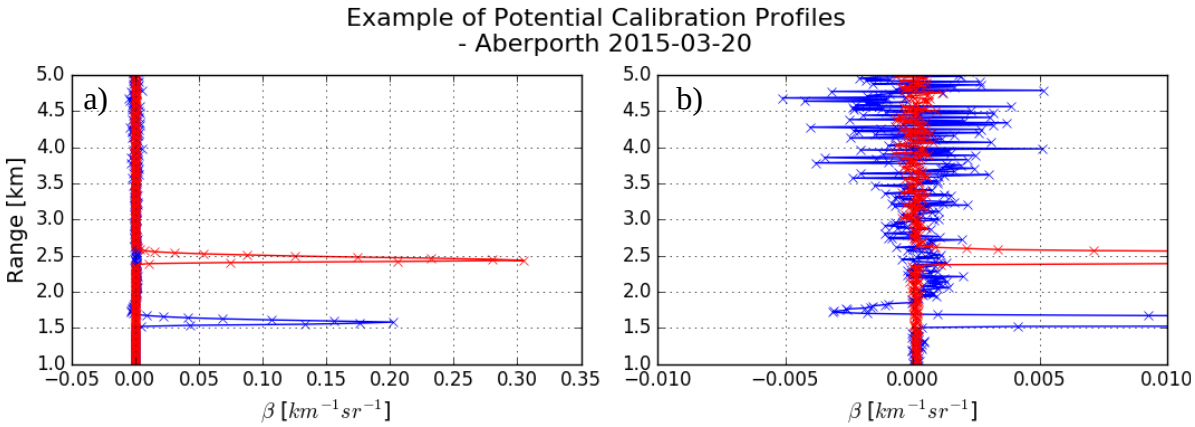

Figure 3.8: Two profiles of attenuated backscatter that detect liquid cloud from the Lufft CHM15k ceilometer at Aberporth on 20th March 2015 (panel b) shows same as panel a) but for a smaller range centred around zero backscatter). The profile in blue has a negative overshoot above the cloud (implying saturation of the detector), whereas the red profile does not.

Figure 3.8a demonstrates the impact of saturation; the blue profile, where saturation has occurred, has a smaller magnitude than the red profile, which is the case where the detector has not saturated. If a saturated profile were to be used for calibration, then the total attenuated backscatter recorded by the ceilometer would appear lower than a non-saturated profile and would therefore systematically skew the calibration coefficient to be larger than it should be. Because the profiles that are recorded when the detector has been saturated have this apparent layer of negative attenuated backscatter, this can be used in the calibration algorithm to detect and reject these profiles. There is a correlation between the negative backscatter and the magnitude of saturation: the larger the negative backscatter value, the greater the magnitude of saturation. However, the relationship is not linear and so the saturation cannot be easily corrected (Personal Communication, H. Wille, Lufft, 2017). Hence, in what follows, we simply filter out such profiles completely. To ensure it is the negative attenuated backscatter of a saturated profile that is detected and not just the random noise in the profile above the cloud

(which appears as small positive and negative values varying randomly from gate to gate), a layer greater than 100 m of negative backscatter is required above the cloud. Profiles that have this negative backscatter for 100 m or more are removed from set of profiles used in the calibration.

This approach removes the majority of saturated profiles. However, those profiles that only just saturate the instrument receiver may not always result in a region of negative attenuated backscatter. To increase confidence that all saturated profiles are being removed, a cloud height threshold can be imposed. Figure 3.9 shows a histogram of the integrated attenuated backscatter for profiles that should be considered by the algorithm for calibration. As discussed for the Vaisala ceilometer calibration (figure 3.7), the integrated attenuated backscatter should be a constant, independent from the height. However, as Figure 3.9 demonstrates, for a Lufft ceilometer, there appears to be a change in the integrated backscatter that is dependent on the height, from 0 km to approximately 2.2 km. Above 2.2 km, although the data is patchy as there are fewer suitable clouds for calibration at these heights, there is also no longer a height dependency; the integrated attenuated backscatter becomes constant. The exact height where the integrated attenuated backscatter becomes constant will be instrument-dependent as it will be affected by instrument power and by the individual receiver. However, with this simple test, the height threshold required can be easily found; thus, allowing for saturated profiles to be removed and calibration to be correctly calculated.

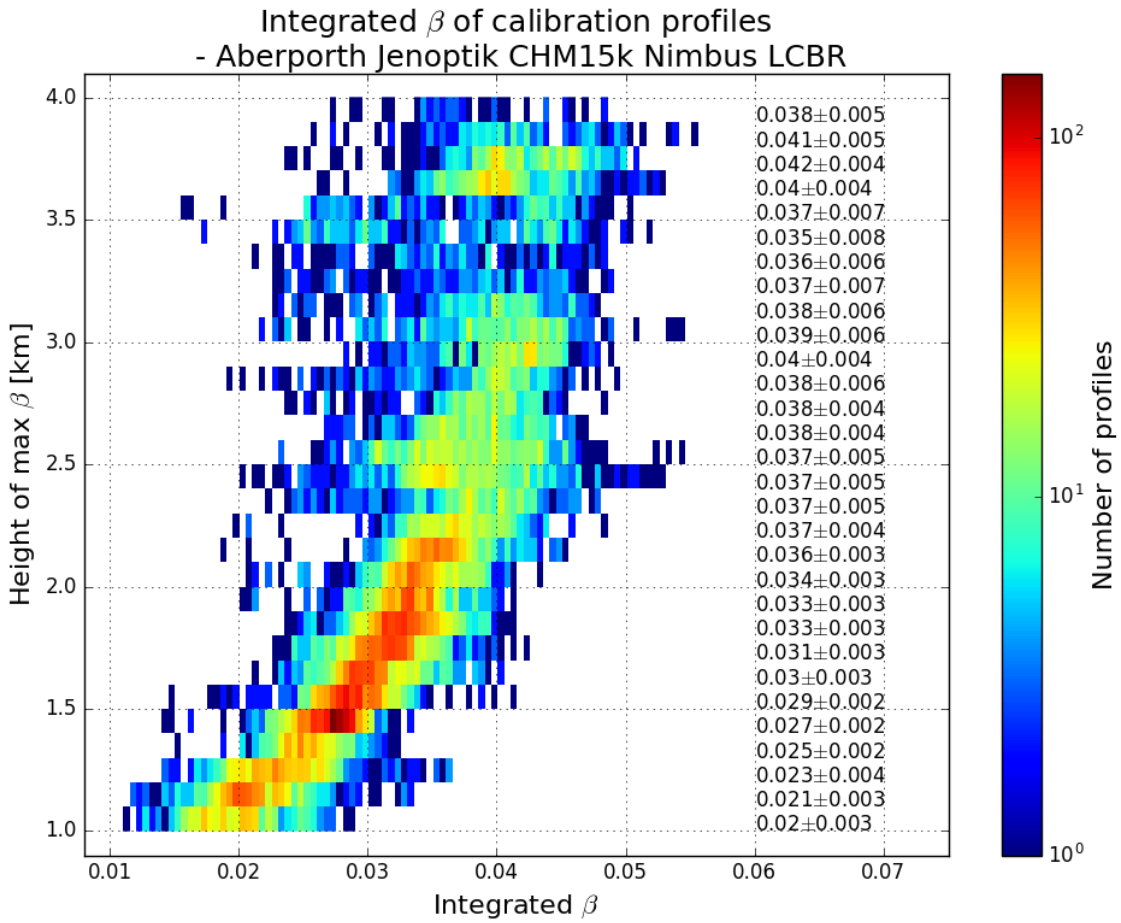

Figure 3.9: 2D histogram of the value of the maximum attenuated backscatter in profiles used for calibration with range. A height dependent multiple scattering correction has been applied. Warmer colours (towards red) indicate a higher density of profiles. The values shown along the right-hand side give the mean +/- the standard deviation of the integrated attenuated backscatter (units sr^{-1}) at 100m intervals.

3.5 Automating the calibration

A new algorithm has been designed to automatically sift through all profiles of attenuated backscatter. This method uses a strict set of criteria to select only those profiles that are suitable for use in calibration. The method is fairly simple ensuring it may be applied operationally with minimal impact on processing time. No absolute values of attenuated backscatter are required

by the algorithm to evaluate the criteria below; thus, so the instrument can be completely uncalibrated, or the instrument could be calibrated but the current calibration could have a large error. There are two main sets of criteria that must be met by a profile of attenuated backscatter for it to be used in the calibration algorithm:

1. Unsuitable individual profiles:
    a. Aerosol filter – In any single profile, if the aerosol under the cloud contributes more than 5% to the total integrated backscatter (as shown in Fig. 2b), this profile is removed from the calibration. The transmission through the aerosol below the cloud attenuates the ceilometer beam, and this attenuation increases with greater concentrations of aerosol. If the aerosol has a lidar ratio value twice the value assumed for cloud droplets, then this filter will limit the calibration error to a maximum of 5%.
    b. Peak sharpness filter – The peak backscatter magnitude must be a factor of 20 greater than the value 300 m above and below that peak. A liquid water cloud suitable for calibration must fully attenuate the ceilometer beam; therefore, the backscatter values should decrease rapidly in the gates immediately above the peak value. Additionally, drizzle or rain below the cloud may give a large backscatter signal backscatter and, like the aerosol, will distort the apparent lidar ratio. Hogan et al. (2003) report that individual liquid-water layers do not tend to occupy more than 300 m of the ceilometer profile, due to their strong attenuation. Our own observations of the data lead to the same conclusion. This filter should therefore remove profiles that do not fully attenuate the beam and that contain drizzle or rain.

c. Window transmission and pulse energy check – A check is made on the recorded instrument transmission (given as a percentage of how much of the instrument window is clear) and on the reported pulse energy (given as a percentage of a nominal amount). Both of these conditions can affect the true value of attenuated backscatter. Periods affected by reduced window transmission and/or reduced pulse energy are filtered out at a threshold of 90% or less.

2. Consistency of neighbouring profiles

   a. Lidar ratio stability – This filter traps errors due to patchy cloud cover or drizzle that may not have been identified by the first filter by checking that the apparent lidar ratio is the same as its nearest neighbours (i.e. the profiles either side in time). The recommendation is to compare to 3 profiles either side in time; however, if the ceilometer is at a site where liquid water cloud is infrequent such as Gibraltar, this could be reduced to 1 or 2 profiles either side, with the consequence of degrading the accuracy of the calibration coefficient.

The operation of these filtering procedures in removing unsuitable profiles is illustrated in Figure 3.10a), where a stratocumulus cloud layer located at about 1 km persists for the whole day resulting in an ideal scenario for calibration. The liquid cloud backscatter signal, which has values greater than 0.3 km^{-1} sr^{-1} (in the red region of the colour scale), appears as a thin layer and has only noise above. Visible with the noise is the superposed diurnal cycle of sunlight. The noise in the data is visible as speckling, and is of the order of less than 0.001 km^{-1} sr^{-1}. There are also limited periods of broken, patchy cloud, which are identifiable by breaks in the

layer of high backscatter and limited periods of drizzle which is identifiable by the streaking (cyan colours of the order 0.003 km^{-1} sr^{-1}) below the cloud.

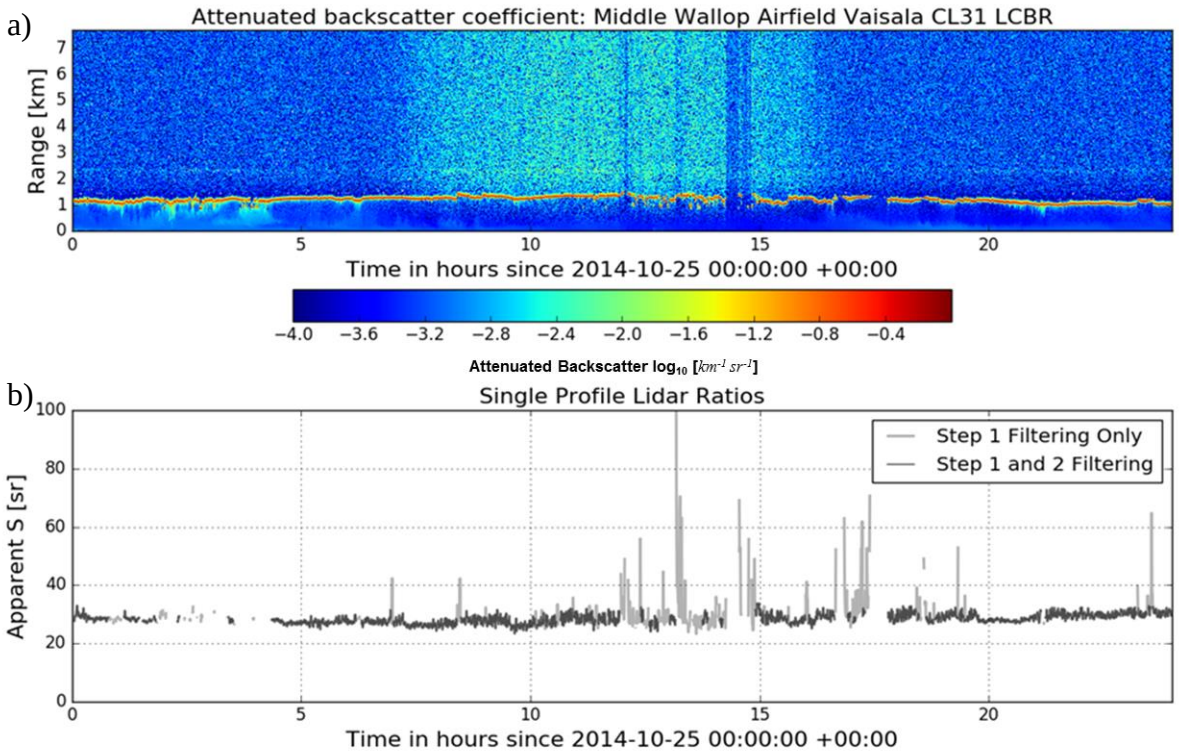

Figure 3.10: (a) Uncalibrated attenuated backscatter vertical profiles (colours shown on a log scale) for 25th October 2014 from a CL31 ceilometer at Middle Wallop airfield (51.1489 N, 1.5700 W) and (b) the apparent lidar ratio for the same day. In panel (b), the grey line shows the apparent S for profiles that pass the step 1 filtering of the calibration algorithm and the black line shows the profiles that pass the step 2 filtering and are used to calculate the calibration coefficient.

Figure 3.10b) illustrates the two main filtering steps of the new calibration algorithm. The thick, light-grey line shows the apparent S values for each indiviudal profile that are acceptable. Profiles between 3:30 – 4:30 hours where there is drizzle and aerosol below the cloud base are removed. The filtering leaves some large apparent S values from 12:00 -15:00 hours that are due to broken cloud that does not totally extinguish the ceilometer return. The second filter checks for consistency between neighbouring profiles and it successfully identifes and removes these spurious profiles where there is broken cloud.

The remaining profiles (i.e. those in black in figure 3.10(b)) give the values of apparent S (S_{app}) which would be used to calculate C using equation 3.1 (where $C = \frac{S_{app}}{S}$, see Appendix A). It is evident that these values remain nearly constant over the course of the day, implying that the calibration of the intrument is very stable on this time scale. This is important, since our method can only be applied to cloudy conditions, which may be separated by intervals of several days. The stability of C implies that we can interpolate between calibration events.

3.6 Conclusion

This chapter has presented a robust algorithm to calibrate ceilometers based on the cloud calibration technique (O'Connor et al., 2004) that relies on the fact that the lidar ratio of liquid water clouds is a known constant. This new method can be run operationally, removing unsuitable profiles where the cloud does not fully attenuate the ceilometer beam or where there is significant backscatter from aerosols. By excluding profiles when the low cloud leads to instrument saturation (particularly in the Lufft instruments) or when the window transmission is low, and by accounting for the attenuation of the ceilometer beam by water vapour (in the Vaisala instruments), ceilometers from different manufacturers can be successfully calibrated using this method. Application of this calibration is analysed in the next chapter

Chapter 4:

Calibration results for the Met Office ceilometer network

4.1 Introduction

In the previous chapter, the theory and method of the calibration algorithm was presented, using the ceilometer 30 s vertical profiles of attenuated backscatter. The method relies on using the integrated backscatter (B, where $B = \int_0^r \beta(r)dr$) from liquid clouds that totally extinguish the ceilometer signal: B is inversely proportional to the lidar ratio (S) of the backscatter to the extinction for cloud droplets. The calibration technique involves scaling the observed attenuated backscatter (β) so that B matches the predicted value for S for cloud droplets, which is 18.8 ± 0.8 sr at ceilometer wavelengths (905-1064 nm). For accurate calibration, care must be taken to exclude any attenuated backscatter profiles having targets with different values of S, such as drizzle drops and aerosol particles, attenuated backscatter profiles that do not totally extinguish the ceilometer signal, attenuated backscatter profiles with low cloud bases that saturate the receiver, and any attenuated backscatter profiles where the window transmission or the lidar pulse energy is low. A range dependent multiple scattering correction that depends on the ceilometer optics should be applied to the profile. A simple correction for water vapour

attenuation for ceilometers operating at ~910 nm wavelength is applied to the signal using the water vapour profiles from a forecast analysis. The ceilometer models operating at 1064 nm, such as Lufft ceilometers, are unaffected by water vapour attenuation, but are more prone to saturation in liquid clouds. Reliable calibration is still possible, provided the clouds used are above a certain altitude. The threshold is instrument dependent but is typically around 2 km. A characteristic signature of saturation of the ceilometer receiver by liquid water clouds has been identified, and used to remove any profiles with this signature.

The following chapter discusses the results of the calibration when the algorithm is applied to the Met Office ceilometer network. Examples of the calibration of individual ceilometers are presented and the stability over time analysed. As the calibration has to be applied slightly differently depending on the wavelength of the instrument, the results are split into the Vaisala ceilometers and the Lufft ceilometers. A comparison of two collocated ceilometers (one Vaisala and one Lufft) is then shown.

4.2 Vaisala CL31 ceilometers (~910 nm)

4.2.1 Middle Wallop ceilometer

The ceilometer in Middle Wallop, Hampshire, is one of the twenty-six Met Office Vaisala CL31 ceilometers recording the full backscatter profiles. Figure 4.1 shows a time series of the calibration results for the CL31 at Middle Wallop over a period of 20 months. Panel (b) shows the mode of the calibration coefficient C, constructed for each day with sufficient attenuated backscatter profiles deemed suitable by the calibration algorithm. For example, the black cross on 25 October 2014 is the mode of the calibration coefficients calculated from the filtered S values (per attenuated backscatter profile) shown (in black) in figure 3.10b.

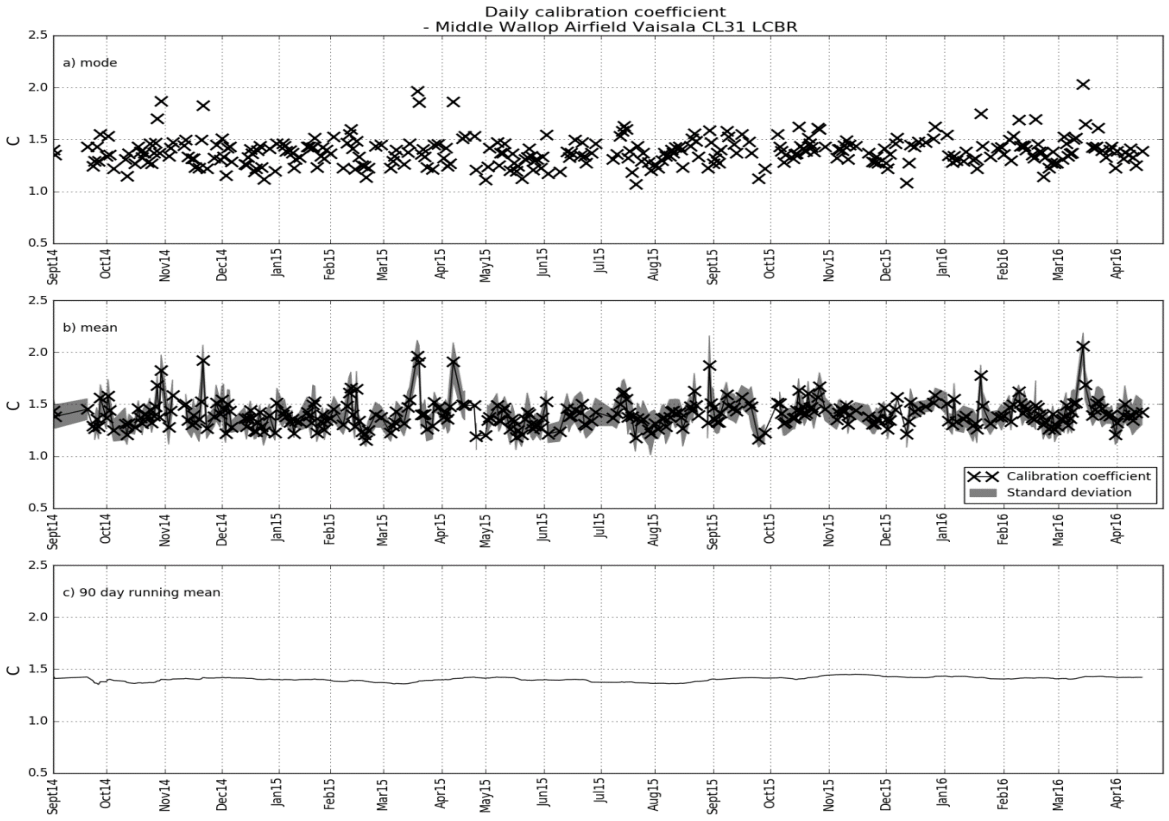

Figure 4.1: Calibration Coefficient (C) for Middle Wallop CL31 from September 2014-April 2016. Each black cross represents a single day, calculated from profiles deemed suitable by the calibration algorithm. Panel a) shows the mode of C for each individual day, b) shows the mean of C for each day, with the standard deviation shaded in grey and c) shows a 90 day running mean for the 20-month period. The average of the daily modes is 1.38 ± 0.14, the average of the daily means is 1.41 ± 0.13 and the average of the 90-day running means is 1.40 ± 0.021.

The results are for almost two years of data and establish that the calibration remains stable over time. The number of profiles used for the calculation of the daily value is different depending on the occurrence of cloud on each day. As the calibration algorithm requires only a minimum of 10 profiles to be included in the daily value of the mode, even a short period of cloud will be included for calibration purposes. This ensures that the technique can be applied to ceilometers in locations with climates that seldom have weather with consistent low level

liquid water cloud. At Middle Wallop, the algorithm found a minimum of 8 days every month with profiles suitable for calibration, with slightly more suitable days during autumn and winter. The water vapour correction profiles are calculated from the Met Office UKV model at the grid point over the Chilbolton Observatory, which is approximately 15 km from Middle Wallop. The variables needed to calculate the transmission profiles were available every hour, and have been interpolated to the observation time.

Panel b) of Figure. 4.1 shows the daily mean and standard deviation for Middle Wallop. For the 20-month (574 days of data available) period, a calibration was possible on 320 days, or 56% of the days, and the average number of profiles per day was 292. There were just 7 days out of the 320 when both the mean and mode of the calibration coefficient, C, was closer to 2.0 rather than the median value of 1.4. Assuming the distribution of C to be Gaussian, it would be expected that 2.5% of the sample would be more than 2 standard deviations from the mean, as is shown by these 7 profiles.

A 90-day running mean was also calculated and is displayed in figure 4.1c. This running mean had a value of C of 1.40 with a standard deviation of 0.021; this is less than 2% of the mean. As both the mean height of the cloud base (and therefore the amount of multiple scattering) and the water vapour attenuation have a pronounced annual cycle, this low value of standard deviation is evidence of the appropriateness of the algorithms that correct for these two effects. Accordingly, it is recommended that for automatic, operational use for a ceilometer, without window transmission or pulse energy issues, a 3-month running average of the calibration coefficient be used.

4.2.2 Gibraltar

Figure 4.2 shows the calibration of the Gibraltar CL31 ceilometer and has the same format as figure 4.1, for 12 months at Gibraltar rather than the 20 months at Middle Wallop. Because the

domain of the UKV model does not include Gibraltar, the water vapour correction was calculated using data from the Met Office global Unified Model (UM) which at this time was a ~17 km horizontal resolution model with a convective parameterization (Wilkinson et al., 2009).

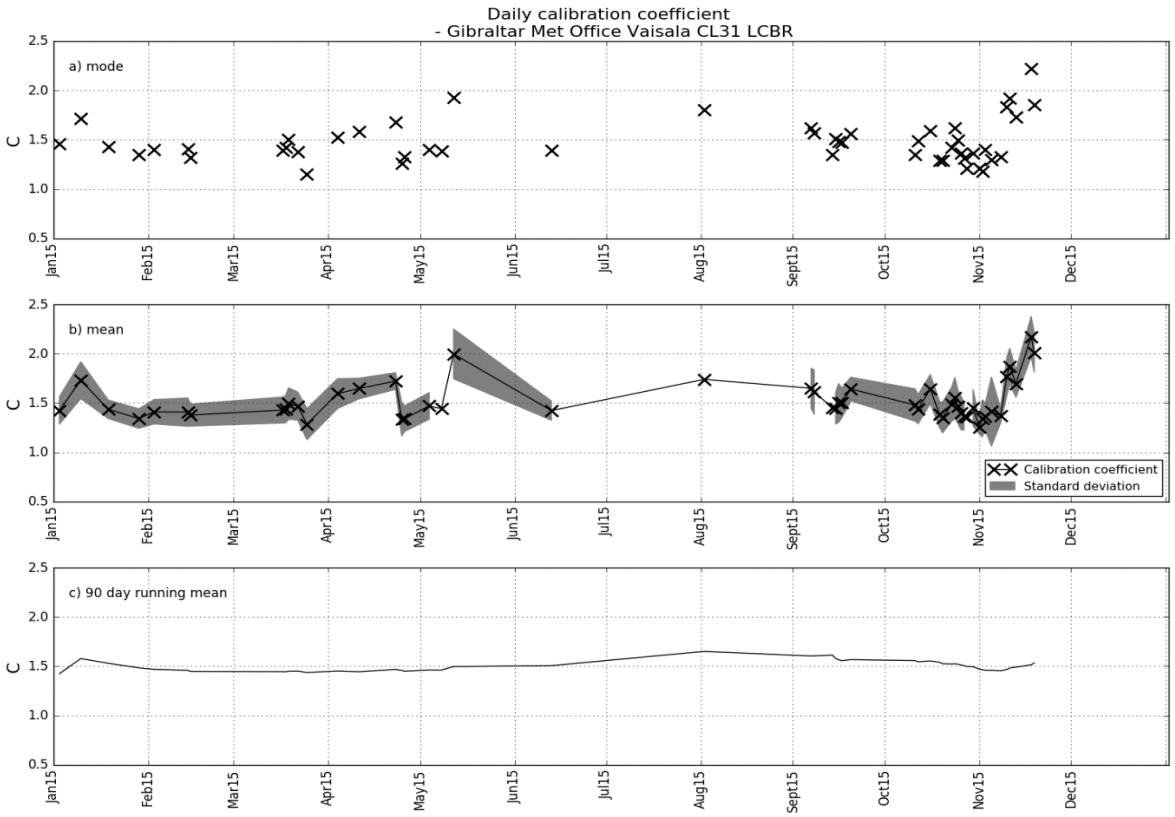

Figure 4.2: Calibration Coefficient (C) for Gibraltar Vaisala CL31 from January-December 2015. Each black cross represents a single day, calculated from profiles deemed suitable by the calibration algorithm. Panel a) shows the mode of C for each individual day, b) shows the mean of C for each day, with the standard deviation shaded in grey and c) shows a 90 day running mean for the 12-month period. The average of the daily modes is 1.48 ± 0.21, the average of the daily means is 1.51 ± 0.19 and the average of the 90-day running means is 1.50 ± 0.053.

Due to the Mediterranean climate, the number of occasions when there are suitable clouds for calibration is reduced at the Gibraltar site. In one year there were 51 days of suitable clouds,

with each day having, on average, 128 profiles. However, from mid-May to mid-Sept. there were only two days where calibration was possible and in December there were none. While this is in part due to a lower amount of stratocumulus compared to the UK, it was also caused by a reduction in the window transmission. The Gibraltar ceilometer requires regular cleaning as dust tends to build up on the window, reducing the transmission. Therefore, several days where the window transmission dropped below 90 % have been filtered out by the algorithm. The 4 crosses in figure 4.2a and figure 4.2b, which show a calibration coefficient closer to 2.0, correspond to days where the profiles only just pass the 90 % window transmission check.

Nevertheless, figure 4.2 confirms that the 90-day running mean calibration coefficient, C, over the twelve month period was 1.5 with a standard deviation of 0.05, or about 3%. As with the data in figure 4.1, there is no sign of an annual cycle in the calibration coefficient.

4.2.3 Met Office Vaisala Ceilometers

The calibration of all the Vaisala CL31 ceilometers in the Met Office network has been collated and is summarised in figure 4.3, where box and whisker plots are shown of the calibration coefficient for each of the CL31s, calculated from data for the period January – March 2015. All instruments have a calibration coefficient larger than 1.0, with the majority of the instruments having a coefficient of around 1.5. When C is greater than 1.0, this means that the ceilometer attenuated backscatter is too low. If C is less than 1.0, the ceilometer attenuated backscatter is too large. If C is equal to 1.0, the ceilometer attenuated backscatter is at the correct magnitude.

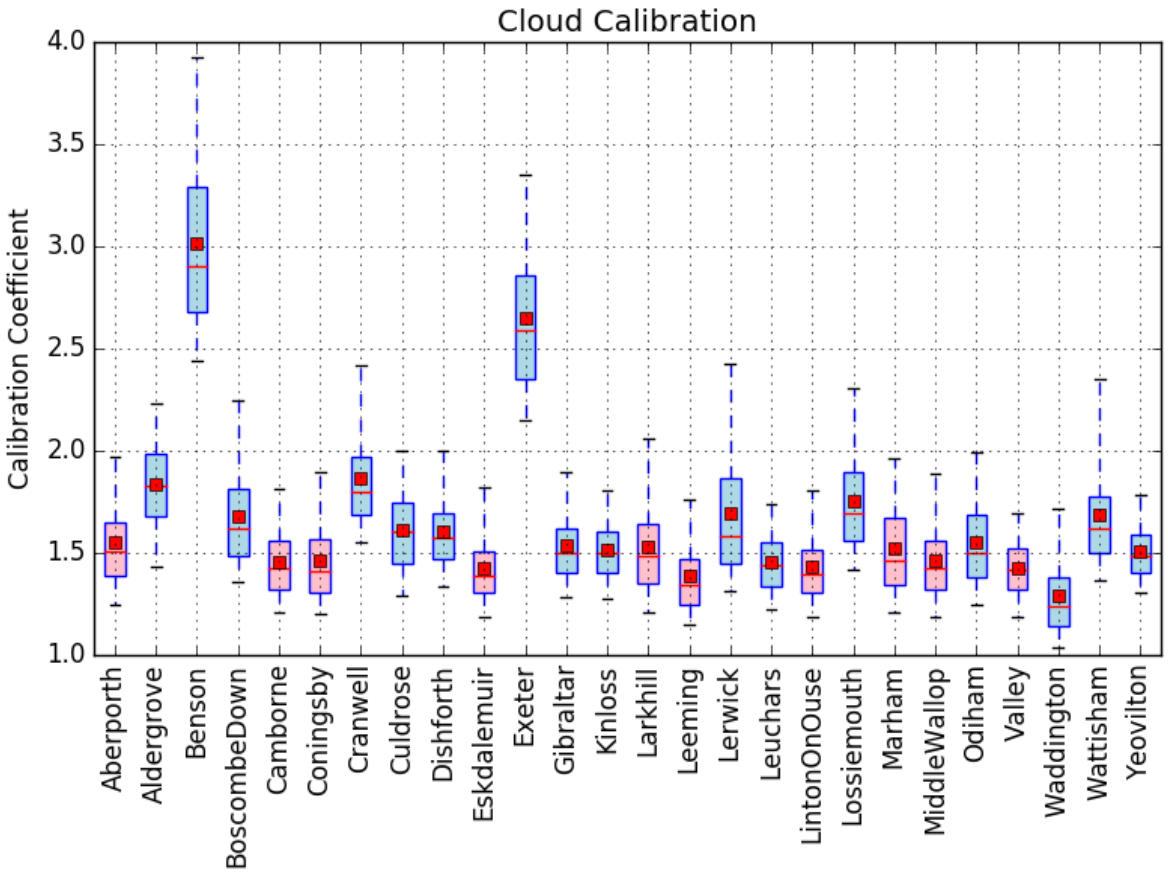

Figure 4.3: Calibration coefficient for each of the CL31 ceilometers in the UK Met Office network. 3 months of data (January-March 2015) have been used for each instrument. The number of suitable vertical profiles of attenuated backscatter that were used to compute the calibration coefficient (C) shown will be dependent on occurrences of cloud and, therefore, will vary for each instrument. The box outline represents 50 % of the values of C derived from the vertical profiles of attenuated backscatter and the whiskers extend to include 95% of the profiles (outliers have been excluded from plot). The horizontal red line in the box shows the median calibration coefficient and the smaller, filled box shows the mean. The boxplot is shaded by firmware version as given by the ceilometer files on 1st January 2015: pink for version 202 and blue for versions 170 and 172.

The range of coefficients for each station is small, with 50% of the data (contained within the box) being within 10% of the mean value. The colour code in figure 4.2 indicates the different

firmware versions installed on the instruments within the Met Office ceilometer network. Stations using the 2.02 firmware, which are shaded pink (for example, Aberporth, Coningsby, Middle Wallop), tend to have an even smaller range of C values, with 50% of the data being within 8% or less of the mean. The network includes stations from Lerwick (60.16°N, 1.15°W) down to Gibraltar (36.14°N, 5.35°W), demonstrating that the calibration method has been successfully applied to a range of different climates, from the North Sea down to the Mediterranean Sea.

The water vapour correction of the data has been applied to the vertical profiles of attenuated backscatter before C is computed in figure 4.3, as described in section 3.4.4. Ideally, the water vapour profiles for each specific site should be used to calculate the transmission correction. However, because the calibration specifically requires a cloud base below 2.4 km and the air is generally well-mixed below cloud base, the water vapour below the cloud is generally fairly constant and depends on the temperature and height of the cloud base. Only the UKV NWP model data for Chilbolton was available at this time. Therefore, it is assumed that the season is more important than the location and so the same water vapour profiles are used for all the ceilometers and in this study the UKV NWP model data for Chilbolton was used for all UK sites. For future, operational implementation, the site specific water vapour profile should be used.

4.3 Lufft ceilometers (1064 nm)

4.3.1 Aberporth

The calibration algorithm is applied to the Lufft ceilometers in a similar way to the Vaisala ceilometers. Differences include a saturation check on the Lufft attenuated backscatter profiles (as described in Section 3.4.6). A couple of additional changes to the method are needed in order to apply it to the Lufft ceilometers. Unlike the Vaisala ceilometers, the Lufft ceilometers

are not restricted by a change in processing at 2.4 km, so the upper range limit of integration to compute B is increased to 4 km, which incorporates the vast majority of liquid clouds in the UK. Additionally, the higher cloud range means the ceilometer beam must travel through a larger portion of the atmosphere, so the ratio filter (criteria 1a – see chapter 3, section 3.5) is increased from 5% to 10%. Note that this may lead to a slightly larger uncertainty in C, but this is done to decrease the amount of data that would otherwise be filtered out by the criteria. The lower height limit on the cloud base height is also changed to 1 km. This is to avoid using attenuated backscatter in the range gates where an overlap correction is applied; there is potentially a temperature dependency in the overlap function that has not been accounted for (Hervo et al., 2016).

At the 1064 nm wavelength there is no absorption by the water vapour molecules; so no water vapour correction is required. Figure 4.4 shows an example of the cloud calibration applied to a Lufft ceilometer situated at Aberporth, West Wales, for the twelve months of 2015. Because of the requirement to remove the low level clouds that resulted in saturation of the ceilometer receiver, calibration was only possible on 70 days or about 20% of the days. Each day had an average of 58 profiles; nevertheless, the 90-day running mean of the calibration coefficient over 2015 was 0.48 with a standard deviation of 0.02 or 4%. There was no sign of an annual cycle. This standard deviation of 4% over the year is slightly higher than for the Vaisala ceilometers, probably because of the relaxation of the threshold for aerosol to be considered negligible, but is well within the specified requirement of 10% as stated in chapter 3, section 3.1.

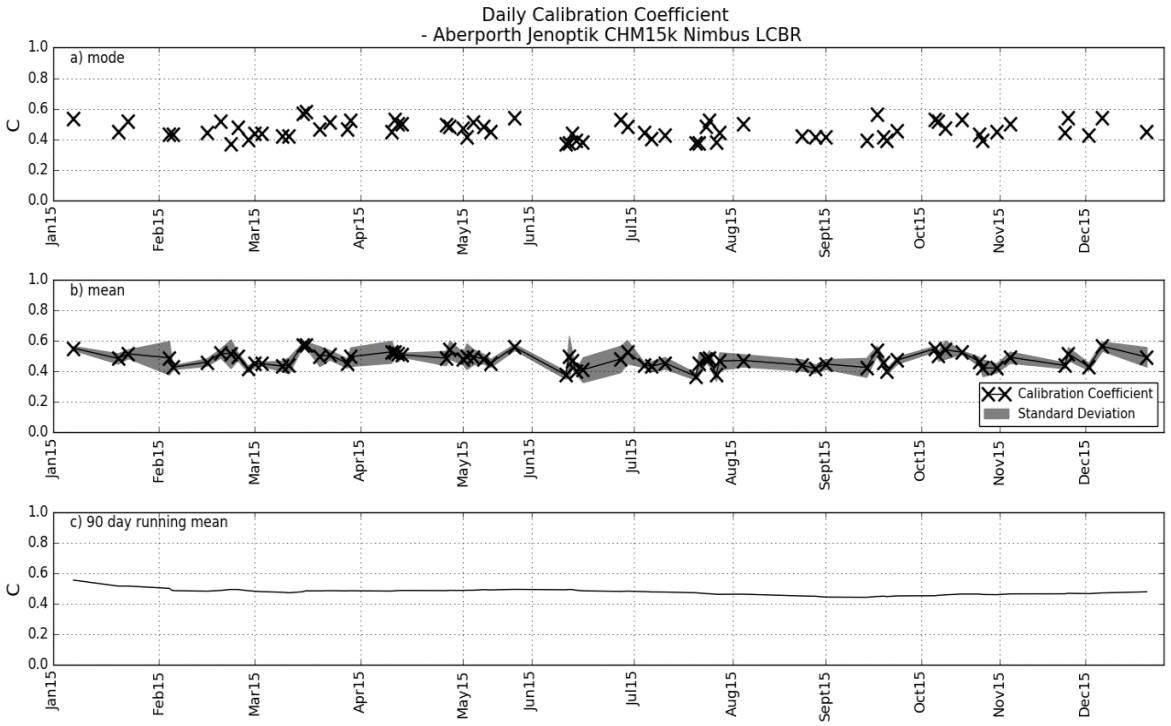

Figure 4.4 : Calibration coefficients for the Lufft CHM15k nimbus ceilometer at Aberporth (52.06° N, 4.33° W). Each black cross represents a single day, calculated from vertical profiles of attenuated backscatter deemed suitable by the calibration algorithm (see cection 3.5). Panel a) shows the mode of C for each individual day, b) shows the mean of C for each day, with the standard deviation shaded in grey and c) shows a 90-day running mean for the 12-month period. The average of the daily modes is 0.46 ± 0.05, the average of the daily means is 0.48 ± 0.05 and the average of the 90-day running means is 0.48 ± 0.02.

4.3.2 Met Office Lufft Ceilometers

The calibration has been applied to the rest of the Lufft ceilometers in the Met Office ceilometer network, as shown in figure 4.5. Most of the sites have a calibration coefficient of less than 1.0; however, Coningsby has a particularly large calibration coefficient. This highlights the importance and need for a calibration of each instrument. For each site, the relative standard deviation over the 3 month period is small.

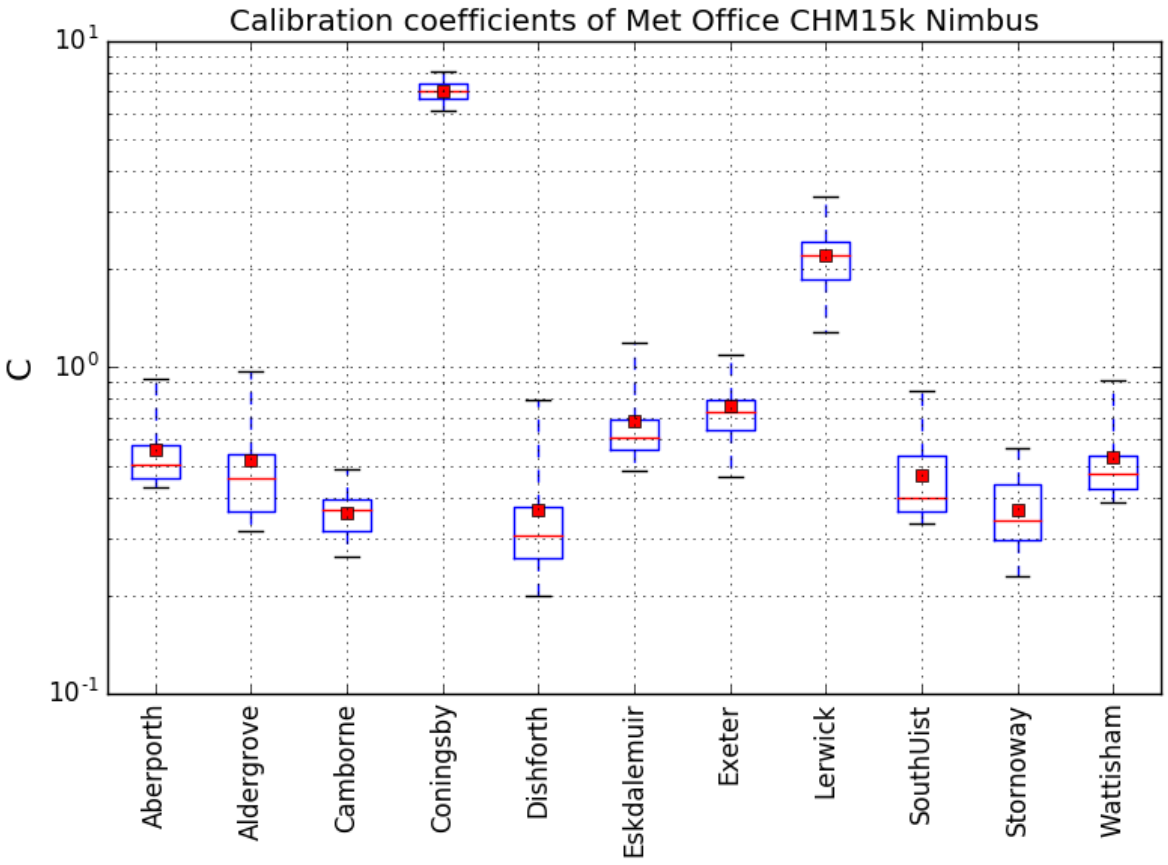

Figure 4.5: Calibration coefficient for each of the Lufft CHM15k Nimbus ceilometers in the UK Met Office network. 3 months of observations (January-March 2016) have been used from each instrument. The number of suitable calibration coefficients(C) from attenuated backscatter profiles will depend on the occurrence of liquid water cloud and, therefore, will vary for each site. The box outline represents 50 % of the values of C derived from the vertical profiles of attenuated backscatter and the whiskers extend to include 95% of the daily C values (outliers have been excluded from plot). The horizontal red line in the box shows the median calibration coefficient and the smaller, filled red box shows the mean.

4.4 Vaisala and Lufft Comparison

The majority (9 out of 11) of the Lufft ceilometers are collocated with a Vaisala ceilometer, allowing comparisons between the two types of ceilometers. Figure 4.6 compares the

observations of vertical profiles of attenuated backscatter from the two ceilometers at Aberporth, which have both been calibrated using the cloud method. To make a fair comparison between the two instruments, it is necessary to choose the meteorological situation carefully. Aerosols are problematic, because the ceilometers operate at different wavelengths, and the backscatter from aerosols is wavelength-dependent in a way that we do not know *a priori*. We could analyse attenuated backscatter profiles in liquid clouds; however, we have already used these for calibration (so it would not be a truly independent test). In addition, the attenuated backscatter profile in liquid clouds contains very large gradients with respect to height which make any comparison extremely sensitive to small offsets in range and/or differences in vertical spacing of the gates between the two instruments. Rain profiles could potentially be used for the comparison: however, rain which reaches the ground may wet the telescope optics of the ceilometer and affect the data collection.

Better targets for such comparisons are drizzle drops and ice particles. These particles are large compared to the wavelength of the ceilometers, and hence the scattering is almost wavelength-independent, since we are close to the geometric optics regime (Weitkamp, 2005). At the same time, the extinction of the lidar beam is much more gradual when detecting drizzle than in liquid cloud, providing smoothly varying backscatter profiles, which can be interpolated onto a common vertical grid with little error. If we use an ice case, we would need to account for the influence of specular reflections from oriented ice crystals (e.g. Westbrook et al 2010a). Therefore, in this example, a drizzle event has been chosen.

To establish quantitatively whether the attenuated backscatter for drizzle drops at 1064 and 910nm are actually equal, Mie calculations from Westbrook et al. (2010b) were used, which assume Gamma drop size distributions; for the number concentration of drops dN with diameters between D and $D + dD$,

$$\frac{dN}{dD} = N_0 \left(\frac{D}{D_0}\right)^{\mu} \exp\left[-(3.67 + \mu)\frac{D}{D_0}\right] \qquad \textit{(Eq. 4.1)}$$

Where D_0 is the diameter of the median volume drop, μ is a dimensionless parameter controlling the shape of the distribution and N_0controls the total concentration of drops for a given (D_0, μ). The results show that the attenuated backscatter at 1064nm is very similar to that at 910nm, but systematically smaller. The differences are very modest: between 5 and 8% for D_0 in the range 0.1-0.6mm, with most of the calculated values in this range close to 7%. Meanwhile the extinction is essentially identical for both wavelengths. Thus, if the calibration has been successful it would be expected that the backscatter profiles during a drizzle episode would match very closely; however the attenuated backscatter values from the Lufft ceilometer would be systematically 7% smaller than the Vaisala, if no adjustment to account for the different wavelengths is made. Therefore, for this comparison, the Vaisala liquid water cloud attenuated backscatter values have been reduced by 7%.

It is also necessary to consider the various technical issues already discussed in Chapter 3 when selecting profiles, in particular the need for the drizzle to be occurring high enough in the atmosphere to be in the region of complete overlap for the Lufft instrument, and below the 2.4km critical height threshold, above which the Vaisala ceilometer attenuated backscatter range correction is variable. Therefore, the data used covers the period 00.00 to 15.00 GMT on 22nd April 2016, during which time there is drizzling cloud. The data are 10-minute averages of attenuated backscatter between 1.0 and 2.4 km and the Vaisala data has been re-gridded from 20 m resolution to 15 m resolution using linear interpolation. The time-height plots of the attenuated backscatter for the Vaisala and Lufft ceilometers are shown in figure 4.6a and figure 4.6b, respectively.

Figure 4.6c shows that there is a strong correlation of 0.95, close to the 1:1 line, between the two ceilometers, as the intercept is close to zero and the slopes differ by less than 10%.

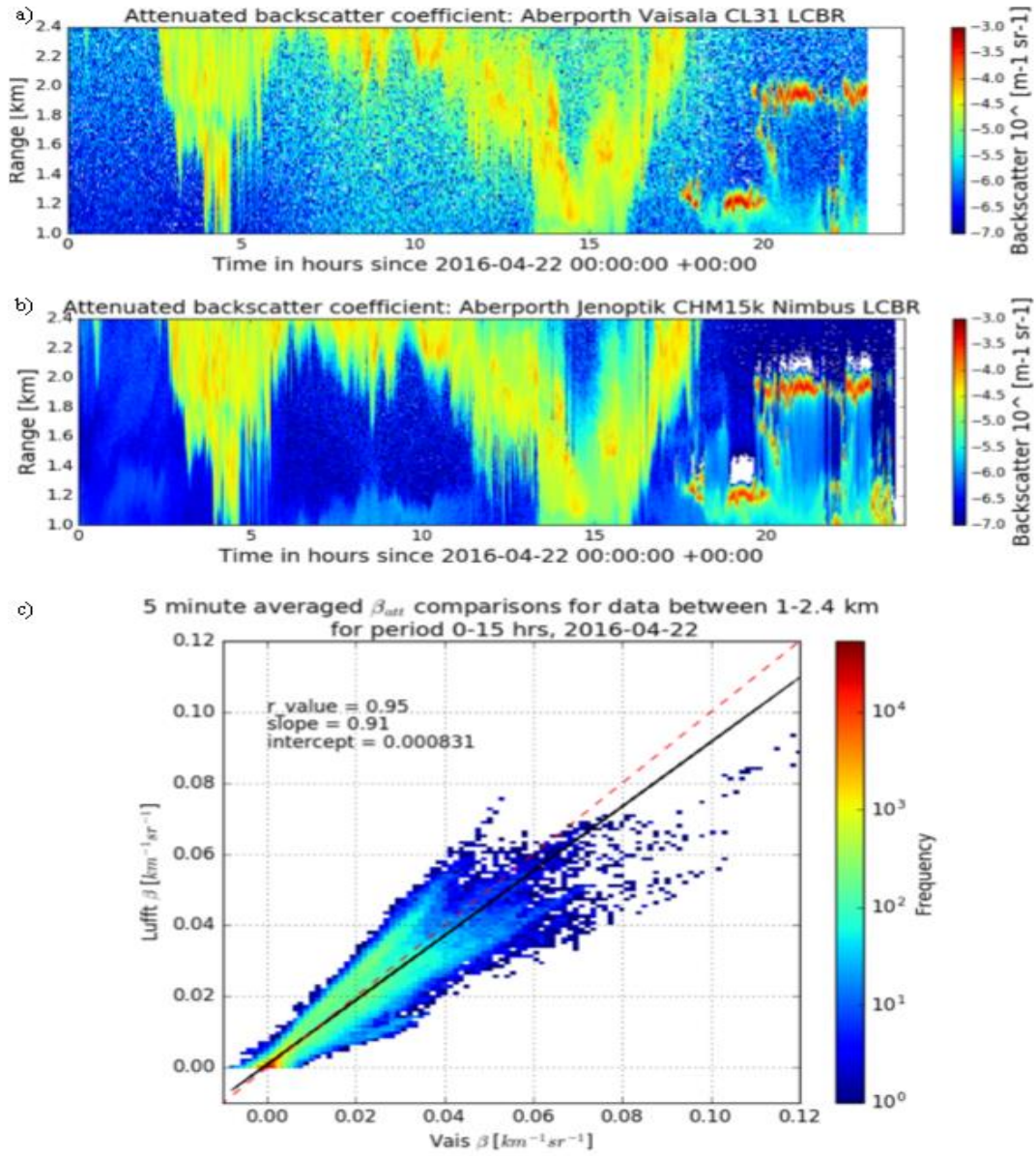

Figure 4.6: Time-height plots of the observed attenuated backscatter between 1 and 2 km are shown for the (a) Vaisala ceilometer and the (b) Lufft ceilometer. Panel (c) shows 5-minute averaged attenuated backscatter values for the Vaisala versus the Lufft ceilometers situated at Aberporth for 22/04/2016 between 0-15 GMT. Colour scale indicates the number of data points. Vaisala attenuated backscatter has been corrected for water vapour attenuation and difference in wavelength, and has been interpolated to match the resolution of the Lufft ceilometer. The black line shows the linear fit of the data and the dashed red line is the 1:1 line. Linear regression parameters are listed on panel (c).

The spread of the individual data points is rather larger than 10 %. Because the Vaisala attenuated backscatter was interpolated onto the Lufft attenuated backscatter grid, it is expected that there would be some added error due to interpolation.

This comparison of the two different types of ceilometers confirms the reliability of this calibration method – the two independently calibrated ceilometers, each with their own challenges (e.g. water vapour, receiver saturation), are consistent with each other. This result is important for an operational network such as the Met Office ceilometer network because it helps maintain a reliable, comparable stream of calibrated data, with water vapour and receiver saturation successfully accounted for, from each instrument at each site.

4.5 Conclusion

This chapter has presented examples of applying the cloud calibration algorithm, which relies on the fact that the lidar ratio of liquid water clouds is a known constant. By excluding profiles when the low cloud leads to instrument saturation (particularly in the Lufft instruments) or when the window transmission is low, and by accounting for the attenuation of the ceilometer beam by water vapour (in the Vaisala instruments), we show that ceilometers from different manufacturers can be successfully calibrated using this method. It has been demonstrated that the running 90-day mean calibration coefficient for each instrument over a year is constant to better than 5% with no detectable annual cycle. At the time of writing, profiles from 200 ceilometers from 17 countries are being distributed in near real time by the E-Profile programme of European Meteorological Services Network (EUMETNET) with the number expected to rise to about 700. E-Profile has decided to calibrate the Vaisala ceilometers using the cloud calibration technique described in the previous chapter.

Chapter 5:

Developing an attenuated backscatter forward model for ice cloud

5.1 Introduction

In the previous chapters, the theory, method and results of the calibration algorithm were presented. The method relies on using the integrated backscatter (B) from liquid clouds that totally extinguish the ceilometer signal; B is inversely proportional to the lidar ratio (S) of the backscatter to the extinction for cloud droplets. By using this calibration algorithm, meteorological organisations, such as the Met Office, can extend the use of pre-existing networks of ceilometers from being simple cloud base height recorders to having the following capabilities: validating the representation of clouds in operational numerical weather prediction (NWP) models (Illingworth et al., 2015), aerosol profiling (Markowicz et al., 2008; Madonna et al., 2015), providing fog observations (Dupont et al., 2012) and retrieving mixing height levels (Münkel et al., 2007).

This chapter presents an example of a novel use of a calibrated ceilometer: the assessment of the representation of ice clouds in the Met Office's UKV model, a convection-permitting variable resolution regional model run operationally over the UK (Tang et al., 2012). A forward model, which produces simulated profiles of attenuated backscatter from the UKV ice water

content has been developed. The ice water content is calculated in the UKV using the model variables mass fraction of cloud ice in air, temperature and pressure. Ice water content (IWC) is a critical quantity in climate studies because it is used to determine other variables such as cloud absorption, optical depth, albedo and emissivity (Heymsfield et al., 2003). Therefore, errors in model IWC are propagated through to other variables (Abel et al., 2014). This ice cloud forward model presents a novel method of evaluating the position and magnitude of IWC in the Met Office UKV. The ice cloud forward model is presented in section 5.2 to 5.4 and the potential errors and uncertainties in the forward model assumptions are quantified. In section 5.5, idealised profiles of IWC are used to test sensitivity to vertical resolution. The ice cloud forward model is first tested on radar retrieved IWC fields as validation and the results discussed in section 5.6 and then applied to model forecast data to test the realism of the model in a number of case studies. Systematic biases are identified. Finally, several comparisons are made with calibrated ceilometer data for the identified case studies. This chapter aims to establish the ice cloud forward model and discuss its potential as a tool for assessing the IWC in the UKV. The ultimate goal for this ice cloud forward model would be to run it on the forecast data and compare to a large network of calibrated ceilometers to improve the forecasting of ice cloud and therefore the weather associated with ice cloud such as fronts, rainbands, snow, and deep convective clouds.

5.2 Forward model for attenuated backscatter from ice cloud

A forward model for calculating the attenuated backscatter from ice clouds has been devised. Profiles of IWC are input into the forward model, which then calculates an extinction profile. Using estimates of the lidar ratio (S) and multiple scattering factor (η), the attenuated backscatter can be predicted at each level of the model for a given location and compared with ceilometer attenuated backscatter data.

The first step in creating the ice cloud forward model is using the IWC from the UKV to predict the extinction in that grid box. The extinction coefficient in infrared wavelengths (σ), valid for $D >> \lambda$, where D is the equivolume diameter representing particle size and λ is the lidar wavelength, is a function of particle size and particle area, given by (e.g. Heymsfield et al., 2003)

$$\sigma = 2 \int_{D_{min}}^{D_{max}} N(D)A(D)\, dD \qquad \textit{Eq. (5.1)}$$

where N is the number concentration and *A* is the area of the particles with size *D*. The IWC is given by

$$IWC = \int_{D_{min}}^{D_{max}} m(D)N(D)dD \qquad \textit{Eq. (5.2)}$$

where *m* is the mass. The forward model is constructed to match the Met Office Unified Model (and therefore the UKV) microphysics scheme. Area and mass are parameterised by the Met Office Unified Model (UM) microphysics scheme (Wilkinson et al., 2017) using:

$$A = r_x D^{s_x}, where\ r_x = 0.131\ and\ S_x = 1.88 \qquad \textit{Eq. (5.3)}$$

$$M = a_x D^{b_x}, where\ a_x = 0.0444\ and\ b_x = 2.1 \qquad \textit{Eq. (5.4)}$$

The UKV is a single moment scheme and predicts only IWC. In principle, the forward model could be constructed to match the UM microphysics scheme's assumptions about N(D), to relate IWC (2.1^{th} moment of the size distribution, b_x) to sigma (1.88^{th} moment of the size distribution, S_x). For convenience, however, and to avoid the need to integrate over the particle size spectra, we assume $S_x \approx b_x \approx 2$; in other words, both the area and the mass are essentially proportional to the same moment of the particle size distribution. Figure 5.1 depicts this.

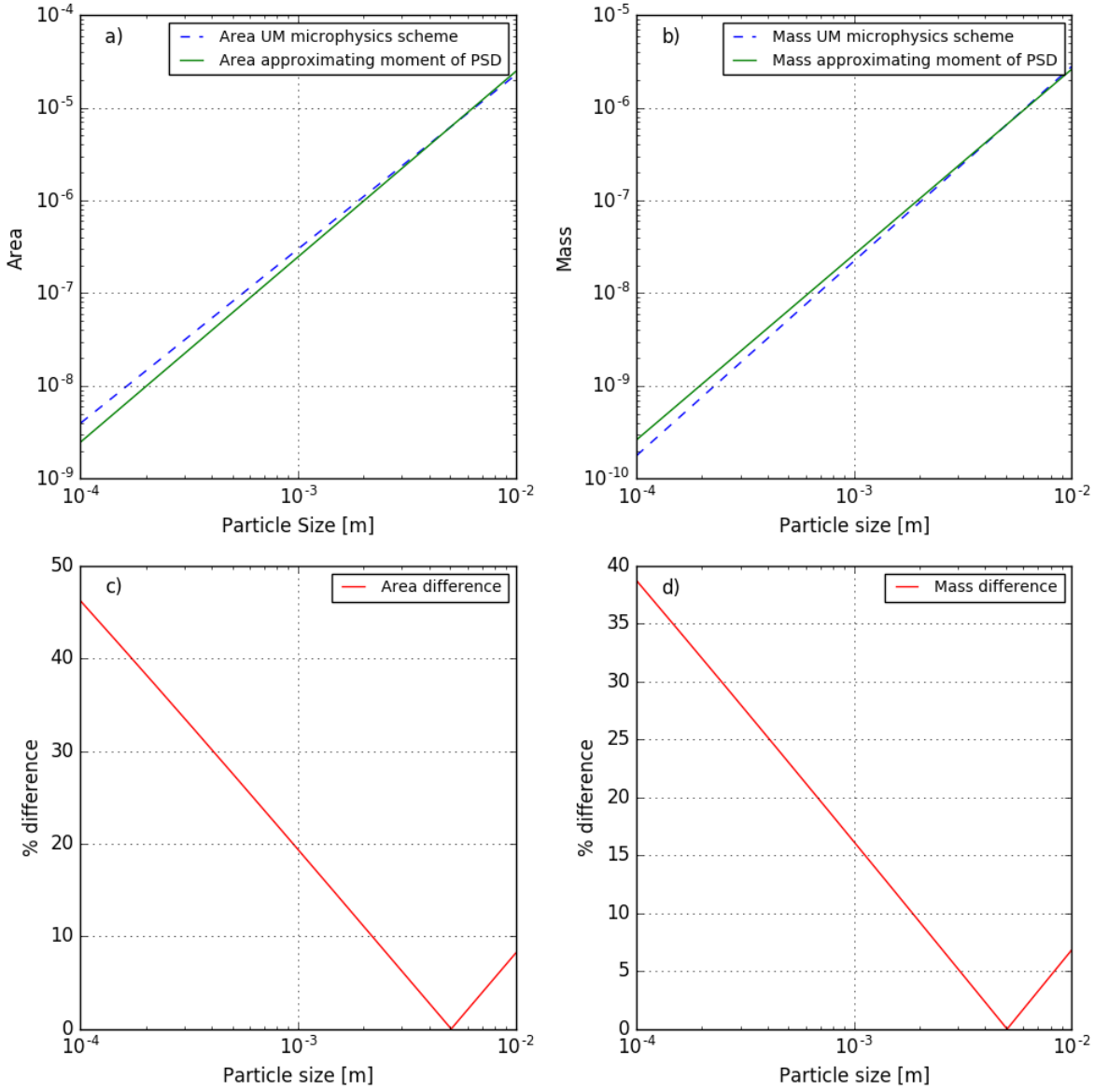

Figure 5.1: Effect of assuming a second moment relationship of particle size distribution for area and mass. a) compares the area from the UM microphysics scheme (blue x) to the area calculated using a second moment approximation (green line), b) shows the comparison for mass and c) and d) show the percentage differences for area and mass respectively.

The dotted blue line in figure 5.1a shows the ice particle area as parameterized in the Met Office UM (see equation 5.3), for a range of typical ice particle sizes (Wallace and Hobbs, 2006). Ice particle sizes below 100 μm are neglected. These small particles do not dominate

the IWC or extinction of most mid-latitude clouds which are the focus of this ice cloud forward model. On the basis that their measured fall speeds were of the order of 0.5 ms^{-1}, which requires particles much larger than 100 μm, Westbrook and Illingworth (2009) showed that the backscatter (and hence the extinction) of the Doppler lidar they used for the study was dominated by particles hundreds of microns to millimetres in size. The stratiform ice clouds observed by Westbrook and Illingworth (2009) are similar to those used in this analysis. Furthermore, while it was previously believed that ice particles below 100 μm were ubiquitous, recent studies have proved that this is in fact an artefact, caused by instrument induced particle shattering (Korolev et al, 2011; Westbrook and Illingworth, 2009; Jensen et al., 2009).

The green line in figure 5.1a shows the area over the range of particle sizes, with $S_x = 2$ used instead of $S_x = 1.88$ (see equation 5.3). From this, a new value for r_x can be derived, giving the approximation of $A \approx 0.3\ D^2$. Similarly, in figure 5.1b, the dotted blue line shows the ice particle mass as parameterized in the Met Office UM (see equation 5.4) and the green line shows the mass over the range of particle sizes, with $b_x = 2$ used instead of $b_x = 2.1$. From this, a new value for a_x can be derived, giving the approximation of $M \approx 0.021\ D^2$.

Figure 5.1c and figure 5.1b show the percentage difference between the UM parameterization and the new parameterization using a second moment approximation for the area and the mass, respectively, where particle size (x axis) is plotted using a log scale. For individual particle sizes, the difference in area is always less than 50% and in mass always less than 40%. However, it is integrated (N(D) weighted) effect on IWC and sigma that matters for the forward model.

Using the approximations $A \approx 0.3\ D^2$ and $M \approx 0.021\ D^2$, the second moment of the particle size distribution parameter, D, cancel and the extinction can be given as a function of IWC, where

$$\sigma = \frac{IWC}{0.021} \times 0.6 \qquad \textit{Eq. (5.5)}$$

This relationship can be tested using the ratio, $\frac{IWC}{\sigma}$. Substituting Λ, the observed exponent for the Marshall-Palmer distribution in clouds $N(D) = N_0 \exp(-\Lambda D)$, into equations 5.1 and 5.2, IWC and extinction can be written as

$$IWC = N_0 a_x \int_0^\infty D^{b_x} exp(-\Lambda D)\, dD \qquad \textit{Eq. (5.6)}$$

and

$$\sigma = N_0 2 r_x \int_0^\infty D^{S_x} exp(-\Lambda D)\, dD \qquad \textit{Eq. (5.7)}$$

Taking the ratio of IWC to extinction, we have

$$\frac{IWC}{\sigma} = \frac{a_x}{2r_x} \frac{\Gamma(b_x+1)}{\Gamma(S_x+1)} \Lambda^{S_x - b_x} \qquad \textit{Eq. (5.8)}$$

where Γ is the gamma function. Note that the intercept parameter N_0 cancels out. Using values given by Ryan (2000), who showed that according to several studies, Λ varies between 1000 and 10000 m^{-1}, the ratio $\frac{IWC}{\sigma}$ is shown in figure 5.2a by the blue line. The green line gives $\frac{IWC}{\sigma}$ for the approximation in equation 5.5. Figure 5.2b shows the percentage difference between $\frac{IWC}{\sigma}$ for a range of Λ and for a constant $\frac{IWC}{\sigma}$ as used in the ice cloud forward model. The percentage difference remains below 25 % and the average difference is 13.5 %.

Note that the ratio $\frac{IWC}{\sigma}$ is proportional to the effective radius, R_{eff}, which is used to describe cloud radiative properties. Van Zadelhoff et al. (2004) define R_{eff} as

$$R_{eff} = \frac{3}{2} \frac{IWC}{\rho\, \sigma} \qquad \textit{Eq. (5.9)}$$

when averaging over the particle size distribution. ρ denotes the density of solid ice. Therefore, for a constant value of $\frac{IWC}{\sigma}$, given by equation 5.5, the ice cloud forward model has a constant R_{eff} of 49 μm. This is consistent with values derived from ceilometer and radar observations at the CloudNET site Cabauw, The Netherlands, made by Van Zadelhoff et al. (2004) for warm ice clouds.

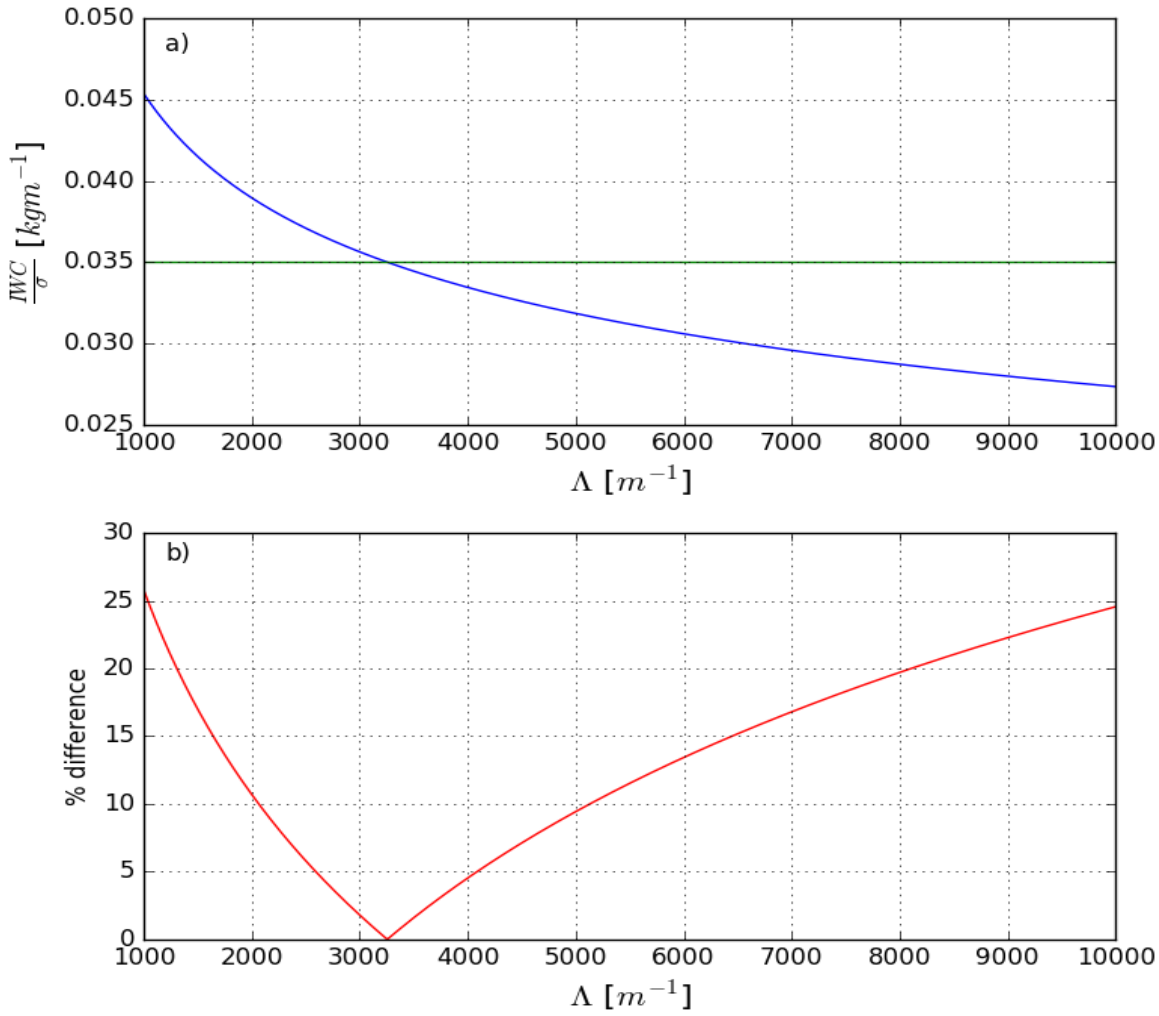

Figure 5.2: The blue line in panel a) shows calculated values of the ratio $\frac{IWC}{\sigma}$ *for ice cloud values of the observed exponent for the Marshall-Palmer distribution in clouds (Λ). The green line shows the constant ratio* $\frac{IWC}{\sigma}$ *for the derived relationship* $\sigma = \frac{IWC}{0.021} \times 0.6$*, which assumes a second order moment for the particle area and mass distributions. Panel b) shows the percentage difference of the two.*

The derived relationship between σ and IWC in equation 5.5 also gives values consistent with the relationship derived from various data sets by Heymsfield et al. (2005). Described in Heymsfield et al. (2005), the data sets combine both direct and derived values of extinction and IWC from aircraft probes, balloon-borne replicators, lidar and radar observations and a particle

growth model at various different latitudes. The data sets are combined and organised by temperature, as shown in figure 5.3.

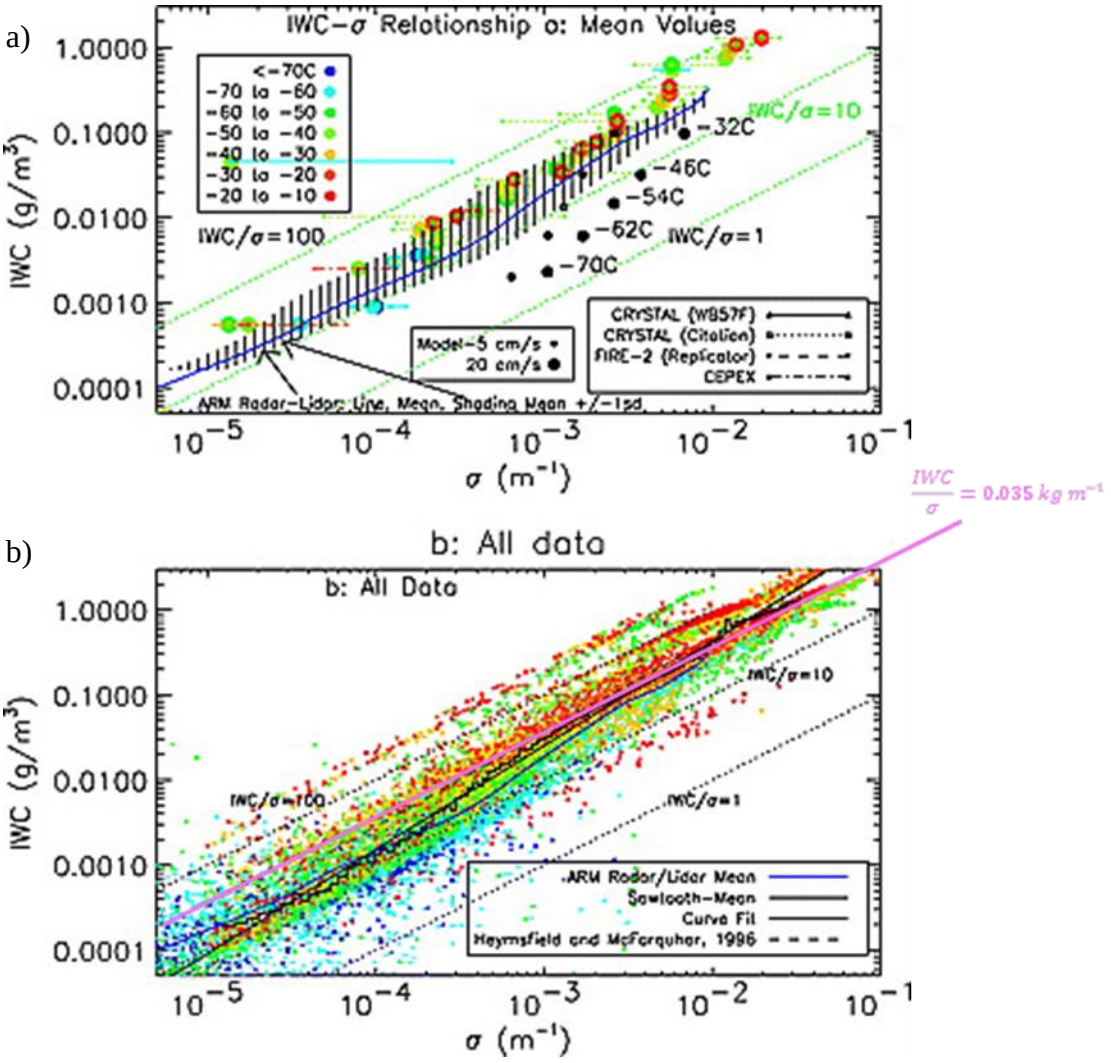

Figure 5.3: Relationship between σ and IWC derived from various data sets. (a) Mean values. (b) Individual data points, mean in given intervals, and power-law curve fitted through the mean values. Source: Heymsfield et al. (2005). The superimposed pink line shows the where the ratio $\frac{IWC}{\sigma}$ *is equal to 0.035 kg m*$^{-1}$.

Figure 5.3 is taken from Heymsfield et al. (2005), with our value of $\frac{IWC}{\sigma} = 0.035\ kg\ m^{-1}$ superimposed as the pink solid line. It shows that the constant value for the ratio $\frac{IWC}{\sigma}$ given by equation 5.5 is consistent with the values observed by Heymsfield et al.

(2005), particularly those for temperatures between -10 °C and -30 °C. As mentioned, the ice forward model has been constructed for warm ice cloud. It has therefore been demonstrated that the approximation, $\sigma = \frac{IWC}{0.021} \times 0.6$ gives reasonable values of $\frac{IWC}{\sigma}$ and R_{eff}, which are consistent with previous literature.

Using this relationship for IWC and extinction, the backscatter (β) can then be calculated using the lidar ratio (S), using: $\beta = \sigma/S$. S is determined by observations of optically thick ice cloud, from the Vaisala CL51 ceilometer at Chilbolton Observatory, England using the same method described in Chapter 3 (see section 5.4). Finally, the attenuation, through the ice and from water vapour, is accounted for to produce profiles of attenuated backscatter (β), which are comparable with ceilometer observations.

5.3 Case Studies

Table 5.1 provides a brief summary of the case studies used in this chapter. They were selected using the quicklooks from the Chilbolton Vaisala CL51 ceilometer and the 35 GHz cloud radar to ensure that each case study had a prolonged period (at least 1 hour) of thick cloud (at least 1 km thick) with a cloud base height between 3 and 7 km.

Case Study Date	Period where ice cloud is present (hrs since 00.00)	min CBH	Max CBH
11/11/2016	15.00-23.99	3 km	10 km
12/01/2017	19.00-21.00	3 km	6 km
27/01/2017	17.00-21.00	3 km	4 km
01/03/2017	05.00-10.00	3km	8 km
02/03/2017	12.00-23.99	6 km	7 km
03/03/2017	00.00-03.00	3 km	8 km
04/03/2017	00.00-09.00	4 km	6 km
06/03/2017	05.00-15.00	3 km	6 km
31/10/2017	14.00-23.99	3 km	7 km

Table 5.1:List of case studies used for the development and testing of the ice cloud attenuated backscatter forward model.

5.4 Multiple Scattering

The lidar ratio for ice cloud can be calculated using the same method used to calculate the apparent S of liquid water cloud described in chapter 3, as long as the ice cloud is sufficiently thick that the ceilometer beam is completely extinguished and there are no supercooled layers present (O'Connor et al., 2004). As was done for the calibration, a multiple scattering correction must first be applied. The multiple scattering correction is calculated (Hogan, 2006) to account for the multiple scattering of the backscatter by the ice particles. Without the inclusion of multiple scattering, this would result in a large uncertainty in the forward model and be the cause of a significant systematic bias when comparing the attenuated backscatter from the ceilometer to that calculated by the forward model. This multiple scattering impact is therefore included in the forward model to match the multiple scattering which affects the ceilometer observations. To run the multiple scattering model, the following Vaisala CL51 ceilometer parameters are used; the FOV is 0.56 mrad and the beam divergence is 0.15 x 0.25 mrad. An asymmetry factor (g) for ice cloud of 0.75 was used (Garrett et al., 2001; Fu, 2007) and a realistic range of ice particle sizes tested (Heymsfield et al., 2013). Note that this is not particle size, D, but rather the effective cross-sectional area. It is this size which determines the width of the forward scattering lobe and is a critical parameter in determining how much of the forward scattering stays within the lidar FOV. Different lidar ratios over a range wider than expected for ice cloud are tested and the results are shown in figure 5.4.

Figure 5.4 shows that, for realistic ice particle sizes and for a large range of lidar ratios (10 – 70 sr, larger than the expected range of S for ice clouds), the results are close to the limit where all of the scattered photons stay within the field of view of the telescope, and therefore can be represented simply using the range independent multiple scattering parameter η=0.5. This is consistent with Rogers et al. (1997), who estimate η=0.5 for ceilometer wavelengths, as the field of view is wide relative to the forward scattering phase functions. Figure 5.4 does show

that for very small particle sizes, η is larger and more variable. However, as the focus of the ice forward model is thick, warmer ice clouds where particle sizes are generally larger, a constant of 0.5 for the multiple scattering is applied in the ice cloud forward model.

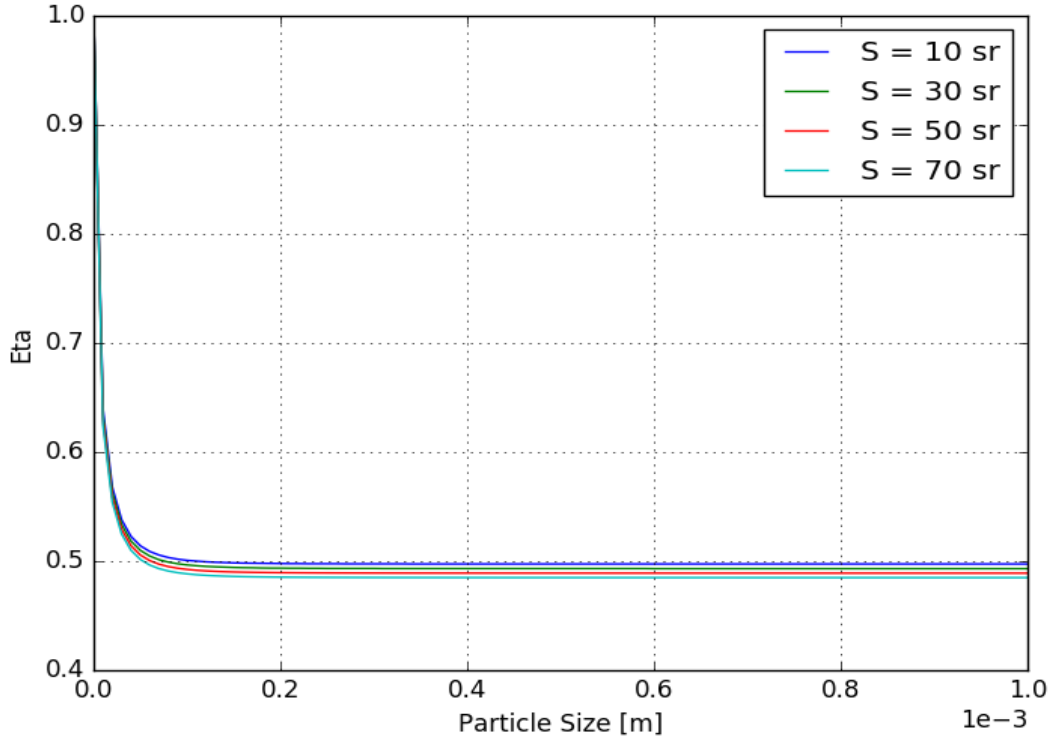

Figure 5.4: Multiple scattering coefficients for a ceilometer with wavelength 910 nm, for a range of sizes typical of ice particles and for a large range of lidar ranges.

5.5 Determining the ice cloud lidar ratio

To calculate the lidar ratio (S) for ice, the Vaisala CL51 ceilometer at the Chilbolton Observatory, Hampshire, is used. The Cl31 ceilometers have a range limitation of ~8 km and therefore either do not see the higher ice cloud or have a low signal-to-noise ratio for these clouds. Moreover, the 2.4 km change in data processing means the raw data is unattainable and so until the Met Office is able to install the newer firmware, the Met Office CL31s are unsuitable. The Lufft ceilometers have a more suitable range, as they can observe up to 15 km.

However, as discussed in Chapter 2, the Lufft ceilometers in the Met Office network have required several hardware and software updates. A further issue with all the Met Office ceilometers is the tilt. Specular reflection from oriented pristine plate crystals can produce a very large backscatter (Westbrook et al., 2010a) which is not representative of the broader population and which is not being forward modelled. Hence, we need to ensure the instruments are pointed away from zenith. The Met Office ceilometer network all have a maximum tilt of 2°, some are not tilted at all. The Chilbolton CL51, however, is operated in research mode, and pointed 4° off zenith so it is a sensible choice for the initial development of the forward model methodology. It also has the advantage of being collocated with other instruments such as radar, which can be use for comparison.

For ice clouds that fully extinguish the ceilometer beam, S is calculated using $B = \frac{1}{2\eta S}$ (see chapter 3, equation 3.1). Any profiles that are affected by a reduced window transmission or pulse energy are removed and a water vapour correction to account for attenuation below the cloud is applied. As detailed in chapter 3, the water vapour attenuation is calculated using UKV data for the grid box over Chilbolton. Figure 5.5 shows an example of the calculated lidar ratio for thick ice cloud. The attenuation of the ceilometer signal can be checked using the 35 GHz cloud radar that is also present on the Chilbolton field site (see figure 5.12a for plot of radar reflectivity factor); as the radar shows a much thicker cloud than the ceilometer, we know that the ceilometer signal is being fully attenuated by the cloud. At around 19.00 hrs and 20.00 hrs the ice cloud is slightly thinner and may not be quite fully attenuating the ceilometer signal, so these profiles are filtered out. Figure 5.5b shows the calculated lidar ratio corresponding to each 30 second ceilometer profile of attenuated backscatter. The mean S for this period is 40.2 sr, with a variability of 6.8 sr, or 17 %. While this is larger than the variability in liquid water clouds (see chapter 4), this is to be expected as ice particles are a lot more variable in size and shape than liquid water particles.

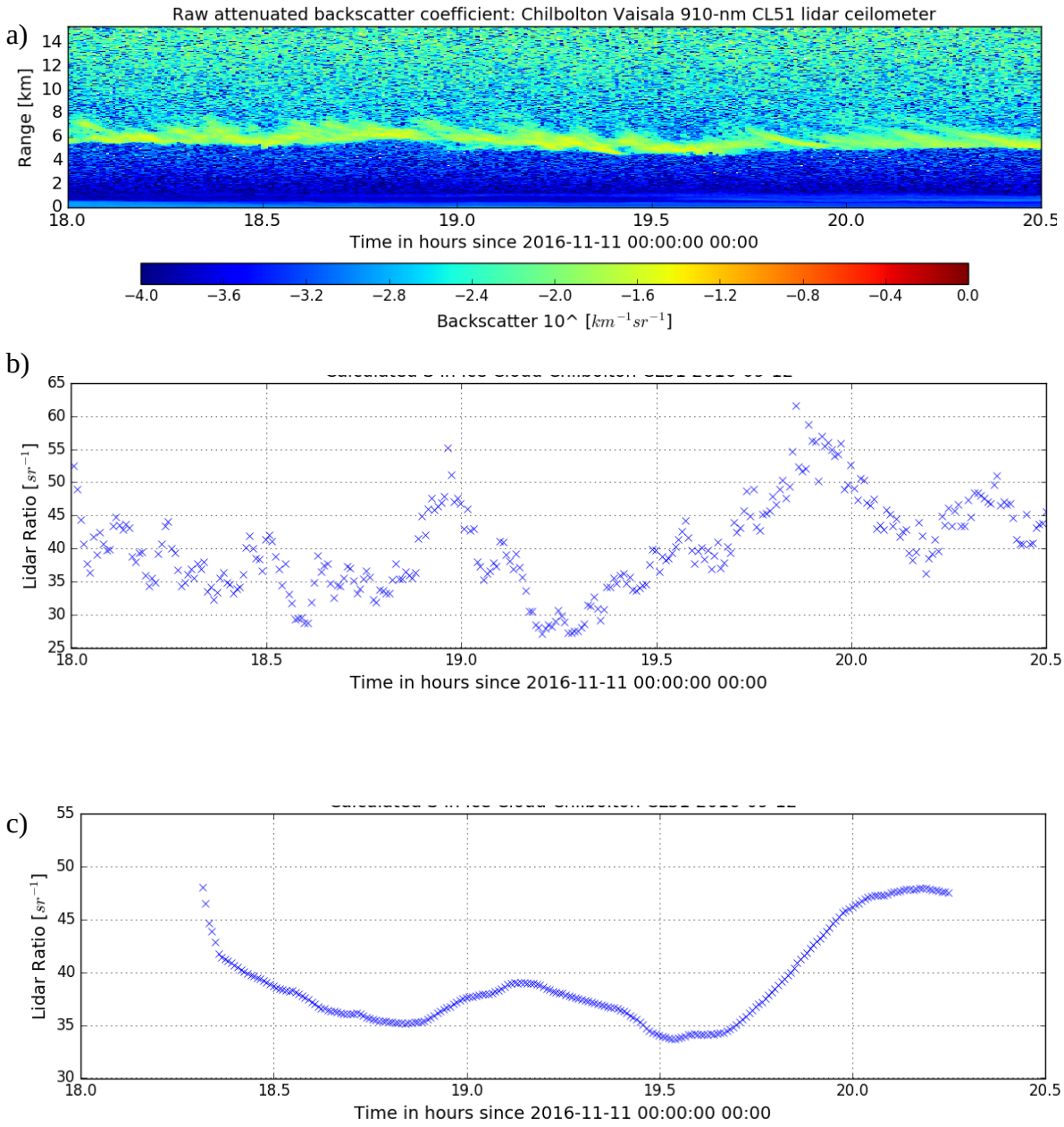

Figure 5.5: a) Attenuated backscatter observed by the Chilbolton Vaisala CL51 ceilometer from 18.0-20.5 hrs, b) the corresponding calculated lidar ratio where each blue cross is for a 30 second profile and c) the 30 minute running average lidar ratio for 18.5-20.5 hrs.

For the comparison between the observed attenuated backscatter and the forward modelled backscatter, the observation is averaged to remove the finer scale microphysical details that are not resolved in the UKV model (see section 5.9). We therefore apply a 30 minute running average to the S associated with each individual profile, as shown in figure 5.5c. This smooths

out the variability to 12 %, although there is still a range of values between 34 and 48 sr. The mean for the 30 minute averaged data is 39.7 ± 4.8 sr.

Figure 5.6 shows histograms of the lidar ratio calculated from profiles of attenuated backscatter where there was ice cloud that was optically thick enough to fully attenuate the ceilometer beam. These periods of ice cloud occurred over 9 days in 2016-2017. Of the total 25,920 individual profiles of attenuated backscatter observed during this period, 530 profiles were used to calculate the ice cloud lidar ratio. The 530 profiles of attenuated backscatter were selected from the middle of sustained (more than 1 hour) periods of thick ice cloud between 3 and 7 km. The full attenuation of the ceilometer beam was confirmed using the radar plots of reflectivity.

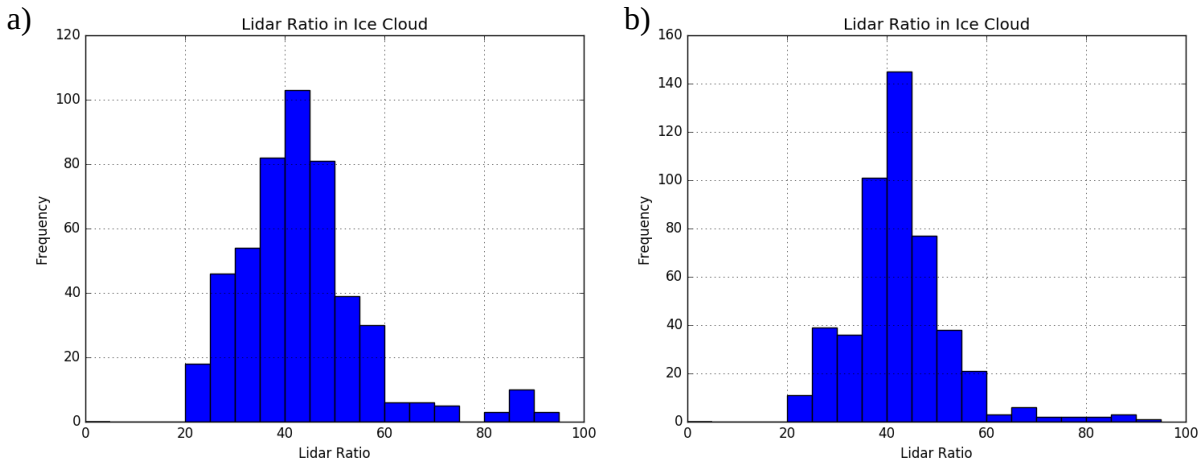

Figure 5.6: Histograms of ice cloud lidar ratio calculated from periods of thick, attenuating ice cloud during 9 case studies. The ceilometer data have been calibrated and water vapour below cloud has been accounted for before the lidar ratio was calculated. In panel a) the lidar ratio is calculated from each 30 second ceilometer attenuated backscatter profile of fully attenuating ice cloud. In panel b) a 30 minute running mean of the lidar ratios has been calculated.

Figure 5.6a shows the histogram for the lidar ratios calculated from individual 30 s profiles of attenuated backscatter. The mean is 43.5 sr, with a standard deviation of 13.2 sr; this is 30 %

of the mean. Figure 5.6b shows the histogram of the lidar ratios after a 30 minute running average was applied. This time, the mean is 42.8 sr, with a standard deviation of 10.9 sr; 25% of the mean.

These values of S appear larger than some other studies in the literature; for example, Yorks et al. (2011) report ice cloud lidar ratios for several airbourne projects, with the majority (84 %) ranging from 10.0 to 40.0 sr and in agreement with Eloranta et al. (2001) and Reichardt et al. (2002). However, the majority of ice cloud lidar ratios in these works are focussed on observations of cirrus cloud. This study, on the other hand, focusses on thick, warmer ice clouds which tend to have larger, more aggregated particles (Lohmann et al., 2016) compared to thin, cold cirrus cloud. We therefore cannot expect the lidar ratio to be the same. O'Connor et al. (2004), who first derived the theory used here, tested a couple of ice cloud cases and found values of ηS between 5 and 30 sr. For η=0.5, this would give an S between 10 and 60 sr, which agrees with figure 5.6. Based on these findings, a value of 40 sr is used for the forward model.

5.6 Idealised profiles

To test the model set up and sensitivity, idealised profiles of IWC were used. Figure 5.7 shows an example of the idealised tests, where figure 5.7a is for IWC values between 10^{-6} and $0.5x10^{-4}$ kg m^{-3} and figure 5.7b is for IWC values between 10^{-4} and 10^{-3} kg m^{-3}. The top panel shows the profiles of IWC. For each profile, the IWC is zero up to 5 km. At 5 km the IWC is increased to a set value and held constant for the rest of the profile. As the Vaisala CL51 ceilometer has a range of 15 km, this is the maximum height used for the profiles. The values of IWC range from 10^{-6} to 10^{-3} kg m^{-3}, and therefore should encompass realistic atmospheric values of IWC (e.g. Brown, 1993). The second panel shows the extinction for each of the profiles of IWC, calculated using the approximation in equation 5.5. The third panel shows the transmission as a result of the attenuation caused by extinction and multiple scattering, given by

$$T_{att} = exp(-2\eta\tau(r)) \qquad \textit{Eq. (5.10)}$$

where T_{att} is the transmission due to attenuation and τ is the optical depth , calculated by integrating the extinction. The final panel shows the attenuated backscatter, where the true backscatter is calculated from the extinction using an assumed lidar ratio of 40 sr and then attenuated using the attenuation profile. The height resolution of this example is 10 m.

For a profile of IWC that would be strong enough to fully attenuate a ceilometer beam and assuming a lidar ratio of 40 sr, the integrated attenuated backscatter (B) will equal 0.025 sr^{-1}. The value of B for each of the idealised profiles in figure 5.7 is shown in the legend of the bottom panel. The second, third and fourth panels of figure 5.7 show up to 8 km, not 15km, for clarity; this is sufficient to show the behaviour at each stage. For example, the cyan line in the top panel of figure 5.7a shows a profile with an IWC of $0.5x10^{-5}$ kg m^{-3} (i.e. a mid-range value of IWC). The next panel shows the extinction for this profile, again shown by the cyan line, and has a value of 0.0012 m^{-1}. The corresponding transmission for the cyan profile in the next panel down shows that by 8km, the tranmission coefficient has dropped to almost zero. Once the attenuation reaches zero, the extinction has caused full attenuation. The final panel shows the impact of this attenuation on the backscatter. Initially, the attenuated backscatter of the cyan profile has a value of 0.029 km^{-1} sr^{-1}, but this drops rapidly due to the attenuation, reaching zero just above 8 km. Therefore, even though the IWC profile goes to 15 km, the attenuated backscatter profile is fully attenuated before reaching this range. The value of B for the cyan profile is 0.0247 sr^{-1}; the expected value for a fully attenuating backscatter profile.

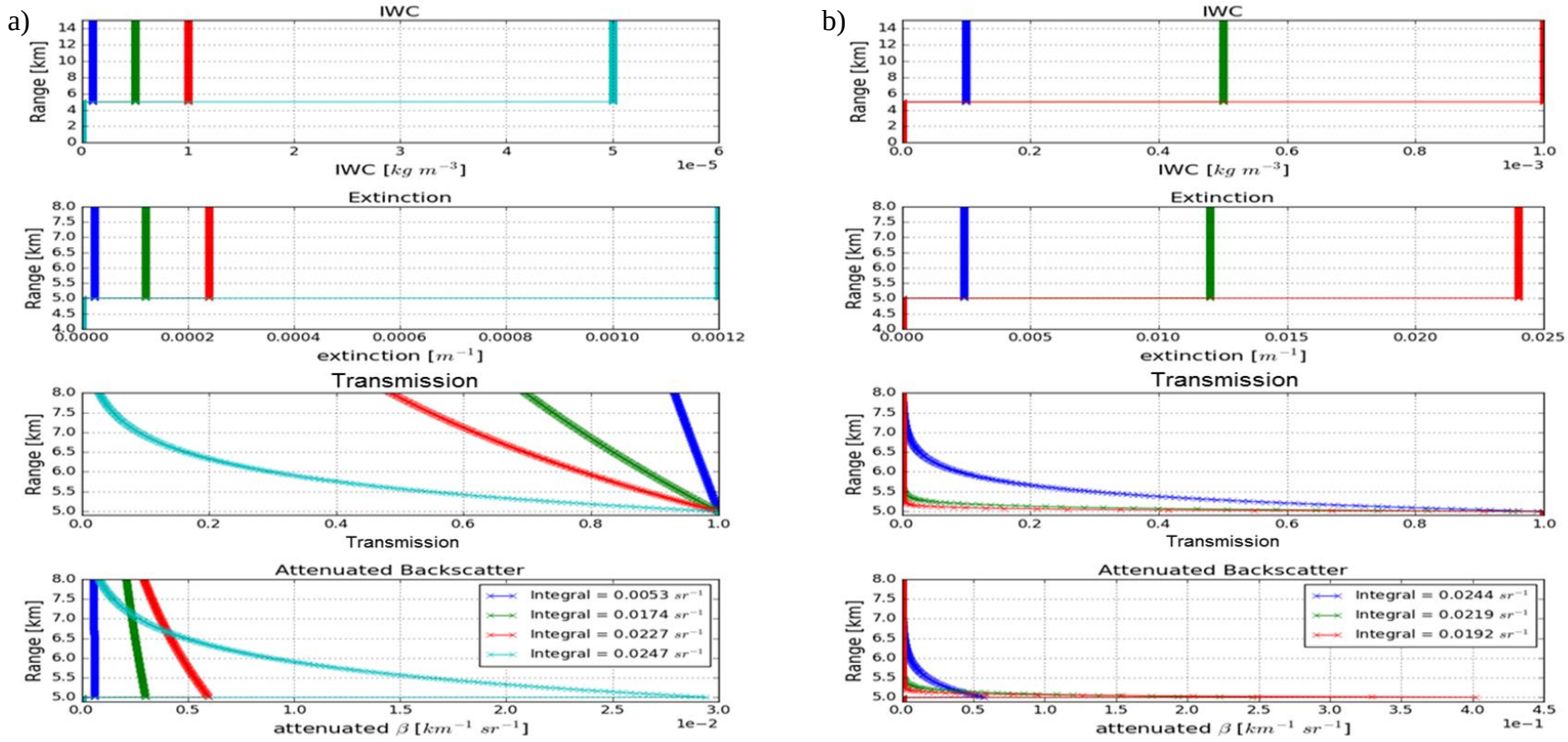

Figure 5.7: Idealised profiles to show steps of ice cloud forward model. a) shows the profiles for IWC from 1e-6 to 0.5e-4 kg m^{-3} and b) shows the profiles for IWC from 10^{-4} to 10^{-3} kg m^{-3}. The top panels shows the idealised profiles of IWC, the second panels show the resultant extinction for the IWC, the third panels show the transmission corresponding to the extinction and the bottom panels show the attenuated backscatter. The IWC profiles have a maximum height of 15 km. The extinction, transmission and attenuated backscatter also have a maximum height of 15 km but only the first 8 km are shown so that the profile shapes are distinguishable.

Figure 5.7b shows that for larger IWC (e.g. 10^{-3} kg m^{-3}, the red profile), attenuation is very rapid. The value of B is 0.0192 sr^{-1}, which is well below the expected value of 0.025 sr^{-1}. This is because the attenuation is so rapid, it cannot be fully resolved and therefore the attenuated backscatter is lower than it should be, as shown in figure 5.8. An idealised profile IWC has a value of 10^{-4} kg m^{-3} from 5 – 15 km (identical to the blue profile in the top panel of figure 5.7b). The range resolution of this profile is tested with resolutions of 1m, 10 m, 50 m, 100 m and 250 m. The attenuation and attenuated backscatter have been calculated for each different resolution and plotted. As shown in figure 5.8, as the resolution is reduced, the attenuation becomes less resolved and hence the attenuated backscatter is too low. This is shown indicated by the values a B in figure 5.8b, which should equal 0.025 sr^{-1}.

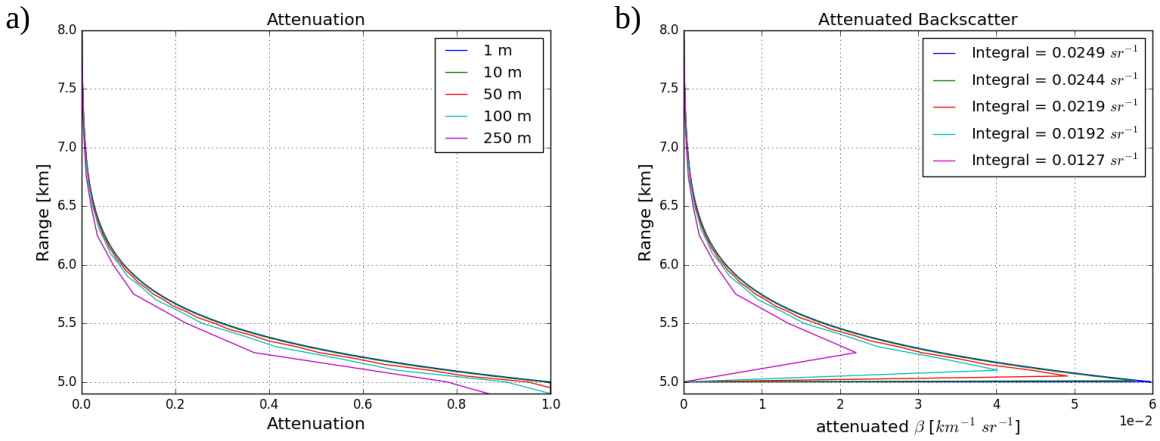

Figure 5.8: For an idealised profile of constant IWC value of 10^{-4} kg m^{-3} from 5 – 15 km, panel a) shows the attenuation with the different coloured profiles for different resolutions set for the IWC profile. Panel b) shows the corresponding attenuated backscatter and the values of B are shown in the legend.

Attenuation is a continuous process, however in order to model it, we have to discretise to grid-squares. Where attenuation is rapid and thus the change between neighbouring grid-points is highly non-linear, the process is not properly resolved and there is a discretisation error. With the 10 m resolution used in figure 5.7, the attenuation is adequately resolved for IWC values

of 10^{-4} and $0.5x10^{-4}$ kg m^{-3}, indicated by a value of B around 0.025 sr^{-1}. For values of IWC below this, the value of B drops again. However, this is simply because the attenuation does not reach zero over the modelled cloud depth so the IWC does not cause full attenuation and therefore the rule of $B = \frac{1}{2\eta S}$ is not valid in these cases, because the cloud is not optically thick.

To further test for which resolution the ice cloud forward model will require to fully resolve the attenuation, the IWC was held constant and the integrated attenuated backscatter was calculated for a range of height resolutions, from 0.0001 to 0.5 km. The results are shown in figure 5.9. As discussed, for a profile of IWC, where the extinction would cause complete attenuation and assuming a lidar ratio of 40 sr and a multiple scattering coefficient of 0.5, the value of B for the corresponding attenuated backscatter profile should equal 0.025 sr^{-1}. This value is shown in figure 5.9 by the red dotted line. Each panel corresponds to a different value of IWC. Figure 5.9d shows an example of smaller IWC, which does not cause complete attenuation within the maximum range of 15 m that are considered (to correspond to the maximum range observable with the CL51 ceilometer). Therefore the value of B does not reach the value of 0.025 sr^{-1}.

It is evident from figure 5.9a, b and c that for an attenuating cloud, the higher the value of IWC, the higher the resolution that is needed to resolve the attenuated backscatter. For large values of IWC, figure 5.9a indicates that to completely resolve the attenuated backscatter, a model resolution of the order of 1 m would be necessary. However, this would be more computationally expensive. Therefore, a resolution of 10 m has been chosen for the ice cloud forward model.

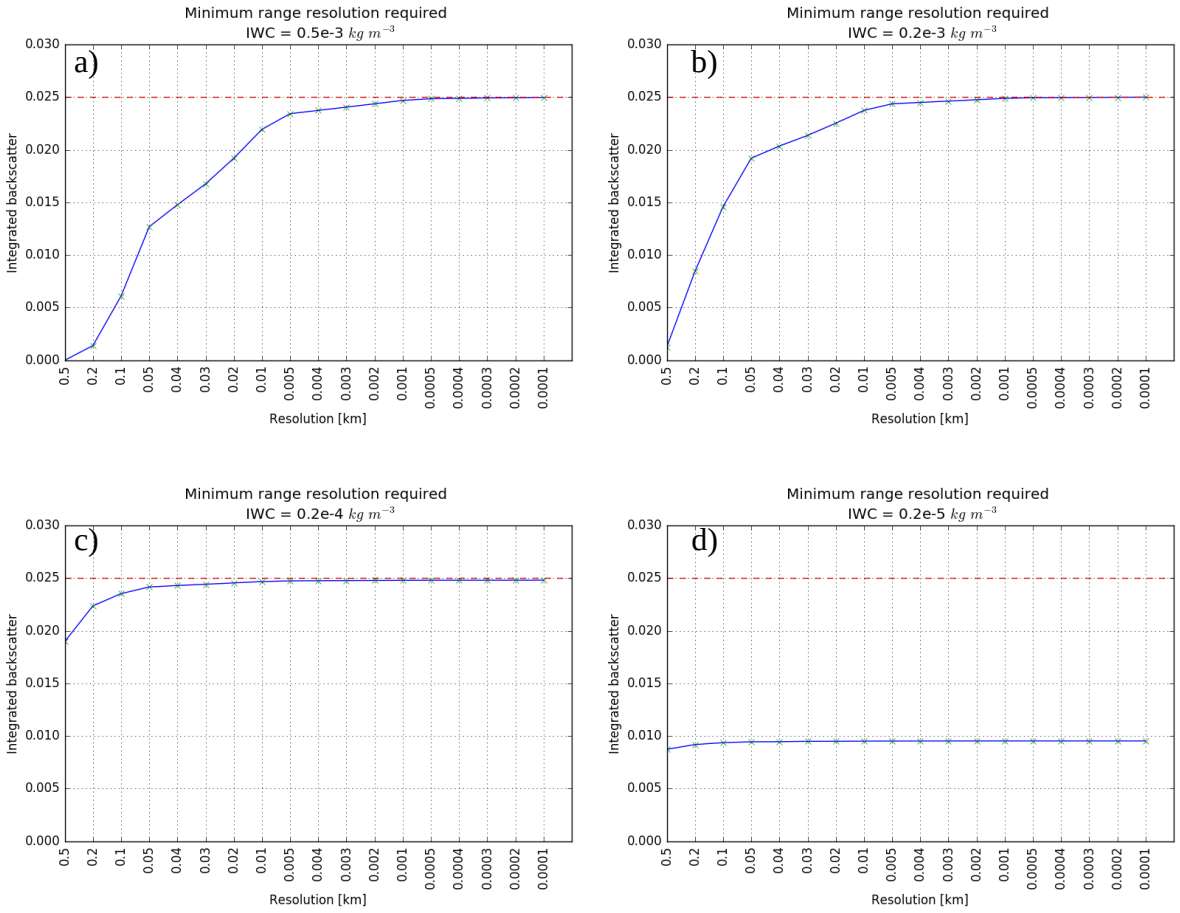

Figure 5.9: Range resolution required to fully resolve the attenuation due to IWC. The red dotted line is for B = 0.025 and hence indicates where the attenuation can be resolved. Each panel show a different value of IWC: a) IWC = 0.5x10^{-3} kg m^{-3}, b) IWC = 0.2x10^{-3} kg m^{-3}, c) IWC = 0.2x10^{-4} kg m^{-3} and d) IWC = 0.2x10^{-5} kg m^{-3}.

While this means that the attenuated backscatter for very large IWC would be too small, it is more computationally reasonable and the error would be at most 14%. Furthermore, this is for idealised profiles of IWC, where the IWC is held constant. In reality, there are unlikely to be cases of such large IWC sustained for such a large depth of cloud. Therefore, the error is likely much smaller. A resolution of 10 m also has the advantage of matching the ceilometer range resolution, making a comparison between the forward model and the ceilometer more straightforward.

In summary, we interpolate the model IWC profiles to the ceilometer range grid and compute attenuated backscatter profiles on that grid. This is much more accurate than forward modelling the backscatter on the model grid which has a coarse vertical resolution.

It is worth noting, however, that this approach may prove too slow for large volumes of data. In this case, if one assumes that the extinction and backscatter within a (coarse) grid cell are constant then algebraic forms for the coarse resolution lidar backscatter can be formulated.

5.7 Forward modelling radar derived IWC

To independently test the validity of the assumptions made for the ice cloud forward model, it has been run on data independent to both the UKV and the ceilometer. As the CL51 ceilometer used for comparisons is situated at The Chilbolton Observatory, there are many collocated instruments. One such instrument is a 35 GHz cloud radar. As the ceilometer and the radar are collocated, they should observe the same clouds. By converting the radar reflectivity (Z) into attenuated backscatter, the profiles of both instruments can be compared. If the attenuated backscatter derived from the radar is a similar in magnitude and height, it can be assumed that the forward model is correctly converting IWC into attenuated backscatter and that therefore differences between the UKV derived attenuated backscatter and the ceilometer attenuated backscatter are a result of UKV errors.

In order to carry out this test, the radar reflectivity must be converted into IWC. Hogan et al. (2006) derived empirical formulae using in situ aircraft measurements of size spectra. The empirical relationship for deriving IWC from a 35 GHz radar is given by

$$log10(IWC) = (0.000242)ZT + (0.0699)Z - (0.0186)T - 1.63 \qquad \text{Eq. (5.11)}$$

where IWC is the ice water content and is given in g m^{-3}, Z is the radar reflectivity factor in dBZ and T is the temperature in °C. Between -20° and -10°C, the RMS error in retrieved IWC is around 50%/-33%, but for T < -40°C it rises to 100%/-50% (Hogan et al., 2006; Stein et al.,

2011). Retrievals of the radar IWC have already been created as part of the Cloudnet project (Illingworth et al., 2007).

Figure 5.10 shows an example of the ice cloud forward model, using the radar reflectivity factor derived IWC and the resulting attenuated backscatter.

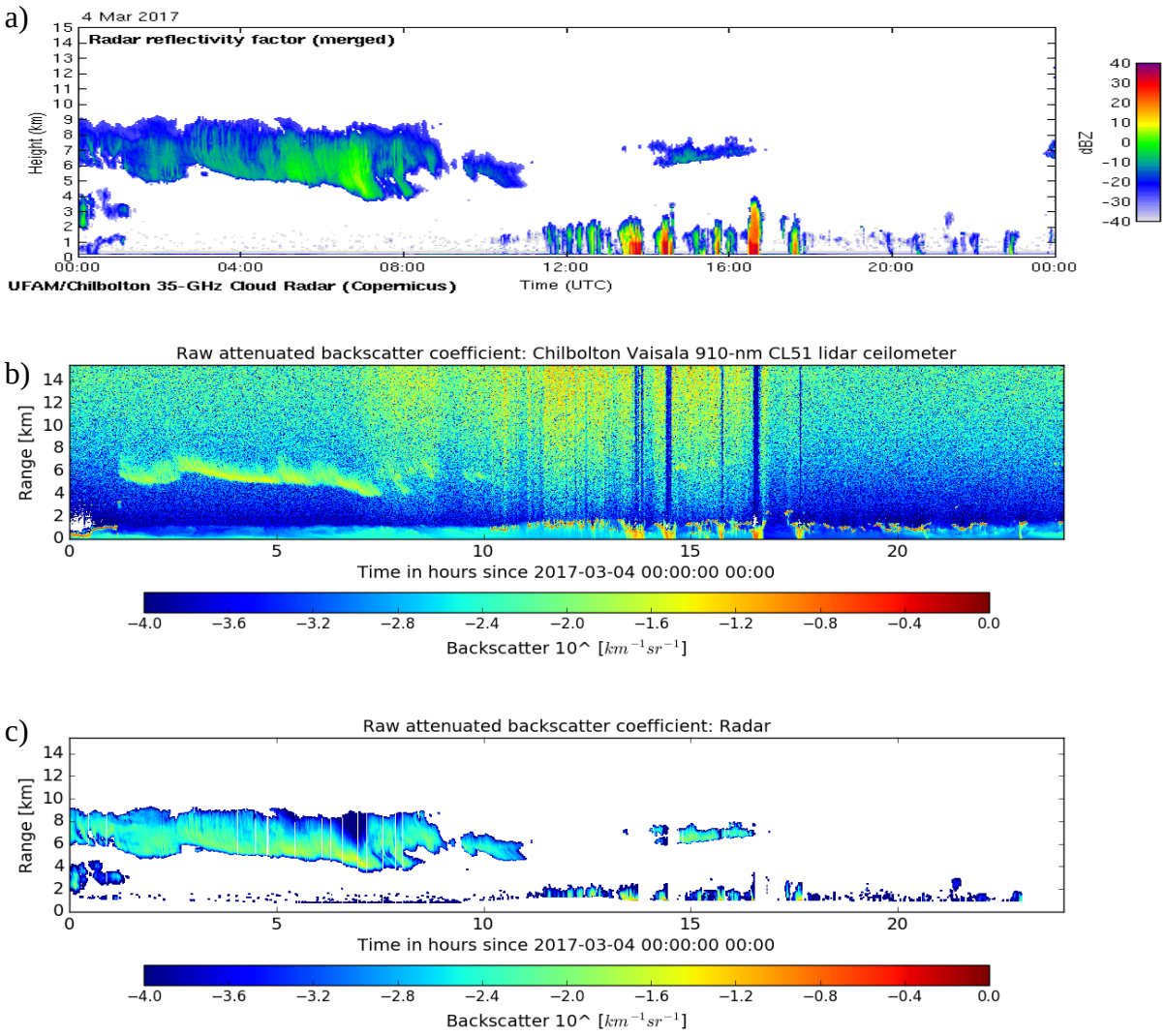

Figure 5.10: a) Reflectivity factor from the Chilbolton 35 GHz cloud radar, plot source: http://www.met.rdg.ac.uk/radar/cgi-bin/cloudarchive.cgi?date=20170304, b) attenuated backscatter observed by the Chilbolton CL51 and c) attenuated backscatter calculated from the IWC which was derived from the Chilbolton 35 GHz cloud radar reflectivity factor.

Figure 5.10a shows the reflectivity factor observed by the cloud radar and Figure 5.10b shows the attenuated backscatter observed by the Vaisala CL51 ceilometer. They both show a

sustained period of ice cloud from approximately 1.00-7.00 hrs with a cloud base height fluctuating around 5 km. The radar reflectivity shows this cloud from 0.00 hrs, however due to the lower liquid water cloud at around 1km also present for the first hour of the day, the ceilometer beam is fully attenuated at this earlier time and so does not observe the higher cloud. The radar reflectivity factor also shows that the cloud is much thicker than what the ceilometer observes. The radar shows a cloud top of approximately 10 km, whereas the ceilometer shows no signal, only noise, above 7km. This shows that this is a thick ice cloud which fully attenuates the ceilometer beam.

Figure 5.10c shows the attenuated backscatter calculated by the ice cloud forward model from the radar derived IWC. The attenuated backscatter calculated from the radar IWC and observed by the ceilometer show many similarities. The general structure and shape of the backscatter are comparable, as is the magnitude. The radar derived backscatter at 6 km is still visible between 0.00-1.00 hrs, unlike the ceilometer backscatter; however, this is to be expected as the ice forward model does not model attenuation due to liquid water cloud.

Figure 5.11a shows an example of attenuated backscatter profiles from 12th November 2016. The blue is the Vaisala CL51 observed attenuated backscatter and the red is the forward modelled attenuated backscatter from the radar derived IWC. The profiles are a 10 minute average, to smooth out the differences due to the CL51 and the radar having different time and range resolutions. The two profiles are very similar in height, magnitude and shape, indicating that despite the potentially large RMS error from deriving the IWC from the radar reflectivity factor, the forward model is capable of correctly modelling attenuated backscatter from IWC.

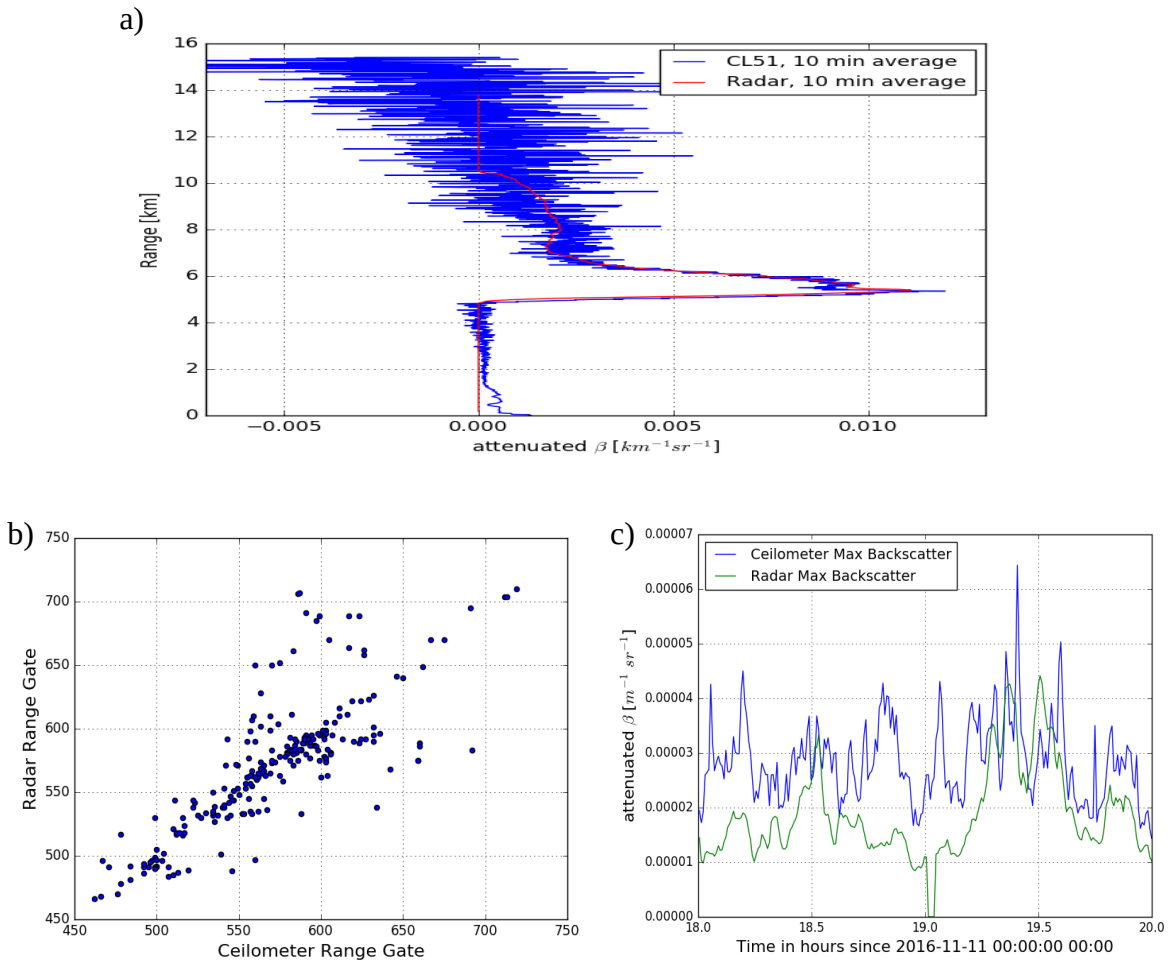

Figure 5.11: a) 10 minute average profiles of attenuated backscatter from Chilbolton Observatory on 11th November 2016, 19:55-20:05. The blue line is the Vaisala CL51 observed attenuated backscatter. The data has been calibrated but not corrected for attenuation due to water vapour or for multiple scattering. The red line is for the attenuated backscatter forward modelled from the 35 GHz radar derived IWC, where attenuation due to water vapour and multiple scattering have been modelled. b) Scatter plot of the range gate number of the maximum attenuated backscatter in each profile between 18.00 and 20.00 on 11th November 2016 as observed by the Vaisala CL51 ceilometer (x axis) and calculated from the radar reflectivity at Chilbolton. c) shows the value of the maximum backscatter for these instruments.

Figure 5.11b shows a comparison of the height of the maximum backscatter for the CL5 and the radar derived backscatter over a two hour period. The majority of the scatter are on a 1:1

line showing that the radar derived attenuated backscatter is at the same height as that observed by the ceilometer. Figure 5.11c shows the value of the maximum backscatter for the same two hour period. There is more variability in this plot; there are periods (such as around 18.75 hrs) where the attenuated backscatter is quite different. This is to be expected, considering the large RMS error from deriving the IWC from the radar reflectivity factor. There are also periods (such as around 19.5 hrs) where the value of the maximum attenuated backscatter derived from the radar is very similar to that observed by the ceilometer.

5.8 Forward modelled backscatter from UKV forecasts

5.8.1 11th November 2016

After such promising results from running the ice cloud forward model on the radar derived IWC, the forward model was then run using IWC from UKV data. The aim is to compare the attenuated backscatter derived by the forward model to the attenuated backscatter observed by the ceilometers. Hence, this rest of this chapter begins the process of assessing the viability and potential for using ceilometer data to improve short term forecasts through the assimilation of attenuated backscatter. A number of case studies have been selected. Figure 5.12 shows an example case study, where the ice cloud forward model has been used to model attenuated backscatter for IWC derived from both the Chilbolton 35 GHz radar and from the UKV. Figure 5.12a shows the radar reflectivity factor and shows there was a sustained period of deep ice cloud, from approximately 13:00 hrs which persisted through to the end of the day. Figure 5.12b shows this same cloud as observed by the Vaisala CL51 ceilometer. Figure 5.12c also shows the attenuated backscatter from the Vaisala CL51, but with the instrument noise removed from the plot, so that the extent of the cloud is clearer. The ceilometer does not observe the cloud until 15.00 hrs and the depth of the cloud observed compared to the radar is shallower, confirming that this ice cloud fully attenuates the ceilometer signal. There is a

period of strong (> 10^{-1} km^{-1} sr^{-1}) attenuated backscatter at approximately 5 km from 21.00 hrs which is a layer of super-cooled water and therefore not included in the ice cloud forward model. Note that the higher the ice cloud, the lower the temperature is expected to be. The fixed value of R_{eff} assumes warm ice cloud (as shown in Figure 5.3) so as the temperature decreases, the validity of the ice forward model may decrease. Figure 5.12d shows the forward modelled attenuated backscatter for the radar derived IWC. As in Figure 5.10, the radar forward modelled attenuated backscatter is very similar to the ceilometer observed attenuated backscatter: the cloud base height shows the same increases and falls (e.g. there is a sharp drop in cloud base at 21.10 hrs) and there are similar increases and decreases in the peak attenuated backscatter (e.g. the peak backscatter increases to approximately 5.0 x10^{-5} km^{-1} sr^{-1} at 19.57 hrs, 21.10 hrs and from 23.00 hrs). Figure 5.12e shows the forward modelled attenuated backscatter from the UKV derived IWC. As the UKV is on a much coarser range resolution and only saves the forecast once per hour, it is not expected that the forward modelled attenuated backscatter would match the shape of the 30 s attenuated backscatter profiles observed by the Vaisala CL51.

Despite this coarse resolution, it is possible to see some similarities to the observed attenuated backscatter; there is a layer of attenuated backscatter in Figure 5.12e which starts at about 10 km and drops down to a cloud base height of 3 km over the course of 8 hours, just as the ceilometer has observed. However, the magnitude of the attenuated backscatter is lower for the forward model compared to that of the ceilometer. Figure 5.12, therefore, suggests that although the forward model may not have the correct quantitative detail of the IWC profiles, qualitatively the forward model has captured the behaviour on the larger scale.

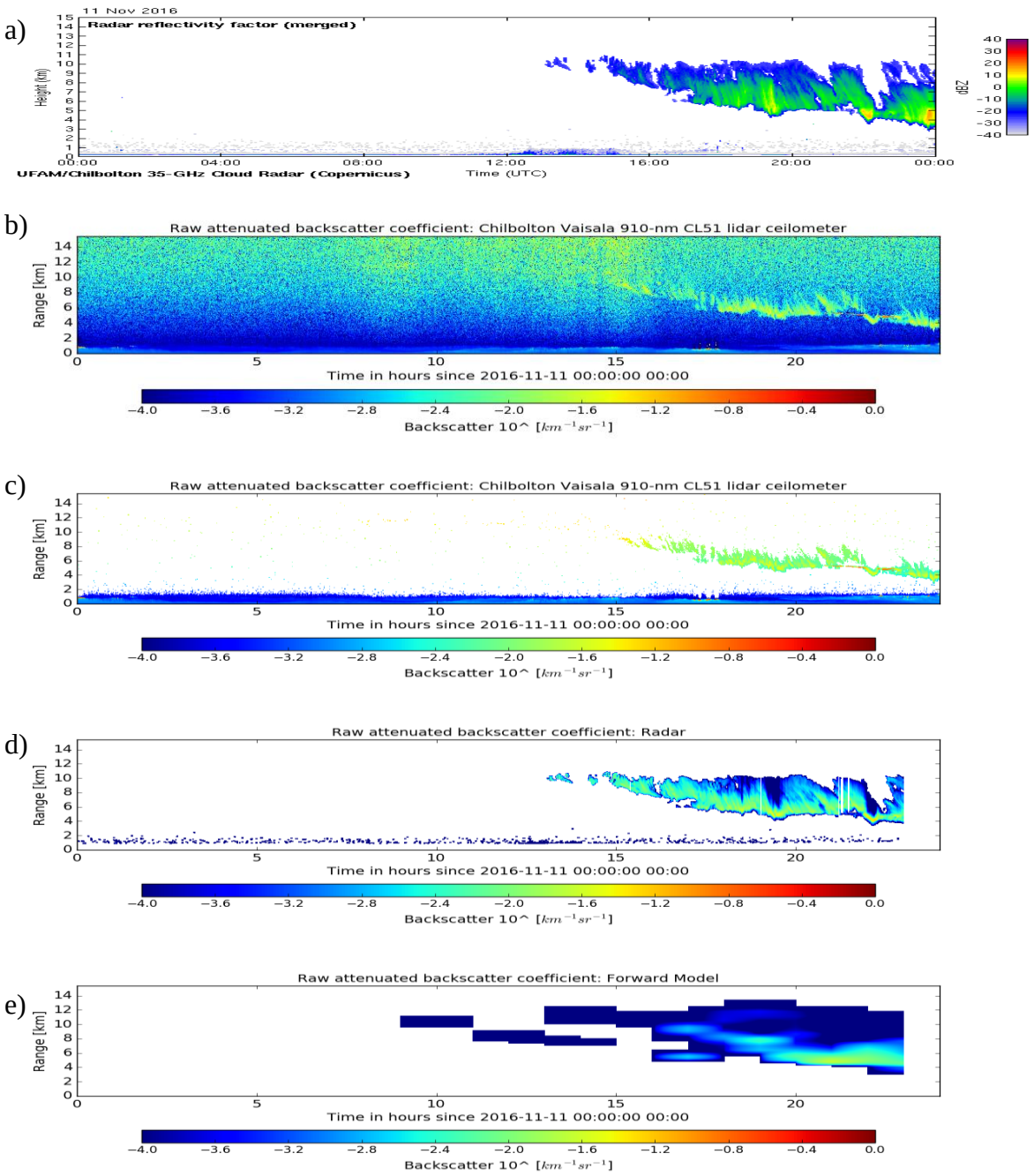

Figure 5.12: Ice cloud forward model case study: 11th November 2016. Panel a) shows the radar reflectivity factor (Z) from the Chilbolton 35 GHz radar (plot source: http://www.met.rdg.ac.uk/radar/cgi-bin/cloudarchive.cgi?date=20161111), panel b) shows the Vaisala CL51 observed attenuated backscatter, panel c) shows the Vaisala CL51 observed attenuated backscatter with the noise removed, panel d) shows the forward modelled attenuated backscatter for the radar derived IWC and panel e) shows the forward modelled attenuated backscatter for the UKV IWC.

5.8.2 3rd March 2017

Figure 5.13 shows a second case study, this one for 3rd March 2017. On this day, an occluded front passed over the Chilbolton Observatory, resulting in the frontal system structure visible in the radar reflectivity in Figure 5.13a.There is a layer of ice cloud present throughout the entire day. However, due to the lower liquid water cloud of the front, and the rain which is shown by the high (red end of scale) reflectivity in Figure 5.13a, the ceilometer is unable to observe much of the cloud. Figure 5.13b shows the ceilometer attenuated backscatter with the noise removed. In the first five hours of the day, the ice cloud at the front of the front is visible, with a lowering cloud base height, as the front moves across. From 5.00 hrs, however, the rain and low cloud attenuated the ceilometer signal so it does not observe the higher ice cloud. Figure 5.13c and Figure 5.13d show the forward modelled attenuated backscatter from the radar derived IWC and the UKV IWC, respectively. The ice cloud forward model does not include liquid water and therefore does not include the attenuation due to liquid water cloud. Consequently, both have the ice cloud after 5.00 hrs that the ceilometer does not observe. Note that the gaps in the radar attenuated backscatter (Figure 5.13c) are due to missing data in the IWC file, where the radar signal is attenuated by rain and not saved by Cloudnet (Illingworth et al., 2007). Figure 5.13d shows that the IWC derived from the UKV does result in a similar backscatter to that observed by the ceilometer. In the first 5.00 hrs there is clearly a layer of ice cloud where the cloud base lowers as the front moves over.

From 3.00 to 5.00 hrs, the UKV forward modelled attenuated backscatter has a similar cloud base to the ceilometer observed attenuated backscatter; going from 4 km down to 2km. However, from 0.00 to 3.00 hrs, the forward modelled attenuated backscatter starts a little low; starting at 6 km, compared to the ceilometer attenuated backscatter which starts at 8 km. The UKV forward modelled attenuated backscatter cloud base then does not lower as quickly as the observed cloud base.

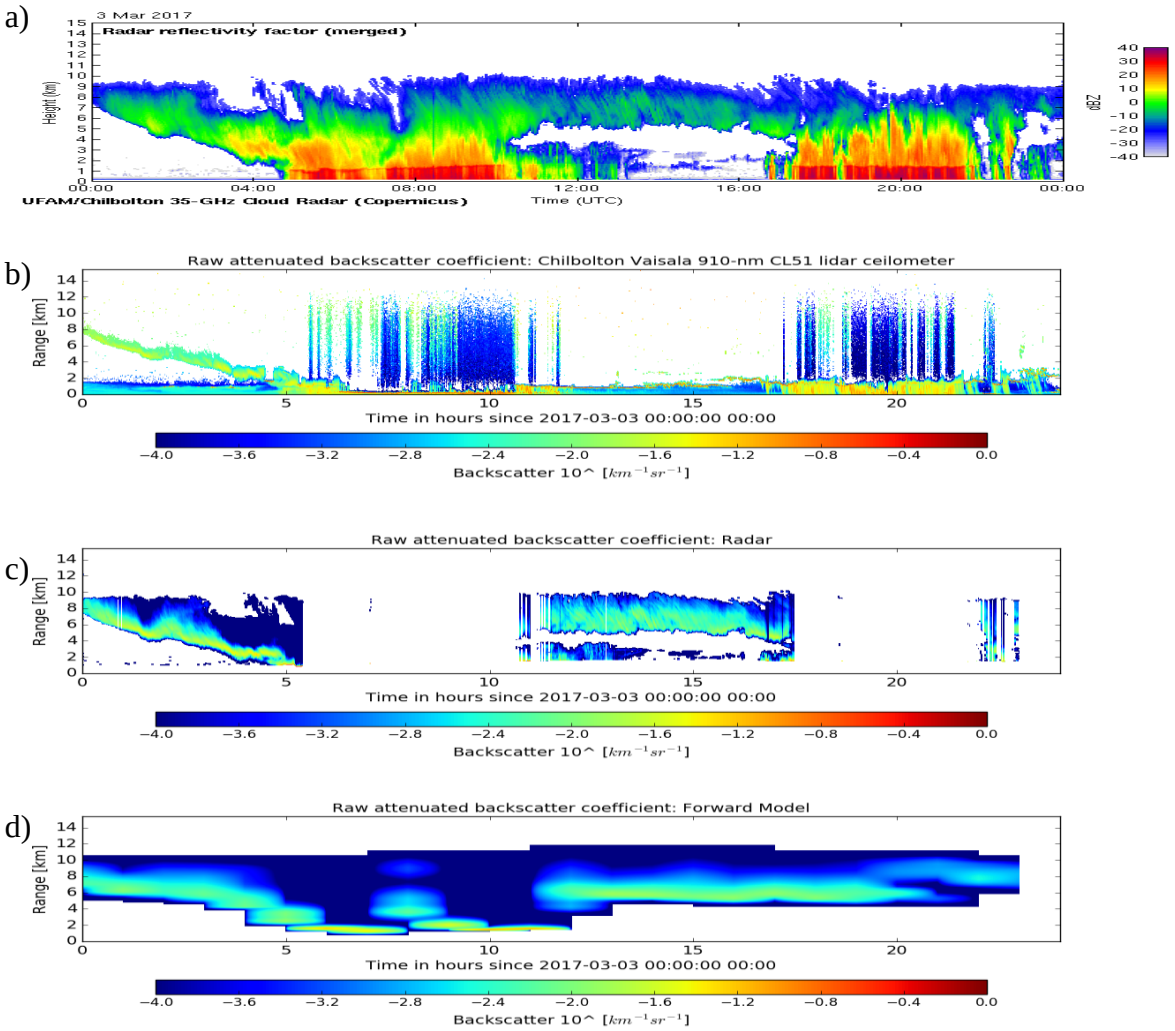

Figure 5.13: Ice cloud forward model case study: 3rd March 2017. Panel a) shows the radar reflectivity factor (Z) from the Chilbolton 35 GHz radar (plot source: http://www.met.rdg.ac.uk/radar/cgi-bin/cloudarchive.cgi?date=20170303), panel b) shows the Vaisala CL51 observed attenuated backscatter with the noise removed, panel c) shows the forward modelled attenuated backscatter for the radar derived IWC and panel d) shows the forward modelled attenuated backscatter for the UKV IWC.

In both figure 5.12 and figure 5.13, the attenuated backscatter from the UKV derived IWC is systematically lower than the ceilometer observed attenuated backscatter. The radar derived

attenuated backscatter, however, is of a similar magnitude to the ceilometer, suggesting that this is due to too little IWC in the UKV and not an error in the forward model.

5.9 Averaging

Section 5.6 described the need for a certain resolution to resolve the attenuation in the forward model. This resulted in the UKV IWC being interpolated onto a 10 m resolution, which is also ideal for comparing to the ceilometer data because it also has a range resolution of 10 m. The second consideration when comparing the forward modelled attenuated backscatter data with the ceilometer attenuated backscatter is the temporal and spatial resolution. The UKV model data has a one hour resolution, the radar data has a 50 second resolution and the ceilometer has a 30 second temporal resolution, but the observations only provide a vertical profile at a single point. To compare the three data sets, some averaging is clearly necessary. The following section considers averaging periods and the implications this has for the data.

5.9.1 Ceilometer Data

The Vaisala CL51 ceilometer records a profile of attenuated backscatter every 30 seconds. As a result, the ceilometer is able to observe some microphysical processes, such as the fall streaks which are visible in Figure 5.12b and in Figure 5.13b (the slanted streaks within the cloud, with an attenuated backscatter of around 10e-1.5 km^{-1} sr^{-1} – yellow on the colour scale). However, it is not possible for the UKV to model such detail; therefore the ceilometer attenuated backscatter is smoothed to average out the microphysical detail and focus on the macrophysical. That is, the location of the cloud and the magnitude of the cloud-scale attenuated backscatter. An appropriate averaging period must be chosen that will do this, without corrupting the trends of cloud height and the attenuated backscatter.

5.9.1.1 Possible averaging methods

Two methods of data averaging are considered; using profiles from the time leading up to a given time or using an averaging window centred on a given time. Figure 5.14 shows an example of averaged profiles of attenuated backscatter for the Vaisala CL51 ceilometer. In Figure 5.14a, the averaging is done for the profiles leading up to a given time; for example, the red line shows the 5 minutes leading up to 2.00 hrs. The impact of a sloping front with descending cloud base is clearly visible, as the longer the averaging period the higher the cloud. Figure 5.14b, however, shows all the profiles have the same cloud base.

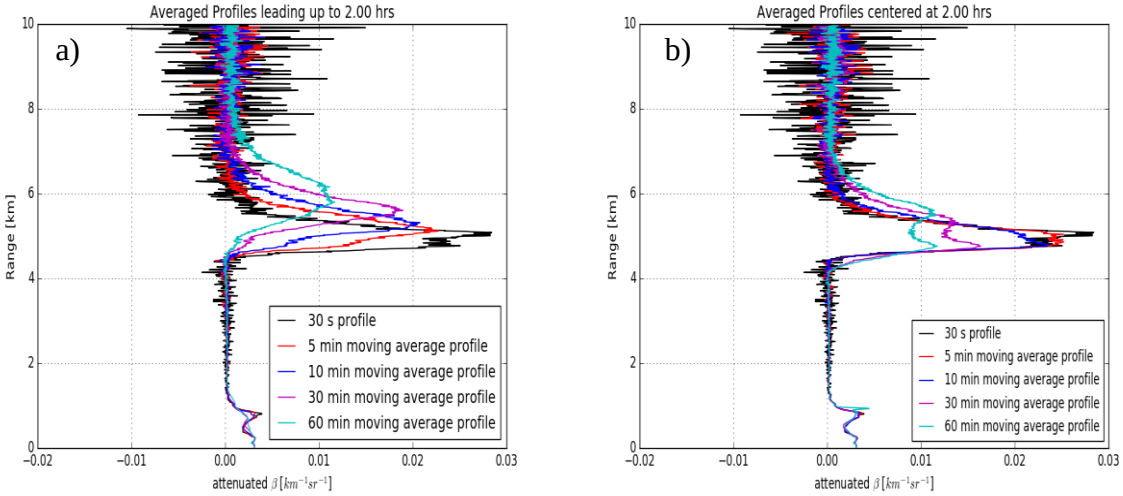

Figure 5.14: Profiles of attenuated backscatter observed by the Chilbolton Vaisala CL51 ceilometer averaged over different periods for a reference time of 2.00 hrs, on 3rd March 2017. The 30 second profile of attenuated backscatter as reported by the instrument is shown in black. Panel a) shows the profile of attenuated backscatter averaged for time periods leading up to 2.00 hrs. Panel b) shows the profile of attenuated backscatter averaged with a centre point at 2.00 hrs.

Figure 5.11a and Figure 5.11b both show the impact of averaging on the magnitude of the attenuated backscatter; the longer the averaging period, the lower the magnitude of the backscatter. As the fall streaks will cause the larger backscatter due to larger particles of ice,

the smaller temporal averages (for example, 5 minutes, 10, minutes) may be more influenced by processes such as fall streaks and therefore can be expected to have a higher backscatter than the UKV derived attenuated backscatter. The longer temporal averaging (for example, 30 minutes) smooth out the smaller scale processes that the UKV cannot resolve. If the averaging period is very long, the profiles are a convolution of both the large scale changes in cloud boundaries (e.g. advection of a sloping frontal surface) as well as the microphysical structure. Therefore, an averaging window which lies between these regimes is chosen; a 30 minute averaging is applied to the ceilometer and radar data for comparison.

5.9.2 UKV Data

5.9.2.1 Interpolation

For comparison with the Vaisala CL51 ceilometer data, the UKV derived attenuated backscatter is interpolated onto the ceilometer temporal grid, a resolution of 30 seconds. Obviously this is not a true representation of 30 seconds; the UKV IWC samples a snapshot every one hour from operational archived 3D fields. Small-scale variability can therefore not be studied by considering consecutive outputs, but only by comparing adjacent grid boxes (which are 1.5 km apart), compared to consecutive profiles (30 seconds apart) in the observations.

5.9.2.2 Averaging in space

One method which could compensate for the coarse temporal resolution of the UKV data is to use a spatial averaging to represent the time period. As this study focuses on thick, attenuating ice cloud, these tend to be large cloud decks, covering several model grid boxes. The ceilometer is a fixed point observation, taking measurements as the cloud passes over. By averaging over several grid boxes from downwind of Chilbolton, a transect can be used to represent the cloud

which moves over the Chilbolton observatory over a set time period. For example, on 11th November 2016 there was a period of ice cloud at approximately 5 km. The wind speed at this height was 10 m s^{-1}, with a SE direction.

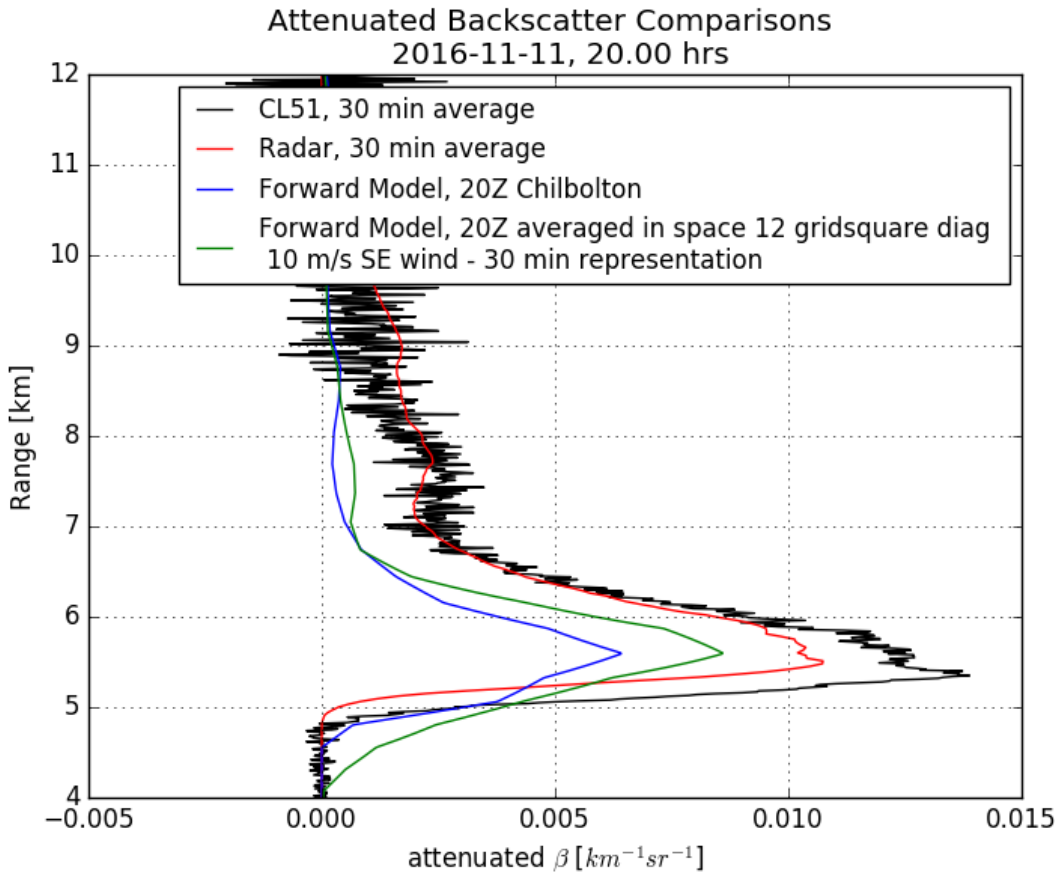

Figure 5.15: Profiles of attenuated backscatter for a reference time of 20 hrs, on 11th November 2016. The black line shows a 30 minute average profile centred at 20 hrs from the Chilbolton Vaisala CL51 ceilometer observed attenuated backscatter and the red line shows a 30 minute average profile centred at 20 hrs from the Chilbolton 35 GHz radar derived attenuated backscatter. The blue line shows the UKV derived profile of attenuated backscatter for the grid box covering Chilbolton at 20 Z and the green line shows the average of the UKV derived attenuated backscatter averaged for a diagonal transect of 12 grid boxes centred at Chilbolton for 20 Z.

Therefore, for a 30-minute average for the ceilometer observation, this time can be represented by 12 UKV grid boxes on a diagonal transect. Figure 5.15 shows this example, for a reference time of 20.00 hrs. Figure 5.15 compares 30 minute averaged profiles of attenuated backscatter observed by the ceilometer (in black) with the UKV derived attenuated backscatter; in blue is the profile for the UKV IWC at 20 Z for the Chilbolton grid box and in green is the averaged profile for 12 grid boxes diagonally centred at Chilbolton to represent a 30 minute average. The averaged profile (green) has a larger magnitude than the individual profile (blue). However, the UKV averaged profile is still half the magnitude of the ceilometer attenuated backscatter.

5.10 Profile Comparisons

Section 5.8 indicated that the UKV derived attenuated backscatter had a lower magnitude compared to the ceilometer attenuated backscatter. The following section shows some vertical profiles of attenuated backscatter from the various case studies, highlighting and quantifying some of the differences.

5.10.1 3rd March 2017

Figure 5.16 shows 30 minute averaged profiles of attenuated backscatter. The solid line shows the mean and the dotted lines shows the interquartile range, giving an indication of the spread of the attenuated backscatter during the 30 minute averaging period.

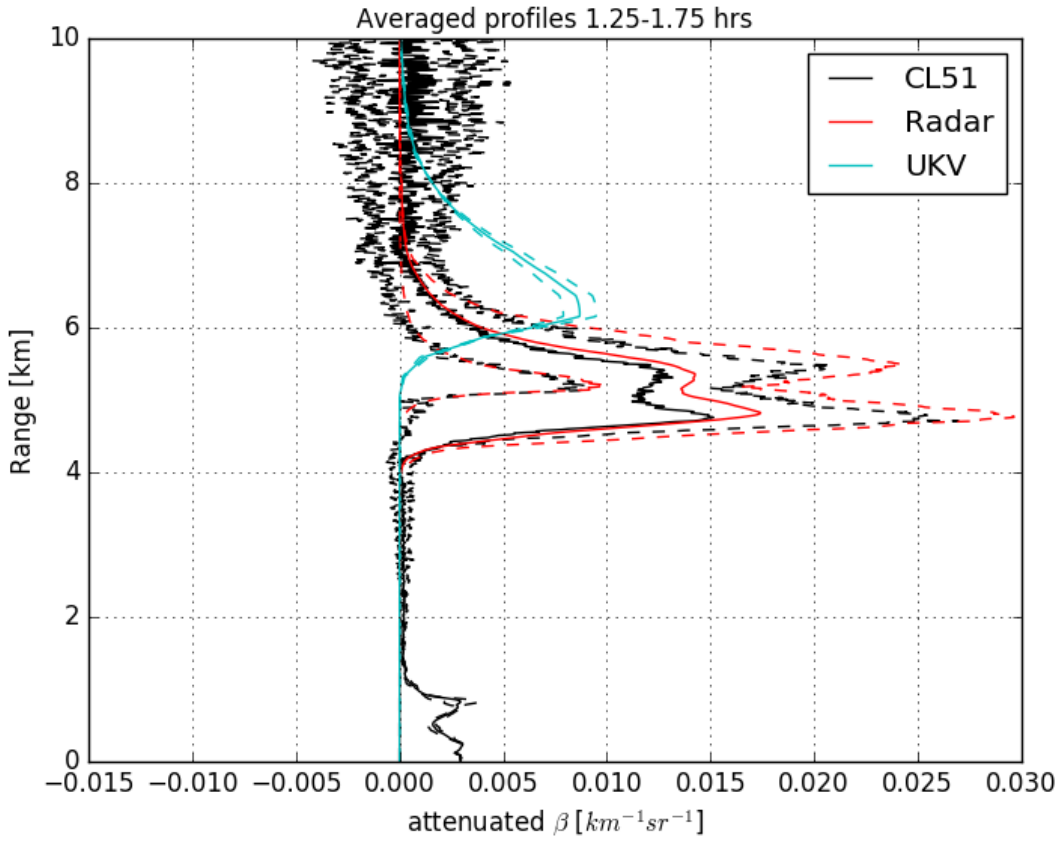

Figure 5.16: 30 minute averaged vertical profiles of attenuated backscatter centred at 1.5 hrs on 3rd March 2017, where the solid line shows the mean and the dotted lines show the interquartile range. The attenuated backscatter observed by the Chilbolton Vaisala CL51 ceilometer is in black, the attenuated backscatter calculated by the forward model from the radar derived IWC is in red and the attenuated backscatter calculated by the forward model from the UKV derived IWC is in cyan. The radar and UKV attenuated backscatter was interpolated onto the same resolution as the ceilometer data, before the 30 minute mean and standard deviation was calculated.

Figure 5.16 shows that the attenuated backscatter profiles from the radar (the red lines) and ceilometer (the black lines) are remarkable similar despite the large error associated with deriving the IWC from the radar reflectivity factor; the difference between the maximum values of attenuated backscatter is 12.5 %. The attenuated backscatter derived from the UKV IWC

(the cyan lines) is, however, very different, both in magnitude and position. The peak (or maximum) of the attenuated backscatter is 1.2 km above the ceilometer peak attenuated backscatter and there is a 53.2 % difference between the two peaks. This suggests that the ice cloud in the UKV model is too high in altitude and too low in the magnitude of IWC.

5.10.2 2nd March 2017

Figure 5.17 also shows 30 minute averaged profiles for ceilometer, radar and UKV attenuated backscatter, this time for 2nd March 2017, centred at 22.00 hrs. The attenuated backscatter profiles from the radar (the red lines) and ceilometer (the black lines) are again showing the cloud at the same height, and again the UKV (the cyan lines) cloud height does not match; in this case it is 2.4 km lower than the observed ice cloud. There is a 30 % difference between the mean peak ceilometer attenuated backscatter and the mean peak radar derived attenuated backscatter. Although this difference is a little larger than the difference in Figure 5.16, the radar derived attenuated backscatter profile still falls within the interquartile range of the ceilometer attenuated backscatter, implying that both instruments are observing the same cloud. The UKV derived peak attenuated backscatter shows a 34 % difference to the peak ceilometer attenuated backscatter and is 2.2 km below the peak ceilometer attenuated backscatter; again the UKV IWC is too low. However, in this case, the ice cloud altitude is too low compared to the previous example where it was too high.

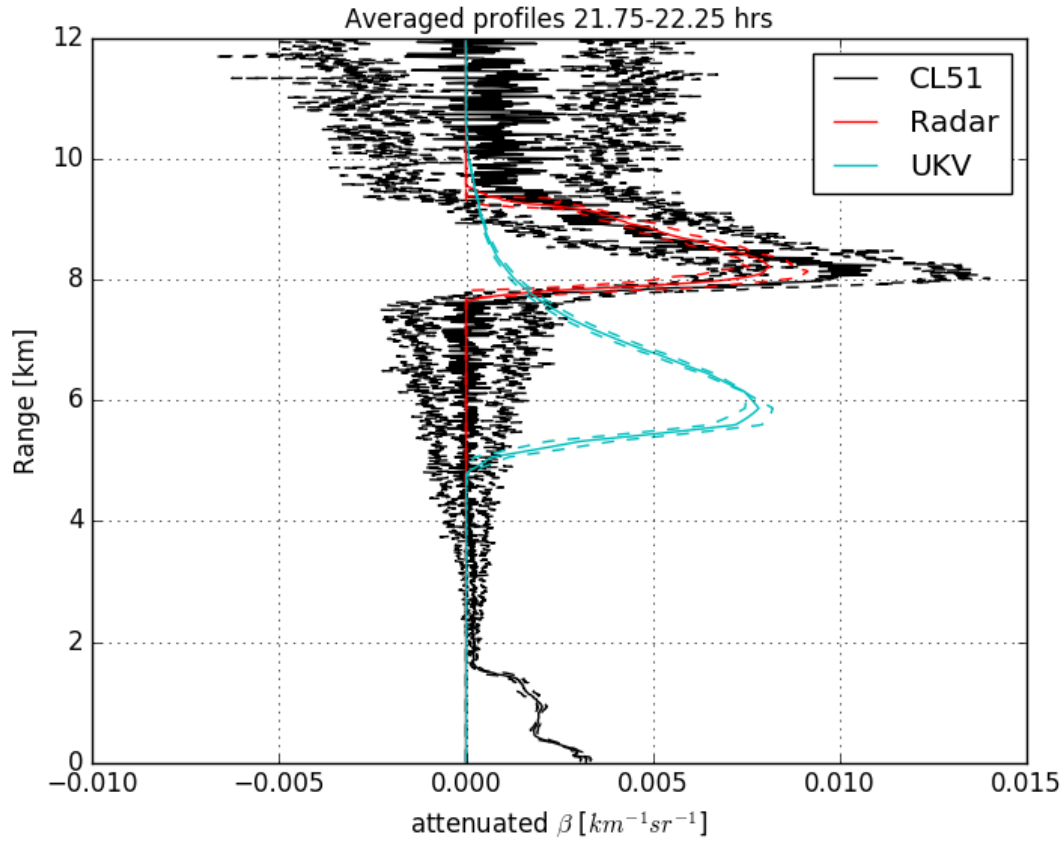

Figure 5.17: 30 minute averaged vertical profiles of attenuated backscatter centred at 22.00 hrs on 3rd March 2017, where the solid line shows the mean and the dotted lines show the interquartile range. The attenuated backscatter observed by the Chilbolton Vaisala CL51 ceilometer is in black, the attenuated backscatter calculated by the forward model from the radar derived IWC is in red and the attenuated backscatter calculated by the forward model from the UKV derived IWC is in cyan. The radar and UKV attenuated backscatter was interpolated onto the same resolution as the ceilometer data, before the 30 minute mean and standard deviation was calculated.

5.10.3 4th March 2017

Figure 5.12 shows a third example of a 30 minute profile comparison. During this period, the attenuated backscatter observed by the ceilometer is much stronger, with a peak difference of

93 % and 84 % compared to the radar and the UKV derived attenuated backscatter, respectively. However, the cloud heights are all within approximately 200 m of each other.

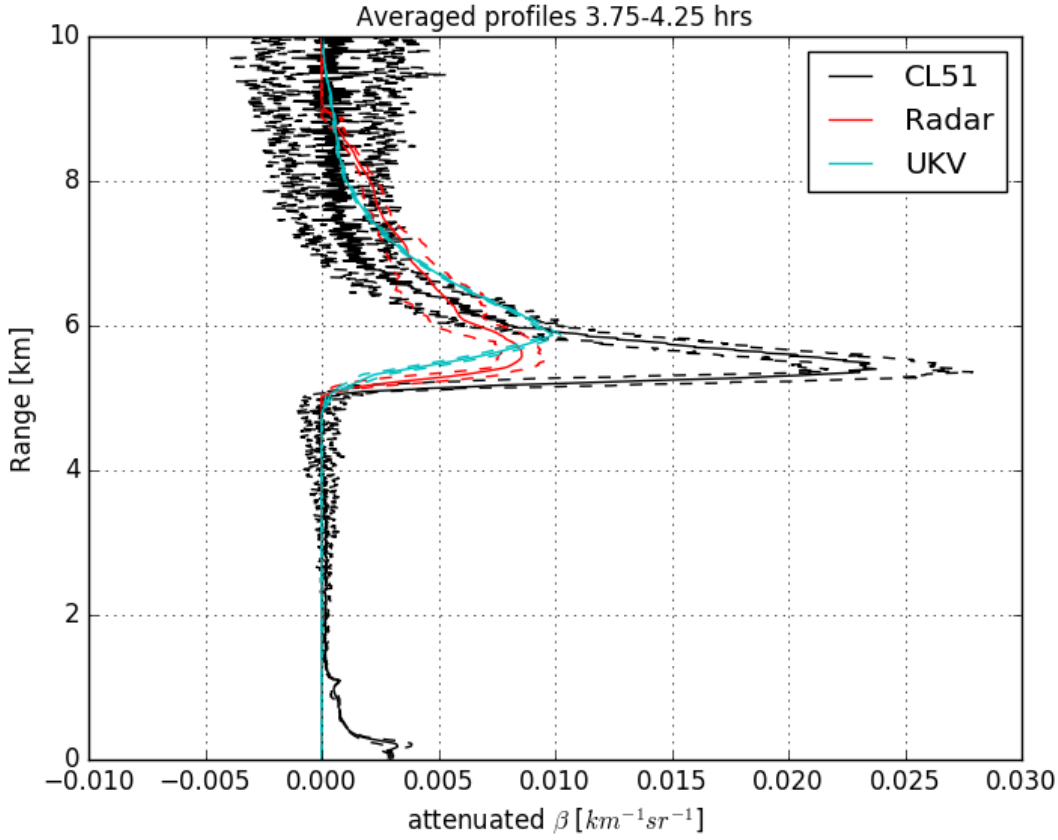

Figure 5.18: 30 minute averaged vertical profiles of attenuated backscatter centred at 4.00 hrs on 4th March 2017, where the solid line shows the mean and the dotted line shows the interquartile range. The attenuated backscatter observed by the Chilbolton Vaisala CL51 ceilometer is in black, the attenuated backscatter calculated by the forward model from the radar derived IWC is in red and the attenuated backscatter calculated by the forward model from the UKV derived IWC is in cyan. The radar and UKV attenuated backscatter was interpolated onto the same resolution as the ceilometer data, before the 30 minute mean and standard deviation was calculated.

5.11 Systematic evaluation of short-range model forecasts and O-B Results

The previous section discussed variations in the profile height and magnitude of the attenuated backscatter for three different case studies. This section introduces the use of departures from the observations, a key step in assessing the suitability of the data for use in data assimilation to improve forecast models. This is sometimes referred to as the O-B statistics, where O is the observation and B is the model background. For the model background in this study, the forecast at 21 Z is used. Here we show an example from a single case study, and then the statistics for all nine case studies.

5.11.1 O-B for 4th March 2017

On 4th March 2017 there were several hours of thick attenuating ice cloud over the Chilbolton Observatory (see Figure 5.10 for radar and ceilometer quicklook). Figure 5.19a shows the attenuated backscatter quicklook as derived from the UKV IWC. There is a period of ice cloud from the start of the day, through to 7.00 hrs just as the ceilometer observed. The ceilometer does not observe ice cloud in the first hour due to attenuation by lower cloud, however the radar suggests there was ice cloud present at approximately 6 km – see figure 5.10. However, where the observations show this cloud breaking up and dissipating at 7 hrs, the UKV derived attenuated backscatter shows cloud continuing throughout the whole day. This is consistent with studies that have investigated the ice cloud representation in global circulation models (GCMs) and report that GCMs generally overestimate the ice cloud fraction (e.g. Wilkinson et al., 2008; Delanoë et al., 2011)

Here, we concentrate on a period where both the UKV and the ceilometer observation show ice cloud present, focussing on the magnitude and height of the ice cloud. As before, the

ceilometer data has a 30 minute averaging applied. Figure 5.16b and Figure 5.16c show histograms of the value of the maximum attenuated backscatter for the profiles between 3.5 and 7 hrs, as observed by Vaisala CL51 ceilometer and as derived from the UKV IWC, respectively. Despite the 30 minute averaging applied to the ceilometer, the maximum attenuated backscatter has quite a wide distribution, with a mean of 0.019 km^{-1} sr^{-1} and a standard deviation of 0.006 km^{-1} sr^{-1}, which is 32 % of the mean. The UKV attenuated backscatter, however, is very much concentrated between 0.0075 and 0.01 km^{-1} sr^{-1}, with a mean of 0.009 ± 0.003 km^{-1} sr^{-1}. Again, the standard deviation is 32% of the mean, although the value of the standard deviation is half that of the ceilometer's standard deviation. This is because the mean of the maximum attenuated backscatter for the UKV is half that for the ceilometer, suggesting that the magnitude of the IWC in the UKV is too low. This is highlighted in figure 5.19d, which shows the O-B for the maximum attenuated backscatter for profiles between 3.5 and 7 hrs. For most of the period, the difference (the O-B) is large; above 0.01 km^{-1} sr^{-1} for the first two hours. Only in the final hour of figure 5.19d does the O-B drop to close to zero and become negative as the UKV maximum attenuated backscatter values exceed the ceilometer attenuated backscatter. However, as discussed, the ceilometer does not observe much ice cloud past this period and may be beginning to dissipate, whereas the UKV shows a continuous ice cloud for much of the day.

Figure 5.19e shows the O-B for the cloud height, represented by the height of the maximum backscatter. Note that CBH is a somewhat arbitrary term and ceilometer manufacturers each have their own proprietary algorithm for determining CBH. For most of the period, the value of O-B is negative, suggesting that, at least for this case study, the UKV IWC is located too high. However, the mean O-B is -0.325 km; at the height of the ice cloud (approximately 6 km), the UKV grid boxes have a resolution of 250 m. Therefore, this suggests that for this case study, the height of the UKV IWC is at most out by one model level.

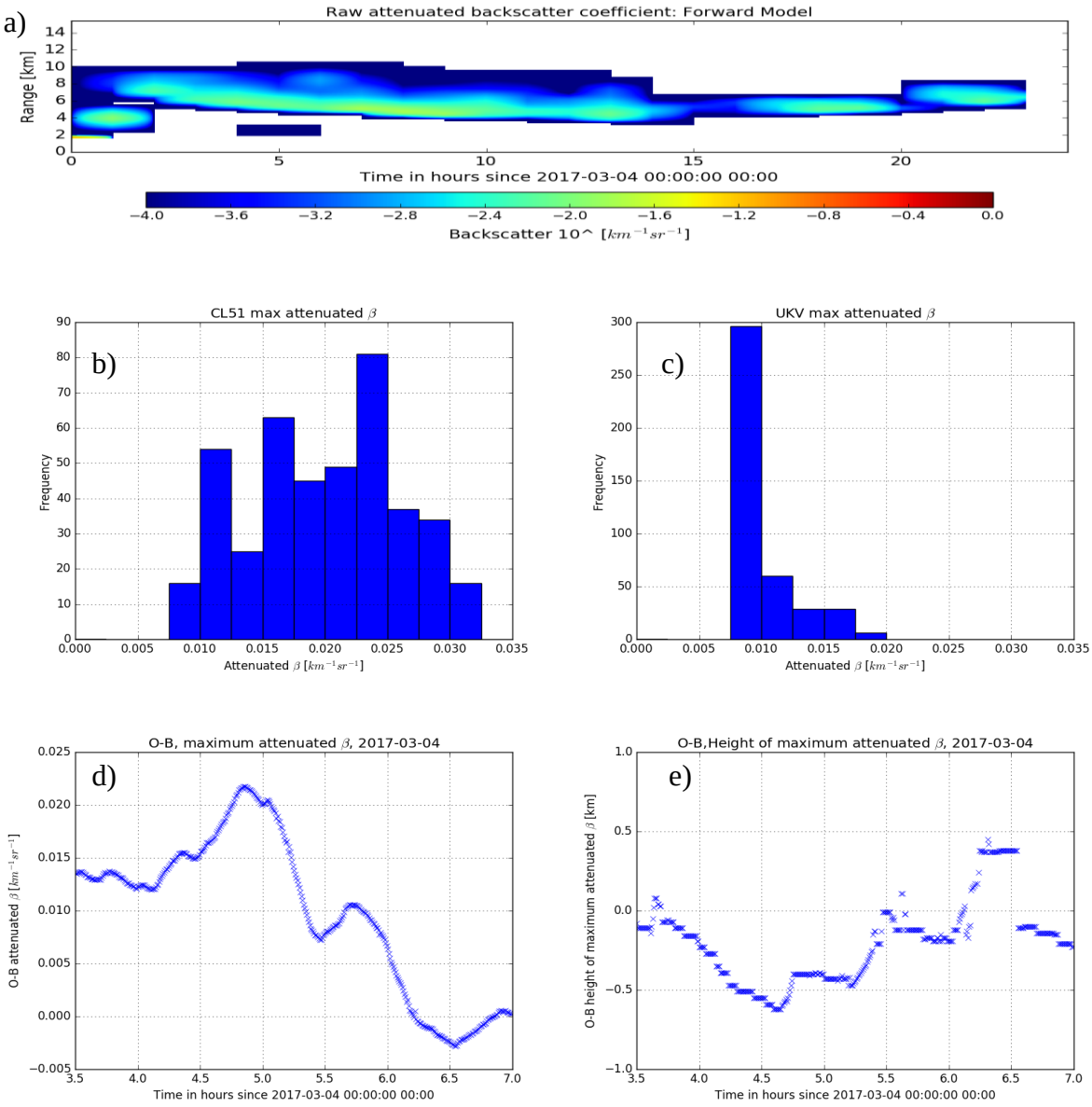

Figure 5.19: Comparison of CL51 and UKV derived attenuated backscatter for 4th March 2017, 3.5-7.0 hrs. Panel a) shows the UKV derived attenuated backscatter for the whole day. Panel b) shows the distribution of the profile maximum attenuated backscatter for Vaisala CL51 profiles and panel c) shows the distribution of the profile maximum attenuated backscatter for UKV derived profiles. Panel d) shows the Vaisala CL51 profile maximum attenuated backscatter (O) minus the UKV derived profile maximum attenuated backscatter (B). Panel e) shows the Vaisala CL51 height of the profile maximum attenuated backscatter (O) minus the UKV height of the derived profile maximum attenuated backscatter (B).

Figure 5.20 shows the O-B for attenuated backscatter, again for the period 3.5 to 7 hrs, this time for the whole cloud rather than only the peak attenuated backscatter of each profile. Only the ice cloud is used as the forward model does not include aerosol, which the ceilometer observes in the boundary level. As shown in Figure 5.16b, Figure 5.20 also shows that the attenuated backscatter derived from the UKV is too low, suggesting that the UKV IWC is too low.

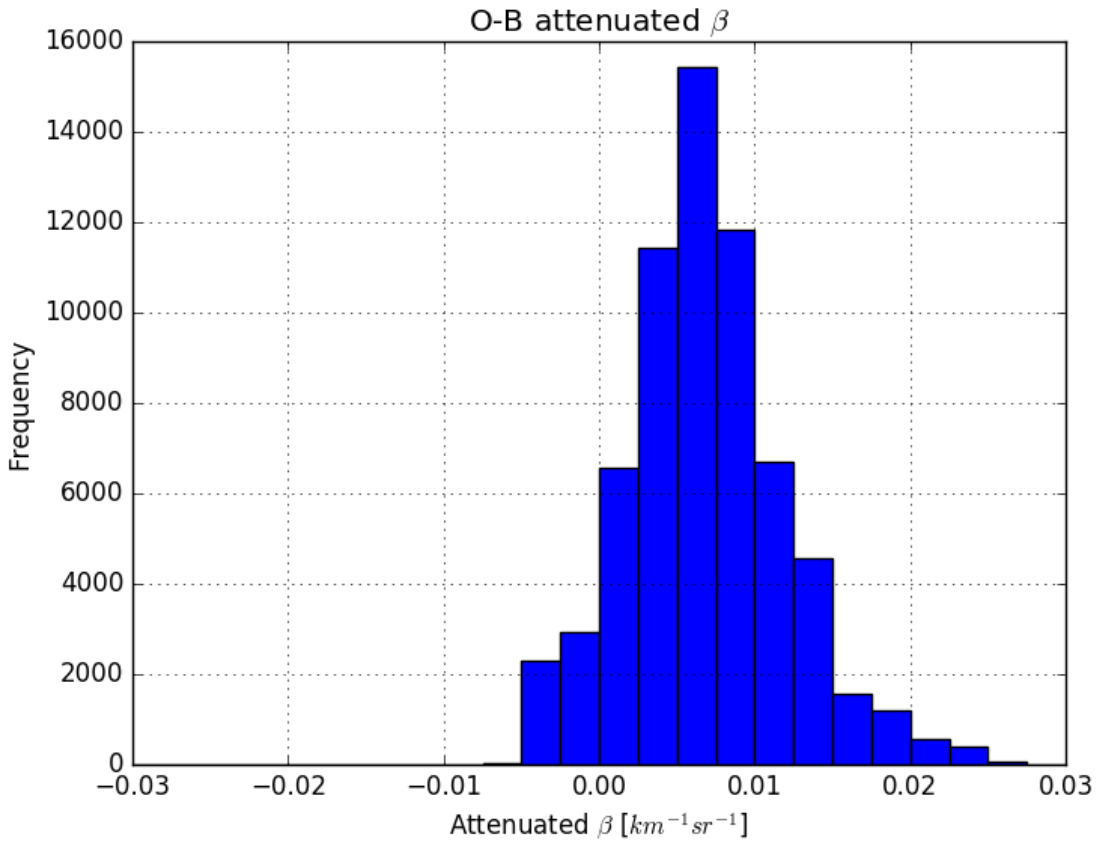

Figure 5.20: Vaisala CL51 attenuated backscatter (O) minus the UKV derived attenuated backscatter (B) for 4th March 2017, 3.5 – 7 hrs.

5.11.2 O-B for multiple case studies

The follow section investigates if the trends found for the 4th March 2017 are held true for all the case studies. The data from all of the case studies, for periods where both the ceilometer

and the UKV showed ice cloud, were used to calculate O-B values and the results are depicted in figure 5.21.

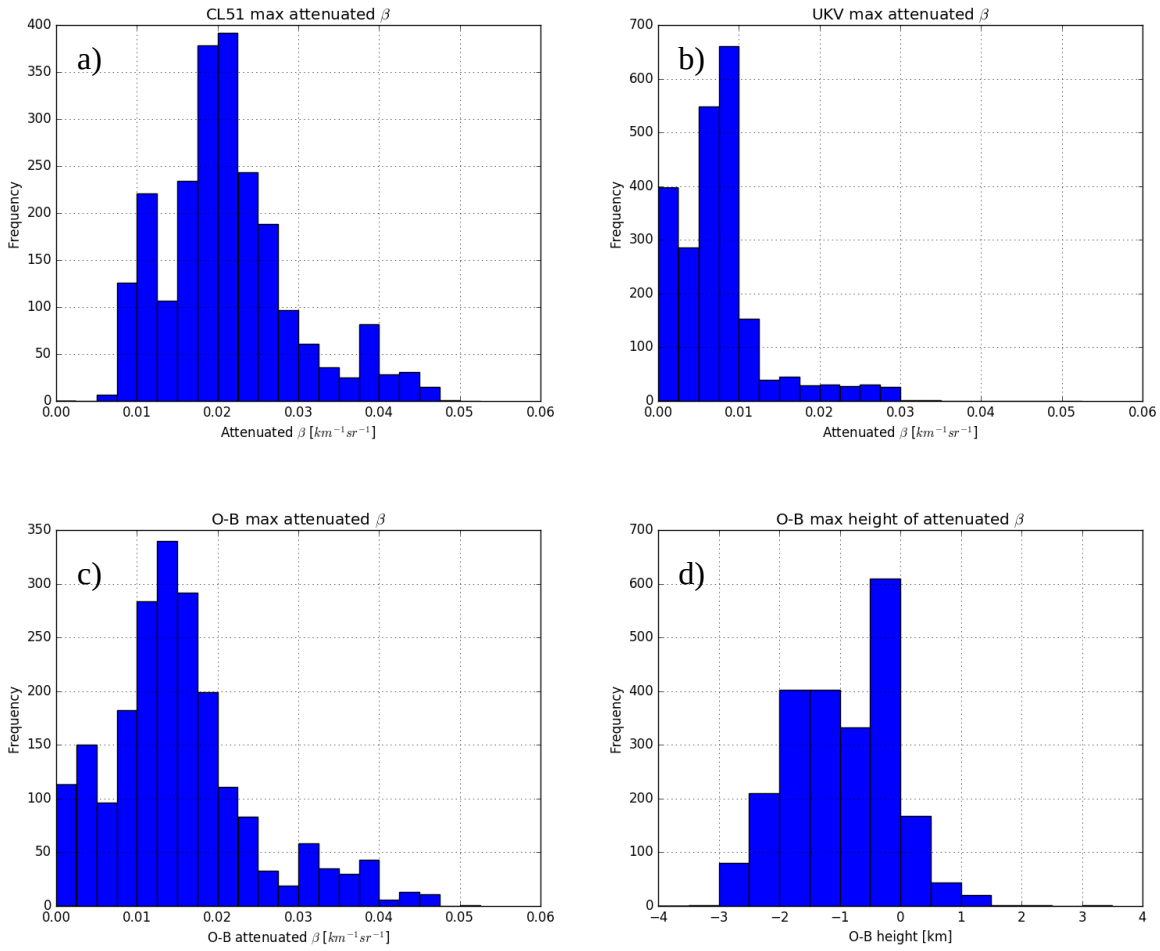

Figure 5.21: Using data from all 9 case studies, panel a) shows the distribution of the profile maximum attenuated backscatter for Vaisala CL51 profiles and panel b) shows the distribution of the profile maximum attenuated backscatter for UKV derived profiles. Panel c) shows the Vaisala CL51 maximum attenuated backscatter (O) minus the UKV derived maximum attenuated backscatter (B) and panel d) shows the height of the Vaisala CL51maximum attenuated backscatter (O) minus the height of the UKV derived maximum attenuated backscatter (B).

As in figure 5.19, the histograms in figure 5.21a show the distribution of the maximum attenuated backscatter from the ceilometer profiles and in figure 5.21b show the maximum

attenuated backscatter from the UKV profiles. Similarly to the single example in Section 5.9.1, the ceilometer data has a mean value of 0.02 km^{-1} $sr^{-1}$and the UKV mean maximum attenuated backscatter is less than half this, with a value of 0.008 km^{-1} sr^{-1}. As a result, the O-B is skewed to positive values, as shown in figure 5.21c where the mean O-B is 0.014 ± 0.01km^{-1} sr^{-1}. The mean O-B is of the order of the values of the attenuated backscatter in ice cloud, showing that the UKV derived attenuated backscatter is very low compared to the ceilometer observed attenuated backscatter. Although the sample size is too small to make conclusive judgments, these results do suggest that the UKV IWC is systematically too low.

Figure 5.21d shows the O-B of the ice cloud height, where the height of the profile's maximum backscatter has again been used as a proxy. The histogram is skewed to negative values, with a mean of -0.95 km and a difference of -2 km or more in almost 200 profiles, suggesting that the altitude of the UKV IWC is systematically too high.

5.12 Lidar ratio sensitivity

Section 5.5 described the calculation of the lidar ratio from ceilometer observations in thick, attenuating cloud. It was shown that the lidar ratio varied by approximately ± 5 sr. As the modelled attenuated backscatter is calculated using the lidar ratio, an error in the lidar ratio would propagate to an error in the modelled backscatter. Figure 5.22 shows an example of a sensitivity test to lidar ratio variability. The ice cloud forward model is used to predict profiles of attenuated backscatter, derived from the UKV IWC, using different values of lidar ratio. As Figure 5.22 shows, a lidar ratio of 35 sr results in the peak of the attenuated backscatter being approximately 28 % greater than if a lidar ratio of 45 sr is used. While this shows that the forward modelled attenuated backscatter is sensitive to the value of lidar ratio used, the difference in the peak attenuated backscatter as a result in the use of a different lidar ratio is not large enough in magnitude to fully explain the systematically lower UKV derived

attenuated backscatter when compared to the ceilometer observed attenuated backscatter.

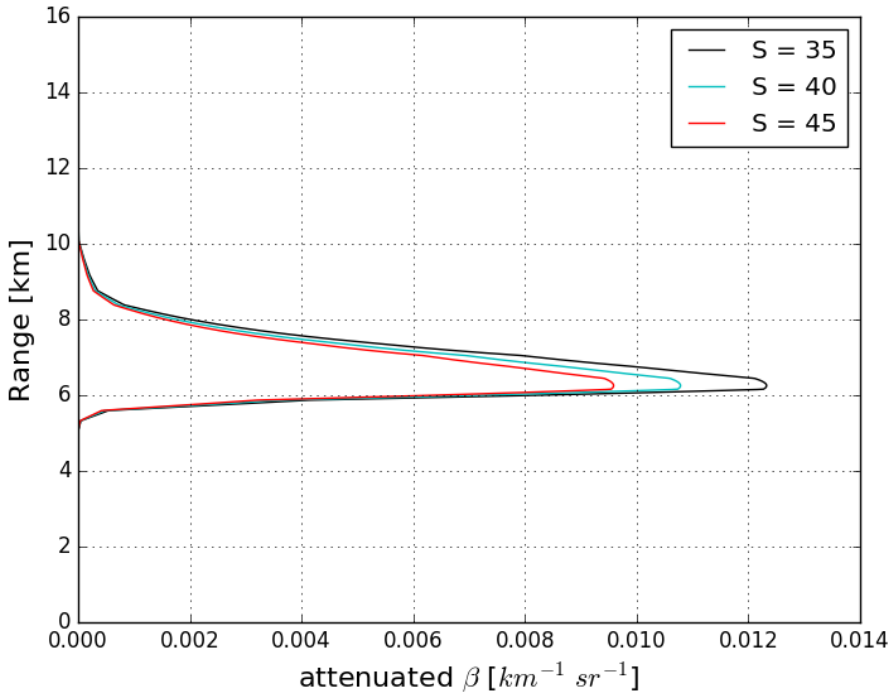

Figure 5.22: Profiles of attenuated backscatter derived from UKV IWC. The attenuated backscatter was calculated using a lidar ratio of 35 sr (black line), 40 sr (cyan line) and 45 sr (red line).

5.13 Sensitivity to the value of $\frac{IWC}{\sigma}$

Section 5.2 discussed the validity of using a constant value of $\frac{IWC}{\sigma}$ and hence a constant value of R_{eff}. To test the response of the ice attenuated backscatter forward model, a similar method to Wilkinson et al. (2008) is used; the value of $\frac{IWC}{\sigma}$ is doubled and an attenuated backscatter profile derived and then the value of $\frac{IWC}{\sigma}$ is halved and an attenuated backscatter profile is derived.

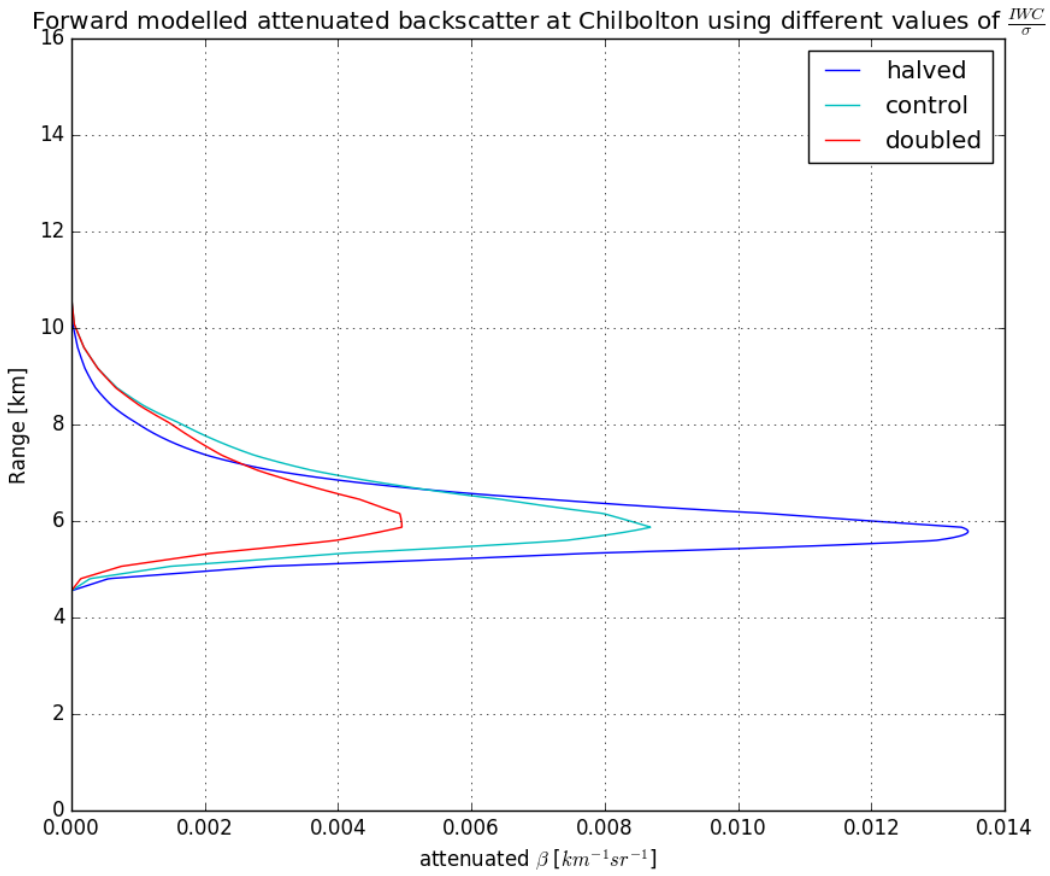

Figure 5.23: Profiles of attenuated backscatter derived from UKV IWC. The attenuated backscatter was calculated using a value $\frac{IWC}{\sigma} = 0.0175\ kg\ m^{-1}$ *(blue line),* $\frac{IWC}{\sigma} = 0.035\ kg\ m^{-1}$ *(cyan line) and* $\frac{IWC}{\sigma} = 0.07\ kg\ m^{-1}$ *(red line).*

Figure 5.23 shows that halving the value of $\frac{IWC}{\sigma}$ results in an increase in the UKV derived attenuated backscatter of about 45 % and doubling the value of $\frac{IWC}{\sigma}$ results in a decrease of the UKV derived attenuated backscatter by about 45 %. As shown in figure 5.3, the majority of values observed by Heymsfield et al. (2005) fall within this range tested here, implying that there may be a maximum bias due to the constant value of $\frac{IWC}{\sigma}$ used in the ice cloud forward model of ± 45 %.

5.14 Conclusions

This chapter has detailed the development of a novel forward model for ice cloud which uses IWC to calculate a vertical profile of attenuated backscatter. A second moment approximation is assumed for particle area and mass, so that IWC is proportional to extinction. The lidar ratio for ice cloud was calculated using ceilometer observations of thick, attenuating ice cloud, found to be 42.8 ± 10.9 sr. This lidar ratio was used to calculate backscatter and attenuation applied. Simulated profiles of IWC showed that the data needed to be discretized onto a finer resolution than the UKV data in order to resolve the attenuation due to extinction so the UKV IWC was interpolated on to a 10 m resolution.

Comparisons between the UKV derived attenuated backscatter and the attenuated backscatter observed by the Vaisala CL51 ceilometer suggest that the UKV IWC is systematically too low in magnitude and too high in height. These two biases are likely to be linked; the lower temperature associated with the increase in height would result in a lower saturated vapour pressure and therefore a slower rate of condensation. Thus at a higher altitude, there would be less ice and therefore a lower attenuated backscatter, compared to a lower altitude. The bias in UKV derived attenuated backscatter does appear to agree with other studies comparing model IWC with observation IWC; for example, Delanoë et al (2011) found that for the global models tested, the larger values of IWC observed were always underestimated by the models.

This study has shown the potential for using ceilometer data to improve the forecasting of IWC in the UKV. Future work would be beneficial to further develop the forward model by testing on a larger data set and extending the observation data to include the ceilometer network. With this additional data, we would then be able to better quantify the O-B statistics. This forward model would also benefit from combining with a forward model for liquid water and aerosol, so that the modelled profiles of attenuated backscatter would better simulate the ceilometer observations.

Chapter 6:

Conclusions and recommendations for future work

Cloud and aerosols play an important part in our everyday life, influencing our behaviour, our safety and our health. The monitoring and study of cloud and aerosol properties is therefore a vital topic in the forecasting and research of weather and climate. Ceilometer networks provide a data source that has a high spatial and temporal density. They are relatively cheap to purchase and operate, they are generally reliable, and can run continuously with little to no human intervention and maintenance. Ceilometers were designed specifically to measure cloud base height (CBH) and visibility. However, ceilometers measure a vertical profile of attenuated backscatter and the use of these profiles has led to the development of several areas of research using ceilometers. Examples of the use of ceilometer profiles in a research environment are for validation of the representation of clouds in operational NWP models, for aerosol profiling, fog observations and predictions, and the retrieval of boundary layer mixing height levels.

6.1 Calibration

Chapter 3 discussed how the development of research using the vertical profiles of attenuated backscatter has resulted in the need for accurate calibration. Calibration of ceilometers using liquid water cloud was proposed by O'Connor et al. (2004) as a simple method that requires no additional instruments to compute a calibration coefficient. The technique relies on the use of the lidar ratio that is a constant for the droplets in liquid water cloud. This calibration technique has been further developed into a new algorithm, as follows:

1. To run operationally and automatically.
2. To remove unsuitable profiles where the cloud does not fully attenuate the ceilometer beam or where there is significant backscatter from aerosols.
3. To apply a range dependent multiple scattering correction that depends on the ceilometer optics.
4. To take into account manufacturer-dependent differences in the ceilometers. Profiles from very low cloud that lead to the saturation of the ceilometer receiver (particularly true in the case of Lufft ceilometers) are removed.
5. To checks the window transmission and pulse energy values to ensure that the optical systems are not artificially reducing the attenuated backscatter.
6. To apply a water vapour attenuation correction, where necessary. In the case of ceilometers with a wavelength of around 905-910 nm, the effect of atmospheric water vapour below the cloud on the laser signal must be considered, because this wavelength is in a weak water vapour absorption band. A novel method of correcting the attenuation due to water vapour has been implemented which uses the vapour profiles from a forecast analysis.

6.2 Calibration of the Met Office ceilometer network

Chapter 4 discusses the results of the calibration when the algorithm is applied to the instruments in the Met Office ceilometer network, which consisting of both Vaisala and Lufft ceilometers. It was demonstrated in this thesis that, over a period of 20 months, the running 90-day mean calibration coefficient for a generic ceilometer in the Met Office network is constant to within 3 % with no detectable annual cycle; thus, confirming the validity of the humidity and multiple scattering correction. For Gibraltar, where cloud cover is less prevalent than in the UK, the 90-day running mean calibration coefficient was constant to within 4%. The Lufft ceilometers, which operate at 1064 nm, are unaffected by water vapour attenuation but are more prone to saturation in liquid clouds. It was shown in this thesis that reliable calibration is still possible, provided the clouds used are above a certain altitude. This critical height threshold is instrument dependent but is typically around 2 km. Despite the more restricted sample of cloud profiles, a robust calibration is readily achieved, and, in the UK, the running mean 90-day calibration coefficients varied by about 4% over a period of one year.

A comparison of calibrated attenuated backscatter data from the two different types of ceilometers located at the same site confirms the reliability of this calibration method. The two independently calibrated ceilometers, each with their own challenges (e.g. water vapour, receiver saturation), are shown to be consistent with each other, with a correlation vaue of 0.95. This result is important for an operational network such as the Met Office ceilometer network because it helps maintain a reliable, comparable stream of calibrated data, with water vapour and receiver saturation successfully accounted for, from each instrument at each site.

6.3 Ice cloud attenuated backscatter forward model

Chapter 5 introduced a novel forward model that uses IWC to calculate a vertical profile of attenuated backscatter. By assuming a second moment approximation for particle area and

mass, IWC becomes proportional to extinction. The lidar ratio for ice cloud is then used to calculate backscatter from extinction and attenuation is applied. The lidar ratio for ice cloud was calculated using ceilometer observations of thick, attenuating ice cloud, and was found to be 42.8 ± 10.9 sr. This forward model was also used to calculate vertical profiles of attenuated backscatter from IWC derived from the Chilbolton Copernicus radar to test the assumptions made by the ice cloud forward model.

Nine case studies were analysed and comparisons between the UKV derived attenuated backscatter and the attenuated backscatter observed by the Vaisala CL51 ceilometer suggest that the UKV IWC is systematically too small in magnitude and too high in height.

6.4 Recommendations for immediate adoption

6.4.1 Met Office Ceilometer Network

The work in this thesis has built on the original cloud calibration method, refining it to correct for instrument related issues as summarised in section 6.1. In order to move forward with operational application of the calibration algorithm, there are a couple of recommendations that would be beneficial to ensure accurate calibration and observation data. The water vapour correction could be improved by using the UKV water vapour data for the nearest grid-box instead of using the Chilbolton grid-box data for all ceilometers.

In addition, the ceilometers should be deployed so that they are a few degrees off zenith to avoid specular reflection. The Chilbolton ceilometer is tilted by 4 degrees off the zenith to avoid specular reflection from ice crystals. Any ceilometer used to study ice clouds must be tilted at this same angle to avoid measuring spuriously high backscatter. It is not clear that the Met Office ceilometers have been installed in this way; as they are an operational network, checking and correcting this has currently not been possible.

6.5 Recommendations for future work

6.5.1 Calibration

Although the calibration algorithm is ready for immediate adoption, there are some outstanding issues which could improve it further. Section 3.4.5, in Chapter 3, hypothesised that the reduction in the magnitude of attenuated backscatter for clouds with a base below 500 m could be caused by either an instrument related issue (e.g. saturation) or due to microphysical properties of low-level clouds. Further work is necessary to give a definitive answer to this issue.

Another area which could be improved by further research is applying a correction for attenuation due to aerosol below the liquid water cloud. This would improve the ability to apply the calibration to ceilometers located in areas with high pollution (e.g. Warren et al.,2018). However, in order to apply a correction for attenuation due to aerosol, measurements of the aerosol lidar ratio would be required. The lidar ratio of aerosol is highly variable compared to the stability of the lidar ratio for liquid water cloud and inaccuracies in an aerosol attenuation correction would degrade the calibration.

6.5.2 Ice Cloud Forward Model

The development of the ice cloud forward model has shown the potential for using ceilometer data to improve the forecasting of IWC in the UKV. Forward models have been developed within the Met Office to model the attenuated backscatter from liquid water and from aerosol and the combining of these forward models would better simulate the ceilometer observations. Further development of the ice cloud forward model would also benefit from testing on a larger data set and extending the observation data to include the ceilometer network. With this

additional data, we would then be able to better quantify the differences between the observations and the forward model.

The development of the ice model would benefit from incorporating a temperature dependent relationship instead of a fixed value. This could be done using the relationship between IWC and extinction, as encapsulated in equation 5.9, which relates these two variables to the effective radius (R_{eff}). The ice model could therefore be adapted to use $R_{eff} = R_{eff}(T, IWC)$ and not the fixed value 49 μm that is currently assumed. This would then reduce the potential bias discussed in Section 5.13. Using this approach, the model could also be adapted to include a calculated value of η instead of the current assumed fixed value approach.

There would be several other issues to consider and challenges to overcome. The work in this thesis has highlighted the need for high vertical resolution in the forward modelling of ceilometer attenuated backscatter from ice clouds, much higher than the vertical resolution of NWP models. It seems likely that this issue would also be relevant to the forward modelling of liquid water clouds, but as far as we are aware, this has yet to be explored in the literature. The attenuation by liquid clouds is very rapid, which may make this effect bigger than it is for ice cloud.

Currently, the forward model only represents ice and snow water content. This could be extended to include liquid water content as well, which would provide information on supercooled and mixed-phase regions within cold clouds, which Hogan et al. (2003) have shown to be a frequent occurrence but which have been excluded from the work in this thesis.

Comparisons with Vaisala CL31 ceilometers may also prove difficult. The Met Office Vaisala CL31 ceilometers would need their firmware updated to remove the processing that results in cosmetic shifts above 2.4 km. Furthermore, the Vaisala CL31 ceilometers have a much lower signal-to-noise ratio at the heights where ice clouds are typically found.

The Met Office has, in addition to the fairly dense network of ceilometers, a national radar network. A potential avenue for future work could explore these products being combined to produce 3D maps of the current clouds and precipitation over the UK. EUMETNET is currently networking 700 European ceilometers so they can provide ceilometer profiles in near real time to European weather forecast centres. Currently quality controlled profiles from 220 ceilometers are being delivered to a central data hub where they can be accessed in near real time by European weather forecasting centres. The field of research using a network of ceilometers has many promising avenues but is still very much in its infancy.

References

Abel, S. J., Cotton, R. J., Barrett, P. A., & Vance, A. K. (2014). A comparison of ice water content measurement techniques on the FAAM BAe-146 aircraft. *Atmospheric Measurement Techniques*, *7*(9), 3007-3022.

Albrecht, B. A., Randall, D. A., & Nicholls, S. (1988). Observations of marine stratocumulus clouds during FIRE. *Bulletin of the American Meteorological Society*, *69*(6), 618-626.

Ansmann, A., Wandinger, U., Riebesell, M., Weitkamp, C., & Michaelis, W. (1992). Independent measurement of extinction and backscatter profiles in cirrus clouds by using a combined Raman elastic-backscatter lidar. *Applied optics*, *31*(33), 7113-7131.

Bouttier, F. and Courtier, P. (1999), Data assimilation concepts and methods, https://www.ecmwf.int/sites/default/files/elibrary/2002/16928-data-assimilation-concepts-and-methods.pdf, last access 10 September 2018.

Brown, P.R. (1993). Measurements of the ice water content in cirrus using an evaporative technique. *Journal of Atmospheric and Oceanic Technology*, *10*(4), pp.579-590.

Charlton-Perez, C., Cox, O., Ballard, S., and Klugmann, D. (2013). A forward model for attenuated backscatter due to aerosols, clouds and rain, Met Office Report.

Chiriaco, M., Vautard, R., Chepfer, H., Haeffelin, M., Dudhia, J., Wanherdrick, Y., Morille, Y. and Protat, A. (2006). The ability of MM5 to simulate ice clouds: Systematic comparison between simulated and measured fluxes and lidar/radar profiles at the SIRTA atmospheric observatory. *Monthly weather review*, *134*(3), pp.897-918.

Cossu, F., Hocke, K., Martynov, A., Martius, O., & Mätzler, C. (2015). Atmospheric water parameters measured by a ground-based microwave radiometer and compared with the WRF model. *Atmospheric science letters*, *16*(4), 465-472.

Costa-Surós, M., Calbó, J., González, J. A., & Martin-Vide, J. (2013). Behavior of cloud base height from ceilometer measurements. *Atmospheric research*, *127*, 64-76.

Delanoë, J., Hogan, R.J., Forbes, R.M., Bodas-Salcedo, A. and Stein, T.H. (2011). Evaluation of ice cloud representation in the ECMWF and UK Met Office models using CloudSat and CALIPSO data. *Quarterly Journal of the Royal Meteorological Society*, *137*(661), pp.2064-2078.

Dupont, J. C., Haeffelin, M., Protat, A., Bouniol, D., Boyouk, N., & Morille, Y. (2012). Stratus–fog formation and dissipation: a 6-day case study. *Boundary-layer meteorology*, *143*(1), 207-225.

Eberhard, W. L. (1986). Cloud signals from lidar and rotating beam ceilometer compared with pilot ceiling. *Journal of Atmospheric and Oceanic Technology*, *3*(3), 499-512.

Edwards, J.M. and Slingo, A. (1996). Studies with a flexible new radiation code. I: Choosing a configuration for a large-scale model. *Quarterly Journal of the Royal Meteorological Society*, *122*(531), pp.689-719.

Eloranta, E. W. (1998). Practical model for the calculation of multiply scattered lidar returns. *Applied Optics*, *37*(12), 2464-2472.

Eloranta, E. W., Kuehn, R. E., & Holz, R. E. (2001). Measurements of backscatter phase function and depolarization in cirrus clouds made with the University of Wisconsin High Spectral Resolution Lidar. *Advances in Laser Remote Sensing*, 255-257.

Emeis, S., Schäfer, K., & Münkel, C. (2009). Observation of the structure of the urban boundary layer with different ceilometers and validation by RASS data. *Meteorologische Zeitschrift*, *18*(2), 149-154.

Eresmaa, N., Härkönen, J., Joffre, S. M., Schultz, D. M., Karppinen, A., & Kukkonen, J. (2012). A three-step method for estimating the mixing height using ceilometer data from the Helsinki Testbed. *Journal of Applied Meteorology and Climatology*, *51*(12), 2172-2187.

Fiocco, G., & Smullin, L. D. (1963). Detection of scattering layers in the upper atmosphere (60–140 km) by optical radar. *Nature*, *199*(4900), 1275.

Fu, Q. (2007). A new parameterization of an asymmetry factor of cirrus clouds for climate models. *Journal of the Atmospheric Sciences*, *64*(11), 4140-4150.

Garrett, T. J., Hobbs, P. V., & Gerber, H. (2001). Shortwave, single-scattering properties of arctic ice clouds. *Journal of Geophysical Research: Atmospheres*, *106*(D14), 15155-15172.

Haeffelin, M., Laffineur, Q., Bravo-Aranda, J. A., Drouin, M. A., Casquero-Vera, J. A., Dupont, J. C., & Backer, H. D. (2016). Radiation fog formation alerts using attenuated backscatter power from automatic lidars and ceilometers. *Atmospheric Measurement Techniques*, *9*(11), 5347-5365.

Hervo, M., Poltera, Y., & Haefele, A. (2016). An empirical method to correct for temperature-dependent variations in the overlap function of CHM15k ceilometers. *Atmospheric Measurement Techniques*, *9*(7), 2947-2959.

Heymsfield, A. J., Winker, D., & van Zadelhoff, G. J. (2005). Extinction-ice water content-effective radius algorithms for CALIPSO. *Geophysical research letters*, *32*(10).

Heymsfield, A. J., Schmitt, C., & Bansemer, A. (2013). Ice cloud particle size distributions and pressure-dependent terminal velocities from in situ observations at temperatures from 0 to− 86 C. *Journal of the Atmospheric Sciences*, *70*(12), 4123-4154.

Hirsch, E., Agassi, E., & Koren, I. (2011). A novel technique for extracting clouds base height using ground based imaging. *Atmospheric Measurement Techniques*, *4*(1), 117.

Hogan, R.J., Illingworth, A.J. and Sauvageot, H., (2000). Measuring crystal size in cirrus using 35-and 94-GHz radars. *Journal of Atmospheric and Oceanic Technology*, *17*(1), pp.27-37.

Hogan, R. J., Illingworth, A. J., O'connor, E. J., & Baptista, J. P. V. (2003). Characteristics of mixed-phase clouds. II: A climatology from ground-based lidar. *Quarterly Journal of the Royal Meteorological Society*, *129*(592), 2117-2134.

Hogan, R. J. (2006). Fast approximate calculation of multiply scattered lidar returns. *Applied Optics*, *45*(23), 5984-5992.

Hogan, R. J., Mittermaier, M. P., & Illingworth, A. J. (2006). The retrieval of ice water content from radar reflectivity factor and temperature and its use in evaluating a mesoscale model. *Journal of applied meteorology and climatology*, *45*(2), 301-317.

Hogan, R. J. (2008). Fast lidar and radar multiple-scattering models. Part I: Small-angle scattering using the photon variance–covariance method. *Journal of the Atmospheric Sciences*, *65*(12), 3621-3635.

Huang, L. X., Isaac, G. A., & Sheng, G. (2012). Integrating NWP forecasts and observation data to improve nowcasting accuracy. *Weather and Forecasting*, *27*(4), 938-953.

Illingworth, A.J., Cimini, D., Gaffard, C., Haeffelin, M., Lehmann, V., Löhnert, U., O'Connor, E.J. and Ruffieux, D. (2015). Exploiting existing ground-based remote sensing networks to improve high-resolution weather forecasts. *Bulletin of the American Meteorological Society*, *96*(12), pp.2107-2125.

Jensen, E.J., Lawson, P., Baker, B., Pilson, B., Mo, Q., Heymsfield, A.J., Bansemer, A., Bui, T.P., McGill, M., Hlavka, D. and Heymsfield, G., 2009. On the importance of small ice crystals in tropical anvil cirrus. *Atmospheric Chemistry and Physics*, *9*(15), pp.5519-5537.

Jacob, N. (1949). *U.S. Patent No. 2,481,034*. Washington, DC: U.S. Patent and Trademark Office.

Kent, G. S., & Keenliside, W. (1975). Laser radar observations of the θ3ω, 1 diurnal atmospheric tidal mode above Kingston, Jamaica. *Journal of the Atmospheric Sciences*, *32*(9), 1663-1666.

Kotthaus, S., O'Connor, E., Münkel, C., Charlton-Perez, C., Haeffelin, M., Gabey, A. M., & Grimmond, C. S. B. (2016). Recommendations for processing atmospheric attenuated backscatter profiles from Vaisala CL31 ceilometers. *Atmospheric Measurement Techniques*, *9*(8), 3769-3791.

Korolev, A.V., Emery, E.F., Strapp, J.W., Cober, S.G., Isaac, G.A., Wasey, M. and Marcotte, D., 2011. Small ice particles in tropospheric clouds: Fact or artifact? Airborne Icing Instrumentation Evaluation Experiment. *Bulletin of the American Meteorological Society*, *92*(8), pp.967-973.

Lorenc, A.C. (1986). Analysis methods for numerical weather prediction. *Quarterly Journal of the Royal Meteorological Society*, *112*(474), pp.1177-1194.

Lohmann, U., Lüönd, F., & Mahrt, F. (2016). *An introduction to clouds: From the microscale to climate*. Cambridge University Press.

Lorenz, E.N. (1963). Deterministic nonperiodic flow. *Journal of the atmospheric sciences*, *20*(2), pp.130-141.

La Cour, P. (1871): Maaling af sammenhængende Skylags Høide (English translation: Measurements of the height of coherent cloud layers*). Tidsskrift for Physik og Chemi,* 10, 321-334.

Madonna, F., Amato, F., Vande Hey, J., & Pappalardo, G. (2015). Ceilometer aerosol profiling vs. Raman lidar in the frame of INTERACT campaign of ACTRIS. *Atmospheric Measurement Techniques*, *7*(12).

Markowicz, K. M., Flatau, P. J., Kardas, A. E., Remiszewska, J., Stelmaszczyk, K., & Woeste, L. (2008). Ceilometer retrieval of the boundary layer vertical aerosol extinction structure. *Journal of Atmospheric and Oceanic Technology*, *25*(6), 928-944.

Markowicz, K.M., Zielinski, T., Pietruczuk, A., Posyniak, M., Zawadzka, O., Makuch, P., Stachlewska, I.S., Jagodnicka, A.K., Petelski, T., Kumala, W. and Sobolewski, P. (2012). Remote sensing measurements of the volcanic ash plume over Poland in April 2010. *Atmospheric environment*, *48*, pp.66-75.

Martucci, G., Milroy, C., & O'Dowd, C. D. (2010). Detection of cloud-base height using Jenoptik CHM15K and Vaisala CL31 ceilometers. *Journal of Atmospheric and Oceanic Technology*, *27*(2), 305-318.

Mattis, I., Begbie, R., Boyouk, N., Bravo-Aranda, J.A., Brettle, M., Cermak, J., Drouin, M.A., Geiß, A., Görsdorf, U., Haefele, A. and Haeffelin, M. (2016). The ceilometer inter-comparison campaign CeiLinEx2015. In *EGU General Assembly Conference Abstracts* (Vol. 18, p. 9687).

Mattis, I. and Wagner, F. (2014), E-PROFILE: Glossary of lidar and ceilometer variables.

McCormick, P. D., Silverberg, E. C., Poultney, S. K., Van Wijk, U., Alley, C. O., & Bettinger, R. T. (1967). Optical radar detection of backscattering from the upper atmosphere. *Nature*, *215*(5107), 1262.

Mie, G. (1908). Beiträge zur Optik trüber Medien, speziell kolloidaler Metallösungen. *Annalen der physik*, *330*(3), 377-445.

Müller, D., Ansmann, A., Mattis, I., Tesche, M., Wandinger, U., Althausen, D., & Pisani, G. (2007). Aerosol-type-dependent lidar ratios observed with Raman lidar. *Journal of Geophysical Research: Atmospheres*, *112*(D16).

Münkel, C., Eresmaa, N., Räsänen, J., & Karppinen, A. (2007). Retrieval of mixing height and dust concentration with lidar ceilometer. *Boundary-layer meteorology*, *124*(1), 117-128.

Münkel, C., Roininen, R., & Oyj, V. (2010). *Investigation of boundary layer structures with ceilometer using a novel robust algorithm*. American Meteorological Society.

Nielsen, K. P., translated in EMS (2007). The invention of the ceilometer, European Meteorological Society, https://www.emetsoc.org/the-invention-of-the-ceilometer/, last access 10 September 2018.

Nicholls, S. Q. J. R. (1984). The dynamics of stratocumulus: Aircraft observations and comparisons with a mixed layer model. *Quarterly Journal of the Royal Meteorological Society*, *110*(466), 783-820.

O'Connor, E. J., Illingworth, A. J., & Hogan, R. J. (2004). A technique for autocalibration of cloud lidar. *Journal of Atmospheric and Oceanic Technology*, *21*(5), 777-786.

Omar, A.H., Winker, D.M., Vaughan, M.A., Hu, Y., Trepte, C.R., Ferrare, R.A., Lee, K.P., Hostetler, C.A., Kittaka, C., Rogers, R.R. and Kuehn, R.E. (2009). The CALIPSO automated aerosol classification and lidar ratio selection algorithm. *Journal of Atmospheric and Oceanic Technology*, *26*(10), pp.1994-2014.

OSCAR (Observing Systems Capability Analysis and Review Tool): https://www.wmo-sat.info/oscar, last access: 27 June 2018.

Oyj, V. (2006). Vaisala Ceilometer CL31 user's guide. *Vaisala Oyj, Helsinki, Finland*.

Pawlowska, H., Brenguier, J. L., & Burnet, F. (2000). Microphysical properties of stratocumulus clouds. *Atmospheric research*, *55*(1), 15-33.

Pinnick, R. G., Jennings, S. G., Chýlek, P., Ham, C., & Grandy Jr, W. T. (1983). Backscatter and extinction in water clouds. *Journal of Geophysical Research: Oceans*, *88*(C11), 6787-6796.

Plass, G. N., & Kattawar, G. W. (1971). Reflection of light pulses from clouds. *Applied optics*, *10*(10), 2304-2310.

Platt, C. M. R. (1973). Lidar and radiometric observations of cirrus clouds. *Journal of the atmospheric sciences*, *30*(6), 1191-1204.

Platt, C. M., Young, S. A., Carswell, A. I., Pal, S. R., McCormick, M. P., Winker, D. M., ... & Flamant, P. H. (1994). The experimental cloud lidar pilot study (ECLIPS) for cloud–radiation research. *Bulletin of the American Meteorological Society*, *75*(9), 1635-1654.

Protat, A., Bouniol, D., O'Connor, E. J., Klein Baltink, H., Verlinde, J., & Widener, K. (2011). CloudSat as a global radar calibrator. *Journal of atmospheric and oceanic technology*, *28*(3), 445-452.

Reichardt, J., Reichardt, S., Behrendt, A., & McGee, T. J. (2002). Correlations among the optical properties of cirrus-cloud particles: Implications for spaceborne remote sensing. *Geophysical research letters*, *29*(14).

Rogers, R. R., Lamoureux, M. F., Bissonnette, L. R., & Peters, R. M. (1997). Quantitative interpretation of laser ceilometer intensity profiles. *Journal of atmospheric and oceanic technology*, *14*(3), 396-411.

Segre, J. P., & Truscott, N. R. (1976). *U.S. Patent No. 3,963,347*. Washington, DC: U.S. Patent and Trademark Office.

Schuhen, N., Thorarinsdottir, T. L., & Lenkoski, A. (2018, April). Improving forecasts through rapid updating of temperature trajectories and statistical post-processing. In *EGU General Assembly Conference Abstracts* (Vol. 20, p. 8646).

Stein, T. H., Delanoë, J., & Hogan, R. J. (2011). A comparison among four different retrieval methods for ice-cloud properties using data from CloudSat, CALIPSO, and MODIS. *Journal of Applied Meteorology and Climatology*, *50*(9), 1952-1969.

Stocker, T.F., Qin, D., Plattner, G., Tignor, M., Allen, S.K., Boschung, J., Nauels, A., Xia, Y., Bex, V. and Midgley, P., 2013. IPCC, (2013). Summary for policymakers in climate change 2013: The physical science basis, contribution of working group I to the fifth assessment report of the intergovernmental panel on climate change.

Sokół, P., Stachlewska, I., Ungureanu, I., & Stefan, S. (2014). Evaluation of the boundary layer morning transition using the CL-31 ceilometer signals. *Acta Geophysica*, *62*(2), 367-380.

Tang, Y., Lean, H. W., & Bornemann, J. (2013). The benefits of the Met Office variable resolution NWP model for forecasting convection. *Meteorological Applications*, *20*(4), 417-426.

Tang, G., Zhang, J., Zhu, X., Song, T., Münkel, C., Hu, B., Schäfer, K., Liu, Z., Zhang, J., Wang, L. and Xin, J. (2016). Mixing layer height and its implications for air pollution over Beijing, China. *Atmospheric Chemistry and Physics*, *16*(4), pp.2459-2475.

Tsaknakis, G., Papayannis, A., Kokkalis, P., Amiridis, V., Kambezidis, H.D., Mamouri, R.E., Georgoussis, G. and Avdikos, G. (2011). Inter-comparison of lidar and ceilometer retrievals for aerosol and Planetary Boundary Layer profiling over Athens, Greece. *Atmospheric Measurement Techniques*, *4*(6), pp.1261-1273.

Van Tricht, K., Gorodetskaya, I. V., Lhermitte, S., Turner, D. D., Schween, J. H., & Van Lipzig, N. P. M. (2014). An improved algorithm for polar cloud-base detection by ceilometer over the ice sheets. *Atmospheric Measurement Techniques*, *7*(5), 1153-1167.

Van Zadelhoff, G.J., Donovan, D.P., Klein Baltink, H. and Boers, R. (2004). Comparing ice cloud microphysical properties using CloudNET and Atmospheric Radiation Measurement Program data. *Journal of Geophysical Research: Atmospheres*, *109*(D24).

Vande Hey, J. V., Coupland, J., Foo, M. H., Richards, J., & Sandford, A. (2011). Determination of overlap in lidar systems. *Applied optics*, *50*(30), 5791-5797.

Vande Hey, J. D. (2013). *Design, implementation, and characterisation of a novel lidar ceilometer* (Doctoral dissertation, © Joshua D. Vande Hey).

Waliser, D.E., Li, J.L.F., Woods, C.P., Austin, R.T., Bacmeister, J., Chern, J., Del Genio, A., Jiang, J.H., Kuang, Z., Meng, H. and Minnis, P. (2009). Cloud ice: A climate model

challenge with signs and expectations of progress. *Journal of Geophysical Research: Atmospheres*, *114*(D8).

Wallace, J.M. and Hobbs, P.V., 2006. *Atmospheric science: an introductory survey* (Vol. 92). Elsevier.

Wang, C., Platnick, S., Zhang, Z., Meyer, K. and Yang, P. (2016). Retrieval of ice cloud properties using an optimal estimation algorithm and MODIS infrared observations: 1. Forward model, error analysis, and information content. *Journal of Geophysical Research: Atmospheres*, *121*(10), pp.5809-5826.

Warren, E., Charlton-Perez, C., Kotthaus, S., Lean, H., Ballard, S., Hopkin, E. and Grimmond, S., (2018). Evaluation of forward-modelled attenuated backscatter using an urban ceilometer network in London under clear-sky conditions. *Atmospheric Environment*, *191*, pp.532-547.

Weitkamp, C. (Ed.). (2006). *Lidar: range-resolved optical remote sensing of the atmosphere* (Vol. 102). Springer Science & Business.

Westbrook, C. D., Illingworth, A. J., O'Connor, E. J., & Hogan, R. J. (2010a). Doppler lidar measurements of oriented planar ice crystals falling from supercooled and glaciated layer clouds. *Quarterly Journal of the Royal Meteorological Society*, *136*(646), 260-276.

Westbrook, C. D., Hogan, R. J., O'Connor, E. J., & Illingworth, A. J. (2010b). Estimating drizzle drop size and precipitation rate using two-colour lidar measurements. *Atmospheric Measurement Techniques*, *3*(3), 671-681.

Westbrook, C.D. and Illingworth, A.J. (2009). Testing the influence of small crystals on ice size spectra using Doppler lidar observations. *Geophysical Research Letters*, *36*(12).

Wiegner, M., Madonna, F., Binietoglou, I., Forkel, R., Gasteiger, J., Geiß, A., Thomas, W. (2014). What is the benefit of ceilometers for aerosol remote sensing? An answer from EARLINET. *Atmospheric Measurement Techniques*, *7*(7), 1979-1997.

Wiegner, M., & Gasteiger, J. (2015). Correction of water vapor absorption for aerosol remote sensing with ceilometers. *Atmospheric Measurement Techniques*, (9), 3971-3984.

Wilkinson, J., D. Wilson, and R. Forbes, (2009), The large-scale precipitation parametrization scheme, Unified Model Documentation Paper 26 , Met Office, Exeter, UK, Unified Model Version 7.3.

Wilkinson, J.M., Hogan, R.J., Illingworth, A.J. and Benedetti, A. (2008). Use of a lidar forward model for global comparisons of cloud fraction between the ICESat lidar and the ECMWF model. *Monthly weather review*, *136*(10), pp.3742-3759.

Wu, Y., Gan, C. M., Cordero, L., Gross, B., Moshary, F., & Ahmed, S. (2011). Calibration of the 1064 nm lidar channel using water phase and cirrus clouds. *Applied optics*, *50*(21), 3987-3999.

Yorks, J. E., Hlavka, D. L., Hart, W. D., & McGill, M. J. (2011). Statistics of cloud optical properties from airborne lidar measurements. *Journal of Atmospheric and Oceanic Technology*, *28*(7), 869-883.

Appendix A

This section details how the lidar ratio is related to the lidar equation as shown by O'Connor et al. (2004). As in equation 2.3, the lidar equation can be written in the form,

$$\beta_{obs}(r,\lambda) = \beta_{TRUE}(r,\lambda)\exp\left[-2\eta\int_0^r \alpha(r,\lambda)dr\right] \qquad \textit{Eq. (A.1)}$$

where $\beta_{obs}(r,\lambda)$ is the observed attenuated backscatter, $\beta_{TRUE}(r,\lambda)$is the backscatter coefficient and $\alpha(r,\lambda)$is the atmospheric extinction coefficient and η is the multiple scattering factor. If we consider a cloud with base at $r = 0$, and, at a distance r into the cloud, the extinction coefficient is $\alpha(r)$, the backscatter is $\beta_{\mathrm{TRUE}}(r)$, and the optical depth is $\tau(r)$. The observed backscatter, $\beta_{\mathrm{OBS}}(r)$, from this height is given by

$$\beta_{obs}(r,\lambda) = \beta_{TRUE}(r,\lambda)\exp[-2\tau(r,\lambda)] \qquad \textit{Eq. (A.2)}$$

Where $\exp[-2\tau(r,\lambda)] = \exp\left[-2\eta\int_0^r \alpha(r,\lambda)dr\right]$ and τ is the optical thickness. For a small distance, dr, the change in optical thickness $d\tau = \alpha(r)\,dr$, and if, for the moment, we neglect multiple scattering, then we have

$$d\tau = S(r)\beta_{TRUE}(r,\lambda)dr \qquad \textit{Eq. (A.3)}$$

where S is the lidar ratio defined as equal to $\alpha(r,\lambda)/\beta_{\mathrm{TRUE}}(r,\lambda)$. The increase in backscatter and apparent reduction in attenuation due to multiple scattering can be expressed by defining a multiple-scattering factor, η, which can take values between 0.5 and 1, so that the effective change in optical thickness is

$$d\tau = \eta(r,\lambda)S(r,\lambda)\beta_{TRUE}(r,\lambda)dr \qquad \textit{Eq. (A.4)}$$

and the apparent lidar ratio, $\sigma(r,\lambda)/\beta_{\mathrm{TRUE}}(r,\lambda)$, is ηS. If we now consider the total integrated backscatter, B, that is the value of observed backscatter β_{OBS} integrated along the path until the signal is totally attenuated at $z = \infty$, we have

$$B = \int_0^{\infty} \beta_{obs}(r,\lambda)\, dr = \int_0^{\infty} \beta_{TRUE}(r,\lambda) \exp[-2\tau(r,\lambda)] dr \qquad \textit{Eq. (A.5)}$$

$$= \frac{1}{\eta S} \int \exp(-2\tau) d\tau \qquad \textit{Eq. (A.6)}$$

$$= \frac{1}{2\eta S} \qquad \textit{Eq. (A.7)}$$

From the observed backscatter, an apparent S (S_{app}) can be calculated. As S in stratocumulus is a known value of 18.8 sr, the calibration coefficient, C, is therefore

$$C = \frac{S_{app}}{S} \qquad \textit{Eq. (A.8)}$$

Appendix B

This appendix details the basic setup of a lidar system which is essentially a transmitter and a receiver, as shown in Figure B.1. The transmitter consists of a laser which generates short light pulses of a few to several hundred nanoseconds. A beam expander is usually applied to reduce the divergence of the light beam before it is transmitted (Weitkamp, 2006).

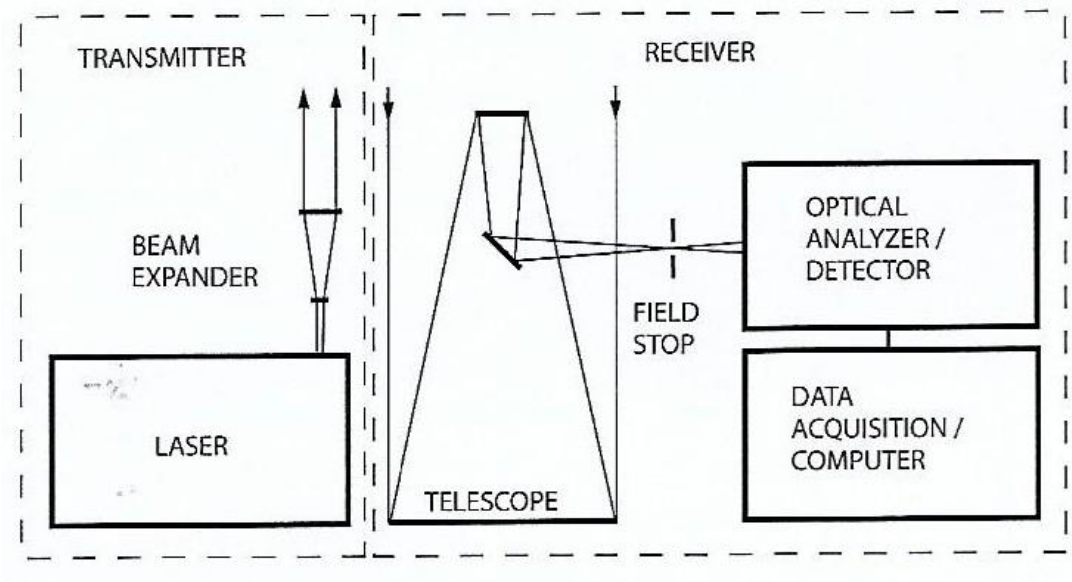

Figure B.0-1: Principal setup of a lidar system (Source: Weitkamp, 2006)

The receiver is a telescope which collects the photons which have been backscattered from the atmosphere. The detector converts the received optical signal into an electrical signal, the intensity of which is determined and stored to the computer.